

AN EXPERIMENTAL STUDY OF DRAG REDUCTION DUE TO THE ROLLER
BEARING EFFECT OVER GROOVED SURFACES INSPIRED BY
BUTTERFLY SCALES

by

SASHANK GAUTAM

AMY W. LANG, COMMITTEE CHAIR

DAVID W. MACPHEE

JAMES P. HUBNER

MUHAMMAD A. R. SHARIF

SEMIH OLCMEN

A DISSERTATION

Submitted in partial fulfillment of the requirements for the degree of Doctor of
Philosophy in the Department of Aerospace Engineering and
Mechanics in the Graduate School of
The University of Alabama

TUSCALOOSA, ALABAMA

2021

Copyright Sashank Gautam 2021
ALL RIGHTS RESERVED

ABSTRACT

Monarch butterfly wings are covered in minuscule scales (approximately 100 μm in length) which align together in a pattern that resembles roof shingles. Flight tests performed on live butterflies showed that these scales provide a beneficial aerodynamic function. The scales are angled upwards such that transverse cavities form for a flow passing perpendicular to the rows of scales. Flow visualization of butterfly inspired cavities has shown that the entrapped vortex (or vortices) inside each cavity can act as a fluidic bearing to the outer boundary layer flow resulting in reduced surface or skin friction drag. This study conducted experiments on cavity embedded flat plates, mimicking the butterfly scale geometry, documenting this “roller-bearing effect”. The experiments were performed in a tow-tank facility, and DPIV measurements were used to calculate the surface drag based on the measured boundary layer velocity profiles. Experimental models with cavity geometries of AR 2 and 3 and wall inclination angles of 22°, 45° and 90° were tested, where the slanted models were inspired from observed butterfly scale geometries. Each of these models exhibited net surface drag reduction for lower Re_d range of 4.5 to 8.5, except for the 22° cavity with AR 2 which showed an increase in drag for all the Re_d cases. The Re_d is defined based on the cavity depth which is kept constant for all the models. As the cavity geometry was varied, the shape of the vortex and the dividing streamline also changed, which in turn affected the surface drag. The model with a 45° cavity wall inclination and AR 2 had the highest surface drag reduction ranging from 18.63% to 26.33% at lower Re_d range. Additionally, the critical Re_d region, beyond which the embedded vortex becomes unstable, and fluid begins to enter and eject out of the cavity,

mixing with the outer boundary layer flow and thereby eliminating the drag reduction effect, is documented for various cavity geometries, and ranged from Re_d 90 to 120. As was hypothesized, the increase in Re_d beyond the critical region resulted in an increase in surface drag.

DEDICATION

To my parents.

LIST OF ABBREVIATIONS AND SYMBOLS

AR	Aspect ratio (Length of cavity / cavity depth)
BL	Boundary layer
C_d	Local drag coefficient
C_D	Drag coefficient
$D_{\Delta mom}$	Drag due to difference in rate of change of momentum in control surface
$\Delta D\%$	Percentage difference in surface drag
DPIV	Digital particle image velocimetry
FPS	Frame per second
F_D	Surface drag force
LE	Leading Edge
PRF	Pulse repetition frequency
q	Dynamic pressure
U_o	Stream velocity
u	Local streamwise velocity
u_{rms}	Root mean square value of the local streamwise velocity
v	Local normal velocity
v_{rms}	Root mean square value of the local normal velocity
Re_d	Reynolds number (based on depth of the cavity)
δ	Boundary layer thickness

δ^*	Displacement thickness
θ	Momentum thickness
ρ	Density of fluid
τ_w	Wall Shear stress
μ	Dynamic viscosity
ν	Kinematic viscosity

ACKNOWLEDGEMENTS

I would like to thank my advisor and committee chair Dr. Amy W. Lang for her immense support, guidance, and mentorship during my PhD program. I thank her for providing me an opportunity to work in this research and for always believing in me. Her broad knowledge of fluid dynamics and experience on bio-inspired research is an invaluable addition for this dissertation. I would also like to thank my committee members Dr. James Paul Hubner, Dr. David W. Macphee, Dr. Semih Olcmen, and Dr. Muhammad Ali Rob Sharif for providing insightful suggestions and reviewing my dissertation.

I would like to thank all my current and former lab mates, particularly Leonardo Santos, Andrew Bonacci, Adam Cross, Trevor Berg, Christopher Jarmon, Julia Barefoot, Jacob A. Wilroy, Chase Parsons, Cassidy Elliot and Sean Devey for their assistance they have provided me in the lab. I am also grateful to the staffs of Machine shop David Kimbrell, Bobby (Jim) Edmonds, Sam Tingle, James Yarbrough, and Alan Texada for their help on designing and machining the equipment setup and the models.

Additionally, I am grateful for the funding support from NSF CBET fluid dynamics grant number 1335848, writing and University of Alabama graduate council fellowship from the graduate school, and the teaching assistantships from department of Aerospace Engineering and Mechanics, UA. Finally, I would like to thank my family and friends for their well wishes and generous support.

CONTENTS

ABSTRACT.....	ii
DEDICATION.....	iv
LIST OF ABBREVIATIONS AND SYMBOLS	v
ACKNOWLEDGEMENTS.....	vii
LIST OF TABLES.....	x
LIST OF FIGURES	xi
CHAPTER 1 INTRODUCTION.....	1
1.1 OVERVIEW	1
1.2 MOTIVATION.....	3
1.3 OBJECTIVES.....	6
1.4 DISSERTATION ORGANIZATION	8
CHAPTER 2 LITERATURE REVIEW	9
2.1 VORTEX FORMATION IN A CAVITY	9
2.2 EFFECT OF CAVITY EMBEDDED VORTEX ON BOUNDARY LAYER FLOW ..	14
2.3 SURFACE DRAG REDUCTION DUE TO THE CAVITY VORTEX	17
2.4 SUMMARY.....	24
CHAPTER 3 EXPERIMENTAL SETUP, MODELS AND VALIDATION	25
3.1 EXPERIMENT SETUP	25
3.1.1 TOW TANK STRUCTURES AND EQUIPMENT	25
3.1.2 DPIV	28
3.1.3 DATA.....	29

3.3 MODELS	33
3.4 VALIDATION OF EXPERIMENTAL SETUP.....	37
3.4.1 COMPARISON OF VELOCITY PROFILES.....	37
CHAPTER 4 RESULTS AND DISCUSSION.....	44
4.1 FLOW VISUALISATION OF CAVITY VORTEX	44
4.2 SURFACE DRAG	51
4.3 UNCERTAINTY CALCULATION.....	63
CHAPTER 5 CONCLUSION.....	68
5.1 LIMITATIONS.....	70
5.2 FUTURE WORK.....	71
REFERENCES	72
APPENDIX A: TRAVERSE SPECIFICATION.....	77
APPENDIX B: DATA PROCESSING AND POST PROCESSING.....	78
APPENDIX C: LEADING EDGE DESIGN	81
APPENDIX D: ANSYS FLUENT SIMULATION OF FLOW OVER FLAT PLATE.....	83
APPENDIX E CALCULATION OF PRESSURE FORCE	86
APPENDIX F MATLAB CODE.....	88
F.1 SUPERPOSITION OF IMAGES	88
F.2 IMAGE STABILIZATION	89
F.3 RATE OF CHANGE OF MOMENTUM CALCULATION	91
APPENDIX G LABVIEW VI	97
G.1 VI FOR DATA ACQUISITION.....	97

LIST OF TABLES

Table 3.1: Operating parameters of the laser and the camera	30
Table 3.2: Processing window size	32
Table 3.3: Geometry and dimensions of cavity of the grooved plate models	35
Table 3.4: Characteristic upstream boundary layer properties of a flat plate flow	43
Table 3.5: Characteristic downstream boundary layer properties of a flat plate flow	43
Table 4.2: Comparison of drag reduction from different studies	55
Table 4.3: Percentage of drag reduction of various models at various Re_d	59
Table 4.4: Mean slip velocity magnitude for various models	60
Table 4.5: Dividing streamline height at the center of cavity for Re_d 8.5	62
Table 4.6: List of error values and uncertainty	65
Table E1: Calculation of Pressure force on the control surface	86

LIST OF FIGURES

Figure 1.1.1 A continuous leading edge vortex formed over a butterfly [13]	2
Figure 1.1.2 Scales of Monarch butterfly	2
Figure 1.2.1: Comparison of efficiency for cases with and without scales of Monarch butterfly	4
Figure 1.2.2: Solid arrow shows the flow in traverse direction; hollow arrow shows the flow parallel to the row of scales	5
Figure 1.2.3: ‘d’ is the depth of the cavity formed by the scales	5
Figure 1.3.1: Schematic of a tow-tank setup	7
Figure 2.1.1: Wall cavity model, Weiss [8]	10
Figure 2.1.2: Streamlines of flow over a cavity with infinite depth, Takematsu [9]	10
Figure 2.1.3: Streamlines obtained from flow visualization at low across cavity of AR (a) 0.5 (b) 1 (c) 2 (d) 3, Re 0.01, Taneda [14]	11
Figure 2.1.4: Time-mean Streamlines for cavity of AR 4, Re 1.1×10^5 , Zhang [10]	11
Figure 2.1.5: Shen’s [4] simulation of Taneda’s [14] flow visualization for cavity of AR (a) 1 (b) 2 (c) 3 (d) 4, Re 0.01	11
Figure 2.1.6: Streamline Contours of flow over angled cavities of (a) 45° AR 2, Re _d 10, (b) 45° AR 2, Re _d 100, (c) 22° AR 3, Re _d 10, (d) 22° AR 3, Re _d 100, Leibenguth [5]	12
Figure 2.1.7 (a): Sequence of instantaneous streamline plots for Re _d 100, Savoie [12]	13
Figure 2.1.7 (b): Sequence of instantaneous streamline plots for Re _d 624, Savoie [12]	14

Figure 2.2.1: Eddies acting as fluid bearing, Scholle [11]	17
Figure 2.2.2: Cavity vortex for $l = d = 1$. Gatski and Groch [6]	17
Figure 2.3.1: Couette flow composed of stationary cavity embedded plate on bottom and sliding smooth plate on top	19
Figure 2.3.2: C_d vs Re on log scale for flow over flat plate with embedded cavity, Jones [3]	20
Figure 2.3.3: C_d vs Re on log scale for flow over flat plate with fins, Jones [3]	21
Figure 2.3.4: ΔD vs Re for various cavity geometry and orientation on Couette flow. [2][3][5]	22
Figure 2.3.5: Non-dimensional shear comparison along the top plate position as a function of cavity length for a) Re_d 1 b) Re_d 10 and c) Re_d 100 for 90° cavity and AR1, [5]	23
Fig. 3.1.1: Experimental setup	26
Fig. 3.1.2: Displacement vector using correlation of two images in DPIV	29
Figure 3.1.3(a): Image obtained from experiment with case 1 setup for 90° cavity model of AR 3	31
Figure 3.1.3(b): Image obtained from experiments with case 2 setup for 90° cavity model of AR 3	32
Fig. 3.3.1 (a): Sagittal cut of butterfly wing SEM image	34
Fig. 3.3.1 (b): Butterfly scales	34
Fig. 3.3.2: Smooth and cavity models diagram obtained from Solidworks. Models from top to bottom; flat plate, 90° AR 2, 90° AR 3, 45° AR 2, 45° AR 3, 22° AR 2 and 22° AR 3 ...	36
Fig. 3.4.1.1(a): Velocity profile comparison of experimental, computational, and theoretical laminar boundary layer flow at Re_d 3.5	37
Fig. 3.4.1.1(b): Velocity contour of u-component of velocity from computational result for Re_d 3.5	39

Fig. 3.4.1.1(c): Velocity contour of u-component of velocity from experimental data for Re_d 3.5	39
Fig. 3.4.1.2(a): Velocity profile comparison of experimental, computational, and theoretical laminar boundary layer flow at Re_d 70	40
Fig. 3.4.1.2(b): Velocity contour of u-component of velocity from computational result for Re_d 70	41
Fig. 3.4.1.2(c): Velocity contour of u-component of velocity from experimental data for Re_d 70	41
Fig. 4.1.1: Cavity vortex visualization for models with rectangular cavity of AR 2 for (a) Re_d 3.5, (b) Re_d 8.5, (c) Re_d 70 and (d) Re_d 170	45
Fig. 4.1.2: Cavity vortex visualization for models with rectangular cavity of AR 3 for (a) Re_d 3.5, (b) Re_d 8.5, (c) Re_d 70 and (d) Re_d 170	46
Fig. 4.1.3: Cavity vortex visualization for models with cavity wall inclination of 45° and AR 2 for (a) Re_d 3.5, (b) Re_d 8.5, (c) Re_d 70 and (d) Re_d 170	47
Fig. 4.1.4: Cavity vortex visualization for models with cavity wall inclination of 45° and AR 3 for (a) Re_d 3.5, (b) Re_d 8.5, (c) Re_d 70 and (d) Re_d 170	48
Fig. 4.1.5: Cavity vortex visualization for models with cavity wall inclination of 22° and AR 2 for (a) Re_d 3.5, (b) Re_d 8.5, (c) Re_d 70 and (d) Re_d 170	49
Fig. 4.1.6: Cavity vortex visualization for models with cavity wall inclination of 22° and AR 3 for (a) Re_d 3.5, (b) Re_d 8.5, (c) Re_d 70 and (d) Re_d 170	50
Fig. 4.2.1: Control surface ABDCA for calculating surface drag along the length AC	51
Fig. 4.2.2(a): Drag coefficient per unit width vs lower Re_d	53
Fig. 4.2.2(b): Percentage change in surface drag coefficient for various low Re_d	54
Fig. 4.2.3(a): Drag coefficient per unit width vs higher Re_d	57
Fig. 4.2.3(b): Percentage change in surface drag coefficient for various higher Re_d	58
Fig. 4.2.4: u-velocity profile at the center of cavity for all the models at Re_d 8.5	61

Fig. 4.2.5: u-velocity distribution on the top of a cavity for all the models at Red 8.5	62
Fig. 4.3.1: Percentage change in surface drag coefficient for various low Re_d with the error bars	66
Fig. 4.3.2: Percentage change in surface drag coefficient for various high Re_d with the error bars	67
Fig. A1: Thrust vs speed for different types of A-LST models, Zaber industries [1]	77
Fig. B1: Processing window from Insight 4G	78
Fig. B2: Post processing window from Insight 4G for the vector validation and the vector conditioning	79
Fig. C1 Distribution of surface pressure coefficient for a) elliptical nose profiles b) double arc nose profiles $r/t = 0.5$ c) $r/t = 0.25$, Davis [7]	81
Fig. C2: Distribution of boundary layer parameter for elliptical nose, Davis [7]	82
Fig. C3: LE of the smooth flat plate	82
Fig. D1: 2D smooth flat plate model	83
Fig. D2: Domain and Mesh of the fluent simulation with the meshing parameters	84
Fig. D2: Mesh statistics	85
Fig. F1: The user interface of the VI file	97
Fig. F2: The block diagram of the VI	98

CHAPTER 1

INTRODUCTION

1.1 OVERVIEW

Bio-inspired engineering offers the potential to utilize solutions to fundamental problems that nature may have already solved. A butterfly's unique flight mechanism and morphological design makes them a frequently researched insect in bio-inspired engineering. This study is inspired by the Monarch butterfly which undergoes impressive migration from Canada and the United States all the way to Northern Mexico during the winter [15]. Their migration path in North America has been extensively tracked by sightings of Monarch roosts along the suspected passing locations of Monarch butterflies during the overwinter migration [16, 17]. During the spring, the sightings of Monarch butterflies in the United States and Canada suggest that they migrate back to their original locations [18].

Although butterflies have a complex rotational and flapping flight mechanism [19, 20], an important aspect of migratory flight includes gliding flight by riding the wind currents. Figure 1.1.1 shows a continuous leading edge vortex that extends from tip of one wing to another [13]. The wing span of a Monarch butterfly ranges from 8.9 cm to 10.2 cm [21], its weight ranges from 0.1 to 0.75 grams [22] and it has a flight velocity of around 9 km/hr [23]. The flight Re_L of the Monarch butterfly is around 15,400 which maintains a laminar boundary condition over the wings because the value is much lower than the upper limit of 500,000 for

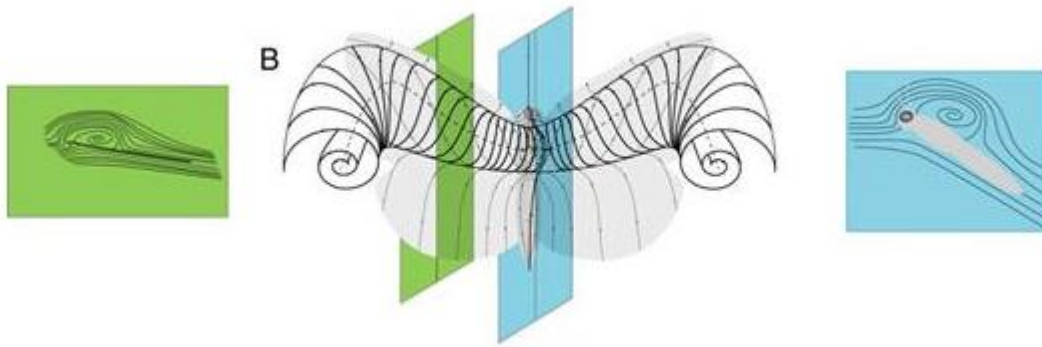


Figure 1.1.1 A continuous leading edge vortex formed over a butterfly [13]

the transition to turbulence. A Monarch butterfly is a very light weight insect with a relatively large wing surface area that flies with a very viscous laminar flow condition. In such a scenario, the skin friction drag becomes a major contributor to the total drag experienced by the butterfly during its flight. This study draws inspiration from the potential mechanism which nature may have evolved through the scales covering the Monarch butterfly's wing to reduce the surface drag. This study is interested in the flow properties associated with the flow over a wing of a

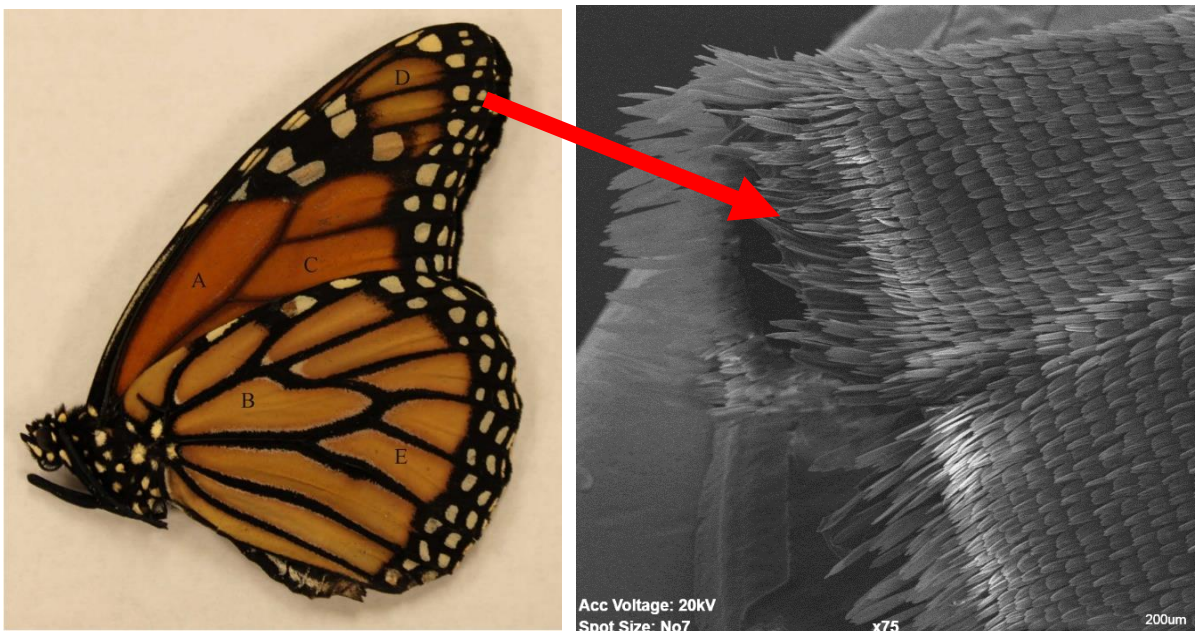


Figure 1.1.2 Scales of Monarch butterfly

Monarch butterfly experienced largely during gliding flight. A closer look at the wings of a Monarch reveals miniscule scales protruding outwards from the wing surface, which arranged together form roof-like shingles as shown in figure 1.1.2. This alignment creates open grooves between subsequent rows of scales.

A collaboration with a biologist Dr. Philip Motta and Laura Habegger and their observations of on a SEM microscope revealed that these scales are on the order of 100 μm and vary in sizes and structure depending on wing location. Scales closer to the body are relatively larger and have a definitive curvature, whereas the scales towards the wing tip show more inclination and are straighter. The wings of a butterfly into which the scale is anchored are transparent, and it is the structural colors generated from the scales that result in such a rich and colorful appearance of the butterfly [24]. Beside the appearance, the scale covering serves to inhibit contamination and the hydrophobic nature to keep the wings dry [25-27]. The purpose of this study is to discern if the natural arrangement of scales form grooves that might serve an aerodynamic purpose as well by altering the laminar skin friction drag.

1.2 MOTIVATION

An experimental study carried out by Slegers [28] confirmed the beneficial effect of scales on the climbing free flight of live Monarch butterflies. Their study included 246 individual climbing flights of 11 live butterflies. Each of the butterfly's flight were tracked by placing markers on the forewings and the flight efficiency was calculated based on energy spent and number of flaps required by the butterfly to reach a certain height. The experiments were repeated first with the scales and then with the scales gently brushed off, in a natural environment.

Figure 1.2.1 shows the comparison of the climbing efficiency (energy change in joules/flap) of the butterfly with and without the scales and found that there was a mean decrease of 37.8% when the scales were gently removed. The study concluded that there was

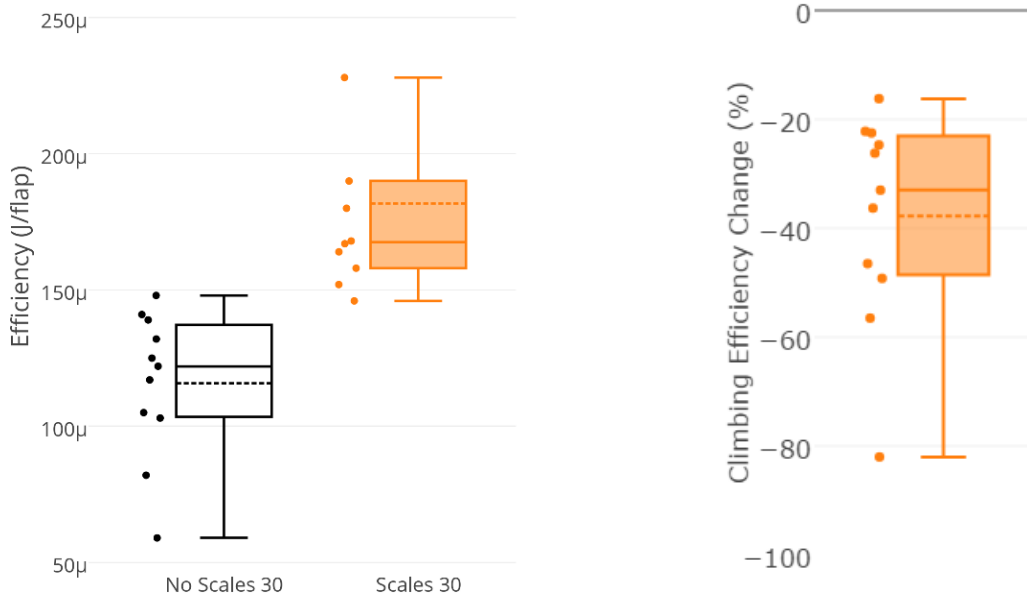


Figure 1.2.1: Comparison of efficiency for cases with and without scales of Monarch butterfly. Solid line shows the mean values

convincing evidence that the butterfly scales and surface patterning may have an aerodynamic function and inspired the question of how the scales help the butterfly achieve a more efficient flight. It is hypothesized that the grooves formed by the arrangement of scales with respect to the flow direction over the wing have the potential to reduce an important component of drag over the wing – specifically the skin friction drag. The primary motive of this research is to validate the hypothesis that flow along the transverse direction with respect to scale orientation results in skin friction drag reduction at low Re_d .

When the flow direction is parallel to the rows of scales as shown by the hollow arrow in figure 1.2.2, it is surmised that the skin friction drag increases due to an increase in wetted surface area from the scales. However, when the direction of flow is transverse to the rows of scales as shown by the solid arrow, an embedded vortex is formed inside each of the cavities, and the outer flow passes over the vortices formed. Each vortex is expected to remain inside the cavity if the Re_d is lower than a critical value (hypothesized to be around 100). The cavity Re_d is defined as a function of freestream velocity and depth of the cavity formed by the scales as shown in figure 1.2.3.

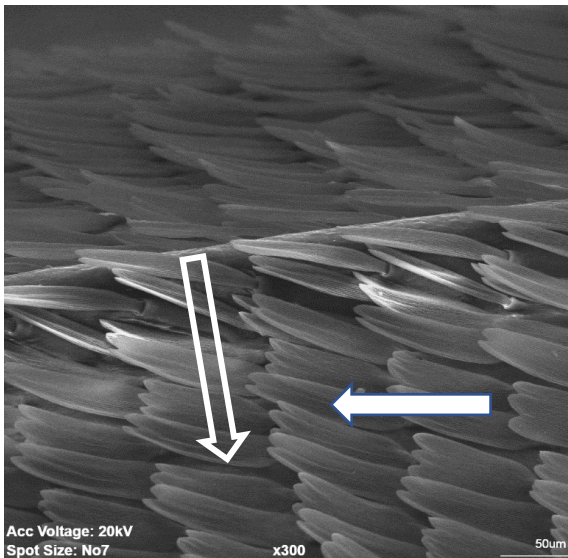


Figure 1.2.2: Solid arrow shows the flow in transverse direction; hollow arrow shows the flow parallel to the row of scales

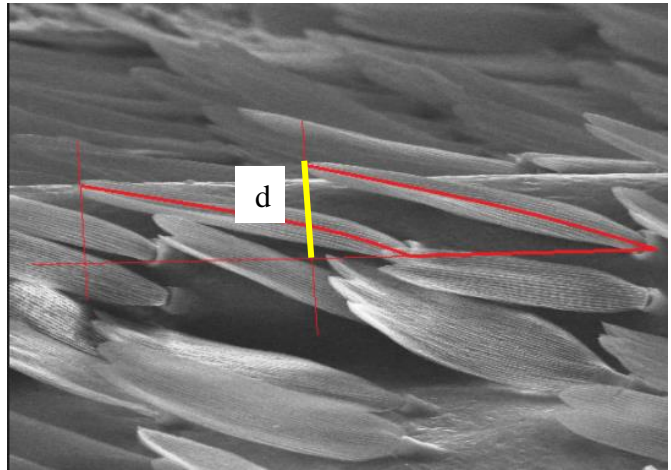


Figure 1.2.3: 'd' is the depth of the cavity formed by the scales

If the vortex remains trapped inside the cavity as the outer boundary layer flows above it, the flow experiences reduced skin friction when compared to laminar flow over a smooth flat surface. Bushnell [29] called this phenomenon the “roller-bearing effect” because the vortices act as rollers to the outer flow passing over them. This explains the fluid dynamic

mechanism by which skin friction drag reduction could be achieved for flow over a series of transverse cavities in comparison to typical flat plate flow.

1.3 OBJECTIVES

At first, this study documents the “roller-bearing effect” for a boundary layer flow over a plate embedded with rectangular cavities (AR 2:1). Next, using a momentum analysis for the measured boundary layer profile over both the cavity plate and a smooth flat plate, the potential for surface drag reduction is calculated. It is hypothesized that as the cavity Re_d increases beyond a critical value, the embedded vortex becomes unstable and begins to mix with the outer boundary layer flow leading to a drag increase because of the exchange of higher momentum fluid from the outer boundary layer with lower momentum fluid inside the cavity. This suggests that the surface drag reduction achieved through the roller-bearing effect is only possible up to a certain critical cavity Re_d . Therefore, this study also aims to document the critical Re_d region beyond which the mixing starts to occur, and the roller-bearing effect is lost.

The objectives of this study are summarized as follows:

- i. Design an experimental procedure and setup to emulate steady boundary layer flow over various flat plate models in a tow-tank facility, permitting the use of both water and higher viscosity oil for Re_d variation. Figure 1.3.1 shows the schematic diagram of the tow-tank setup that used to conduct this study. The equipment setup is explained in detail on chapter 3.

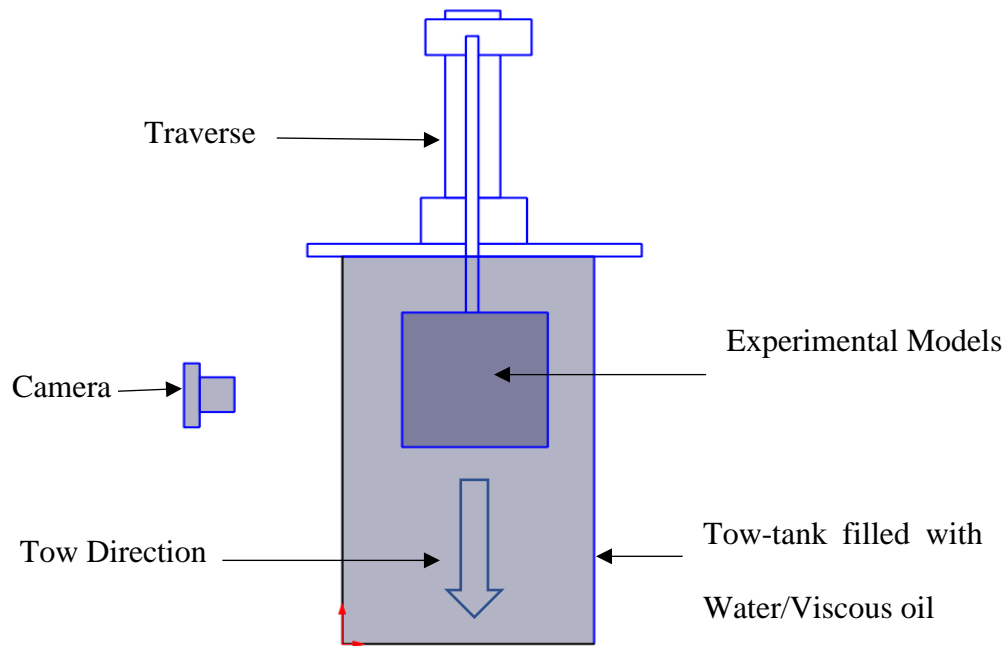


Figure 1.3.1: Schematic of a tow-tank setup

- ii. Perform tests on a rectangular cavity geometry of AR 2: 1 to determine the critical cavity Re_d region where the embedded vortex ejects out and mixes with the outer boundary layer flow.

Quantify the potential surface drag reduction due to the roller bearing effect for the lower cavity Re_d range, and an increase in surface drag for a Re_d range at and above the critical value region.

- ii. Compare the potential surface drag reduction and critical Re_d for various cavity geometries, with angled models below 90° inspired by the Monarch butterfly scale patterning. Models consist of cavities with wall angles of 22° , 45° and 90° and with a variation of AR 2:1 and 3:1. It is hoped that of the geometries tested, the cavity

geometry that achieves the maximum surface drag reduction will be identified. Further details on the models considered for this study is explained on Chapter 3.

- iii. Initial experiments are performed in water for higher cavity Re_d values. Experiments are then repeated for the same models in Silicone Oil of viscosity 20 cSt to permit a lower cavity Re_d regime which matches the butterfly flight cavity Re_d range of 5 to 25.

1.4 DISSERTATION ORGANIZATION

The dissertation consists of five chapters. Chapter 2 reviews the relevant previous work that relates to the objectives of this study. This consists of past research performed to study the vortex formation within a cavity, the effect of a cavity embedded vortex on the flow and the surface drag due to presence of cavity vortex. Chapter 3 includes the experimental setup and the methods that are followed to achieve the objectives. It explains about the choice of models, data acquisition plan using DPIV, along with data validation and an uncertainty analysis associated with the experiments. Chapter 4 includes results and discussion and starts with the visualization of cavity vortex for various cavity geometries. The second half of this chapter includes the comparison of surface drag associated with different cavity models and a smooth flat plate. This chapter also documents the critical cavity Re_d , which represents the upper limit for potential of surface drag reduction through the roller bearing effect. Chapter 5 summarizes the results and concisely states the conclusions of the experimental work.

CHAPTER 2

LITERATURE REVIEW

Studies showing interest in the aerodynamics related to butterfly flight date back to research performed by Nachtigall [30], in which the beneficial aerodynamic effect of butterfly scales was first documented. Nachtigall experimented using dead specimens in a wind tunnel under gliding conditions and attempted to determine the lift and drag. His results indicated that with the presence of scales, the lift increased by 15%. Likewise, a study conducted by Slegers [28], as previously mentioned, demonstrated the beneficial effect of scales on forward climbing flight of Monarch butterflies. In this study, Slegers placed markers on the wings of the butterfly and was able to count the number of flaps required to reach a certain height. The climbing efficiency measured in terms of joules per flap, was an indication of energy required to reach a certain height. The results demonstrated that without the scales, the mean climbing efficiency decreased by 37.8%. These studies indicate that the scales have a beneficial effect on the flight of a butterfly but offer no real explanation as to how.

2.1 VORTEX FORMATION IN A CAVITY

Before we can understand the beneficial effects of low Re_d micro-cavities with orientations inspired by butterfly, we need to understand the previous work done to study the formation of an embedded vortex as the flow passes over a cavity surface. Weiss [8] formulated the problem of flow in a cavity at low Re_d and conducted an experiment on a model with square

cavity as in figure 2.1.1 at Re_d 150. He performed flow visualization of a single cavity embedded plate by allowing it to fall in a glycerin solution, resulting in a flow parallel to the plate and over the cavity opening. Weiss concluded that his assumption of considering the dividing streamline between the outer flow and the cavity vortex as an approximate straight

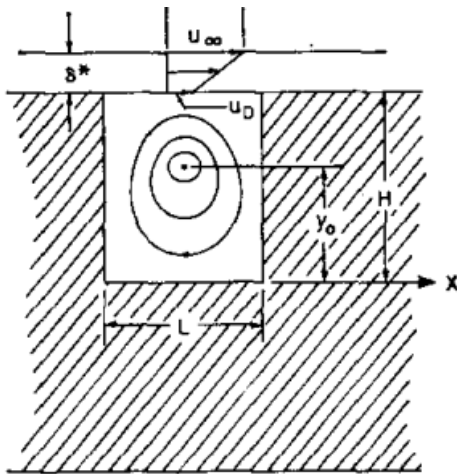


Figure 2.1.1: Wall cavity model, Weiss [8]

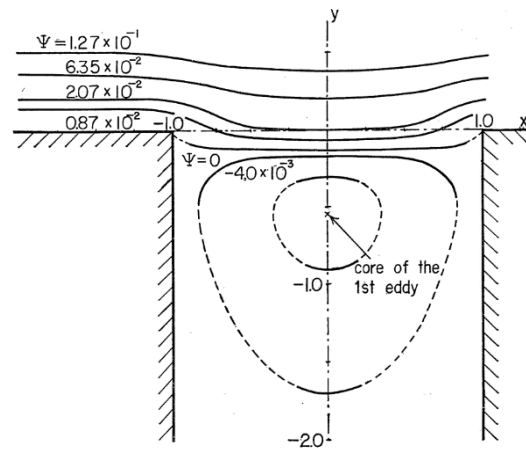


Figure 2.1.2: Streamlines of flow over a cavity with infinite depth, Takematsu [9]

line was valid for Re_d 150. He also inferred that the dividing streamline would have a curvature as the Re_d approached zero. Takematsu [9] studied flow over a cavity with infinite depth, based on Stokes approximation in a slow viscous condition to determine the flow pattern near the cavity entrance. He found that the dividing streamlines have a definite curvature for the low Re_d flows as shown in figure 2.1.2. Flow visualisation performed by Taneda [14] as in figure 2.1.3 shows that a variation in cavity aspect ratio changes the shape of the vortex formed in the cavity. The results for Re_d 0.01 showed that up to AR 2, there is a single dominant vortex which forms inside the cavity. As the AR increased to 3, the vortex stretched enough to be separated into two corner vortices such that the outer flow dips down and closer to the cavity

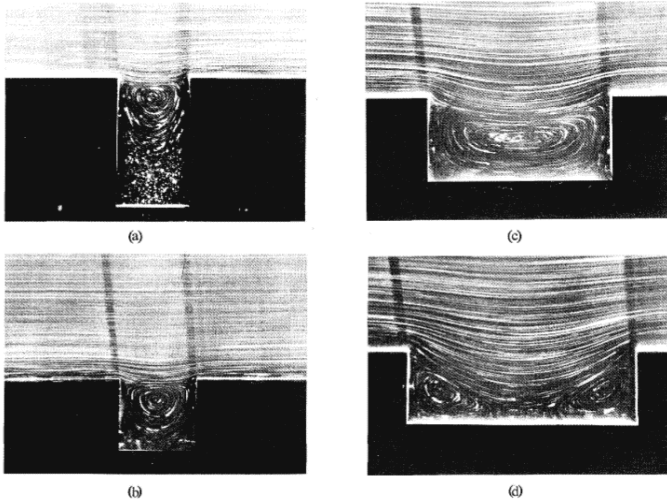


Figure 2.1.3: Streamlines obtained from flow visualization at low across cavity of AR (a) 0.5 (b) 1 (c) 2 (d) 3, $Re\ 0.01$, Taneda [3, 14]

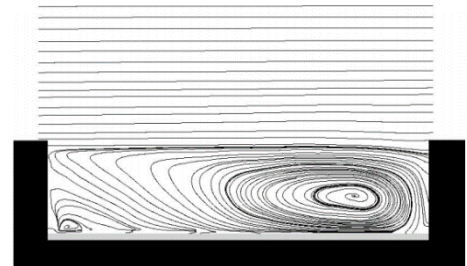


Figure 2.1.4: Time-mean Streamlines for cavity of AR 4, $Re\ 1.1 \times 10^5$, Zhang [10]

bottom. However as the Re_d increases, the flow is again dominated by a single large vortex with its center shifted towards downstream as Zhang's [10] wind tunnel study showed for flow over rectangular cavities at $Re_d\ 1.1 \times 10^5$ and AR 4 as shown in figure 2.1.4. Shen [4]

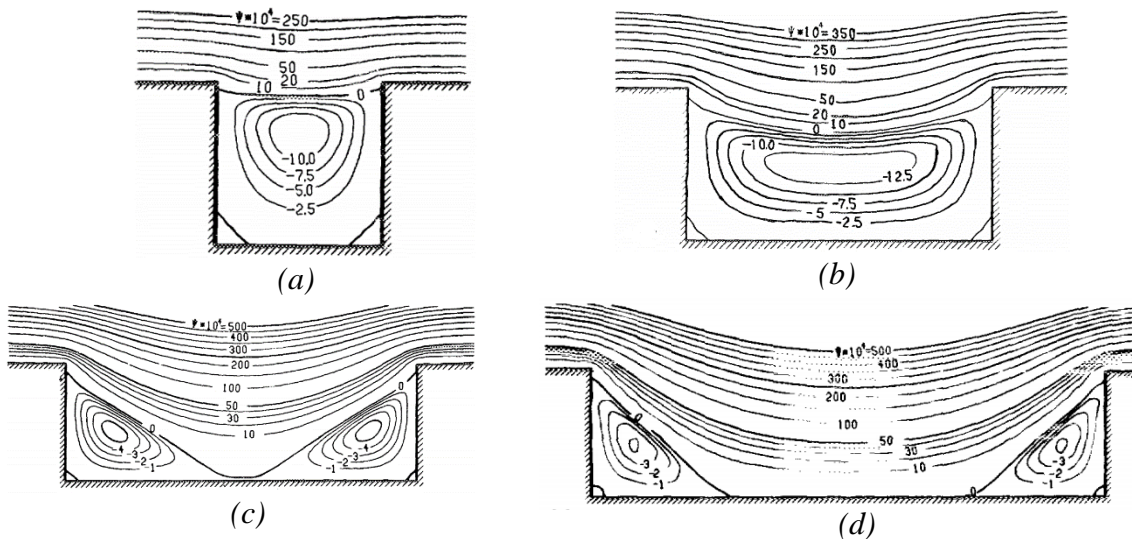


Figure 2.1.5: Shen's [4] simulation of Taneda's [14] flow visualization for cavity of AR (a) 1 (b) 2 (c) 3 (d) 4, $Re\ 0.01$

numerically computed the flow over a cavity and matched the flow pattern of flow visualisation from Taneda [14]. Figure 2.1.5 shows the results from Shen's simulation of Taneda's setup.

Figure 2.1.6 shows the computational results of streamline contours of the cavity vortex for cavity with inclined wall angles [5]. Figure 2.1.6 (a) and (b) shows the contours for 45°

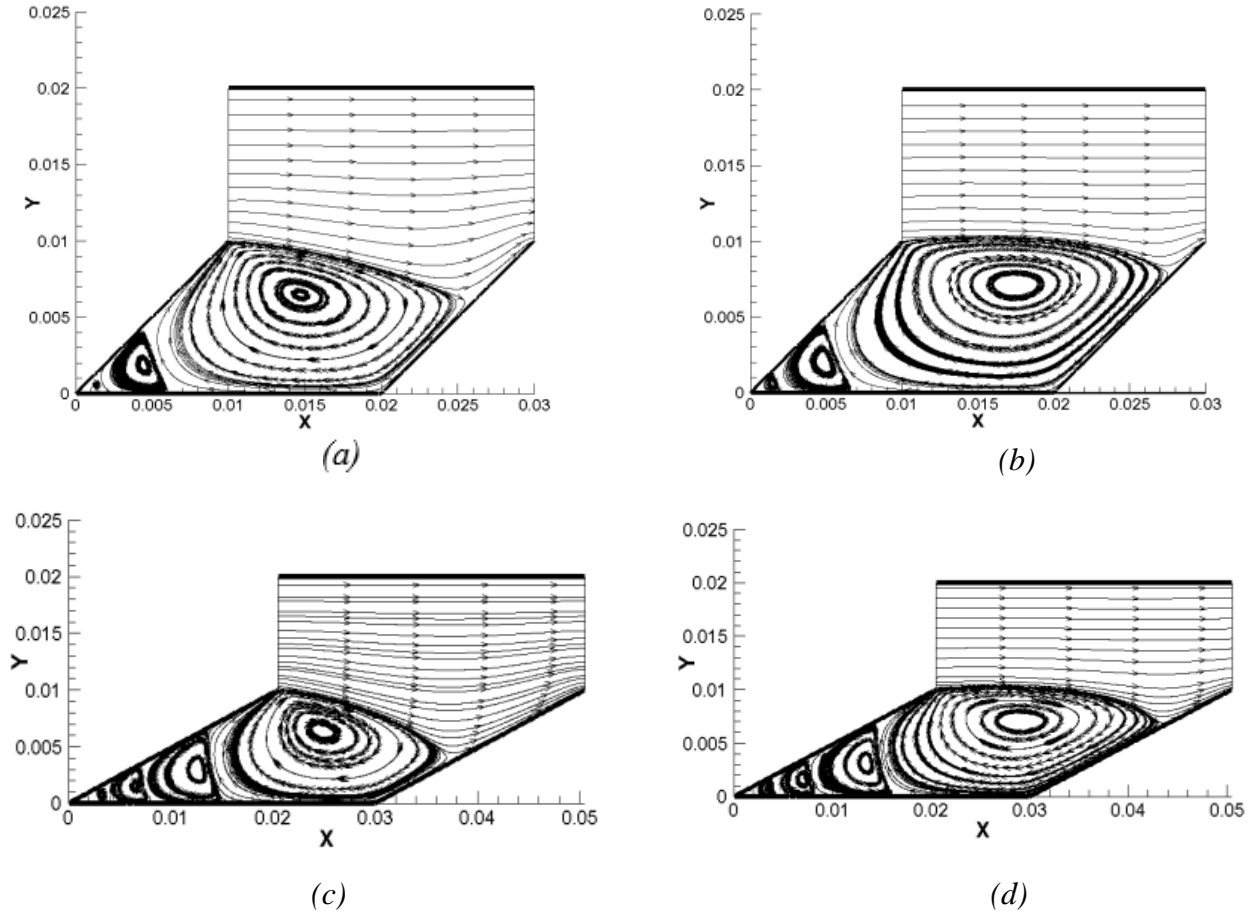


Figure 2.1.6: Streamline Contours of flow over angled cavities of (a) 45° AR 2, Re_d 10, (b) 45° AR 2, Re_d 100, (c) 26° AR 3, Re_d 10, (d) 26° AR 3, Re_d 100, Leibenguth [5]

cavity inclination of AR 2 for Re_d 10 and 100 respectively. The dip of the dividing streamline is not centered and is skewed towards the downstream section. A corner vortex is also formed on the upstream portion of the cavity. Similarly, figure 2.1.6 (c) and (d) shows the contours for 26° cavity inclination of AR 3 for Re_d 10 and 100 respectively. The nature of the vortex formed

is like that of the 45° cavity AR 2 with two distinct corner vortices. Also, the size of the dominant vortex seems to reduce with the decrease in cavity wall inclination.

Chebbi & Tavoularis [31] [32] computationally solved the flow over triangular cavities which they modeled after their own observations of a butterfly scale geometry. They observed the formation of an embedded vortex, but their results were inconclusive that there was any aerodynamic benefit to the presence of scales on the wings. Savoie [12] numerically simulated the flow over a model of triangular cavities found in *Agrotis Moth* wings and found that for Re_d less than 100, there would be a single stationary eddy structure that oscillates around its equilibrium position as shown in figure 2.1.7 (a). However, for Re_d 624, the vortex sheds

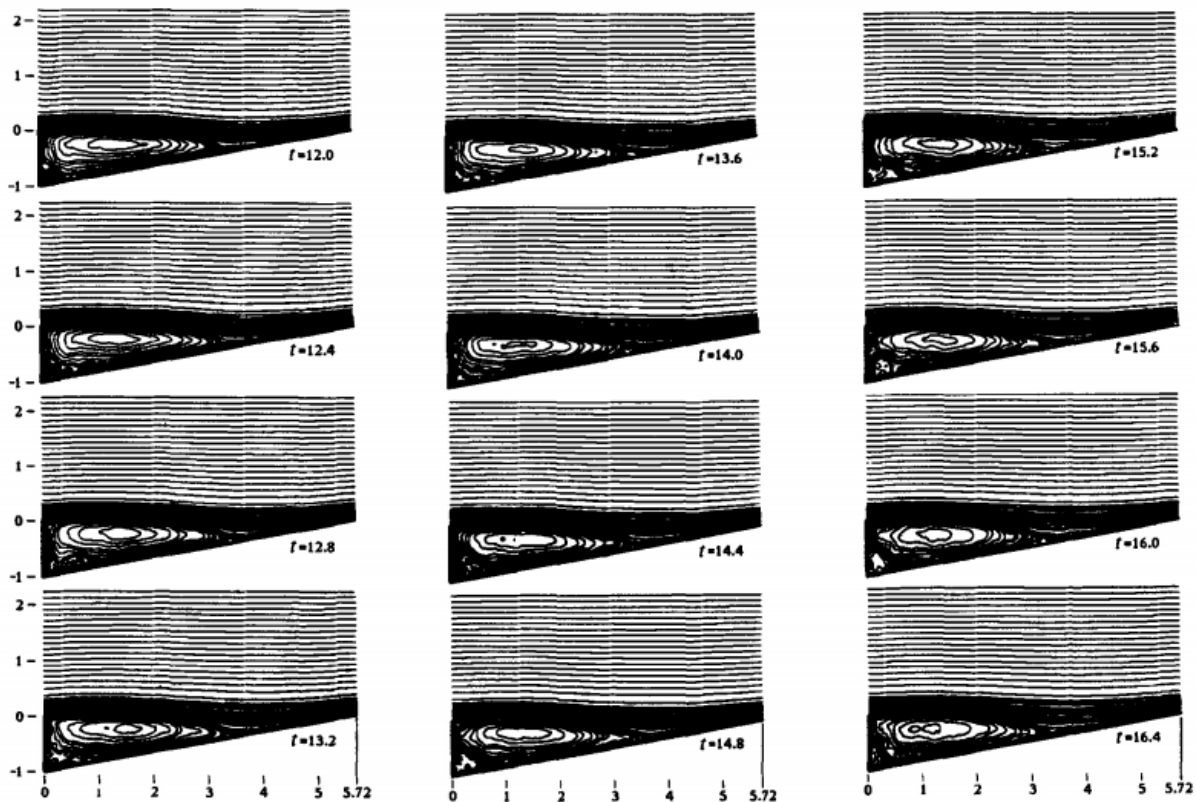


Figure 2.1.7 (a): Sequence of instantaneous streamline plots for Re_d 100, Savoie [12]

towards the downstream of the flow while new vortex is formed on the corner of the cavity

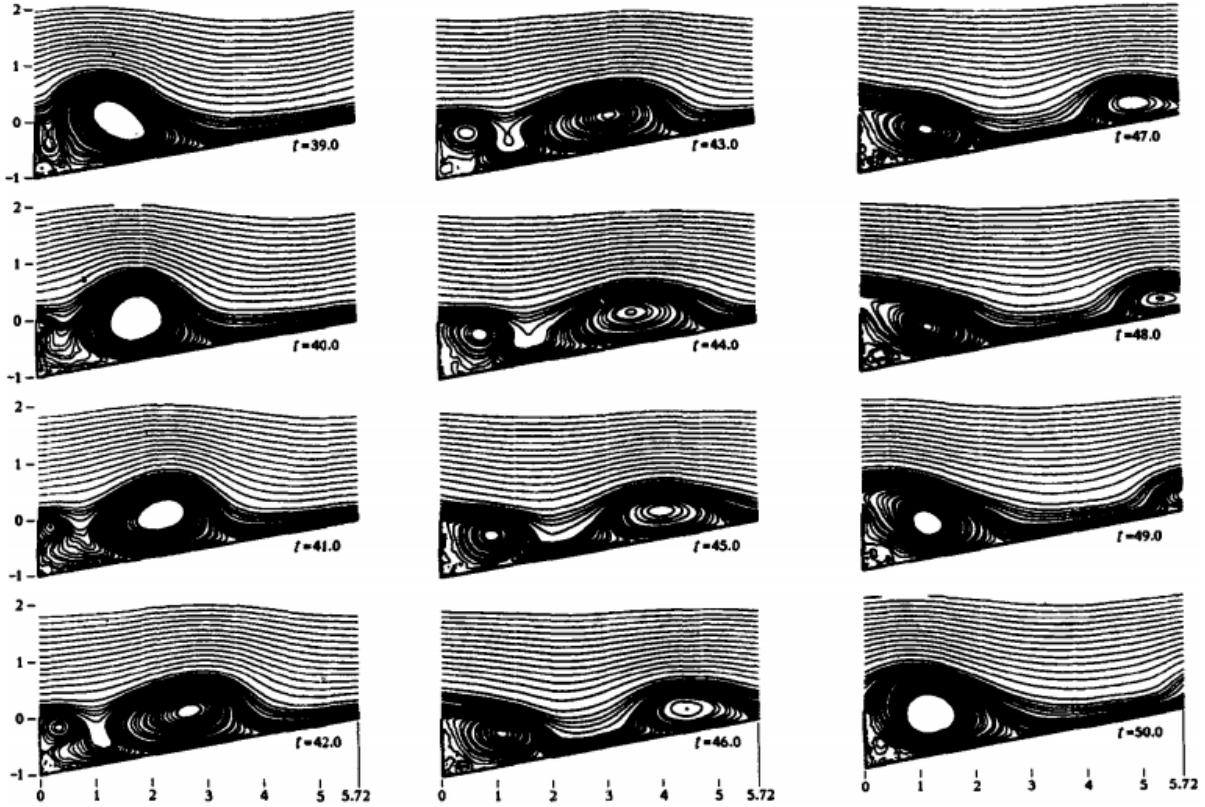


Figure 2.1.7 (b): Sequence of instantaneous streamline plots for $Re_d 624$, Savoie [12]

due to influx of the fluid as shown in figure 2.1.7 (b). Although the model is an asymmetric triangular one, we can still relate this to our work and expect that the embedded cavity vortex to eject out of the cavity at higher Re_d above 100.

2.2 EFFECT OF CAVITY EMBEDDED VORTEX ON BOUNDARY LAYER FLOW

The above studies discuss the formation of a single vortex inside a cavity as the flow passes over it. To understand the effect of the embedded cavity vortex on the outer boundary layer (BL), it is necessary to discuss the origin of BL and the concept of no-slip velocity.

Boundary layer theory began with the paper of L. Prandtl on 1904 [33], *On the motion of a fluid with very small viscosity*. In his paper, Prandtl focused on the behavior of the fluid

close to the wall of the solid boundary. He mentioned that the flow is approximately irrotational far away from the solid boundary. On the other hand, flow closer to the solid boundary around a small “transitional layer” has a steep velocity gradient which is significant enough to consider the flow as rotational. The thin layer of the fluid closer to the solid interface has the highest velocity gradient because of the assumption that the first layer of fluid adjacent to the wall of solid boundary has zero velocity due to the no-slip condition. The viscous effect of the fluid is only present on the small “transition layer” around the solid wall which was later mentioned frequently as boundary layer by Blasius [34]. The small thickness allows approximation of the governing equations to a simplified version inside the BL. The simplified version of x-component of 2D Navier-Stokes equation is shown as in equation 2.1.

$$\frac{du}{dt} + u \frac{du}{dx} + v \frac{du}{dy} = -\frac{1}{\rho} \frac{dp}{dx} + \nu \frac{d^2u}{dy^2} \quad (2.1)$$

Assuming a semi-infinite plate placed parallel to the flow direction in a steady condition, $p = \text{constant}$ along the x-direction, Blasius calculated the exact solution for the drag coefficient of a flat plate by integrating small steps along the length from equation 2.2.

$$C_d = 1.33(Re_L)^{1/2} \quad (2.2)$$

Eventually, the total skin friction drag per width computed from equation 2.3 represents the momentum loss due to the resistance offered on a viscous fluid by the solid boundary throughout the length of the flat plate.

$$F_d = qLC_d \quad (2.3)$$

In comparison to the skin friction drag offered by the solid boundary of the smooth flat plate, a grooved flat plate is hypothesized to create a lower skin friction drag to the flow under certain scenarios. If the embedded vortex remains trapped within the cavity throughout the

flow, then the dividing streamline between the vortex and the outer BL flow acts as the boundary or wall condition for the outer BL flow. Contrary to the no-slip boundary condition offered by the smooth flat plate, the dividing streamline results in a partial slip scenario which offers less skin friction drag to the outer BL flow. This idea of slip condition was first proposed by Goldstein [35]. Hocking [36], examined the behaviour of two immiscible liquids flowing over a corrugated surface and found that one of the liquids becomes trapped within the waves of the corrugation while the other one slides over it. These studies demonstrated the potential for drag reduction due to presence of a trapped vortex in the cavity for low Re_d flow. The tendency of fluid to slide above the vortex, which results in a partial slip condition for the outer flow, would explain this mechanism for drag reduction [37].

Bushnell [29], later hypothesized about the vortices embedded inside cavities acting to induce a partial slip to the flow and introduced the term “micro-air bearing effect”, comparing this mechanism to a single embedded vortex acting as a mini bearing to the flow above it. According to Bushnell, the presence of a vortex would increase the slip velocity on the outer boundary layer which would contribute to the skin friction drag reduction. However, he also realized that if the vortex mixes with the outer layer, as occurs for larger cavity Re , this effect would no longer be present and instead an increase in drag would occur due to exchange of high momentum and low momentum fluid within the cavity flow. A similar study performed by Scholle [11] also described the eddies inside the cavity acting as fluid roller bearing to the flow above provided that the two regions are separated by a “dividing separatrix”. This study of Stokes flow over a rippled-surface topography showed that, for sufficiently high waviness which caused the formation of an embedded vortex (figure 2.2.1), the mean velocity at the interface is increased by 1% for a single ripple.

As explained by the studies mentioned above, a single entrapped vortex in a cavity could result in a decrease in skin friction drag for the flow gliding over it. The reason for drag reduction is mainly because of a partial slip condition at the dividing streamline between the outer boundary layer flow and inner cavity flow in comparison to a typical flat plate that encounters a fixed wall with no slip condition.

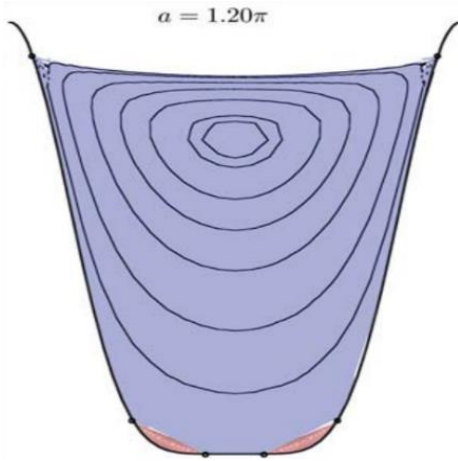


Figure 2.2.1: Eddies acting as fluid bearing, Scholle [11]

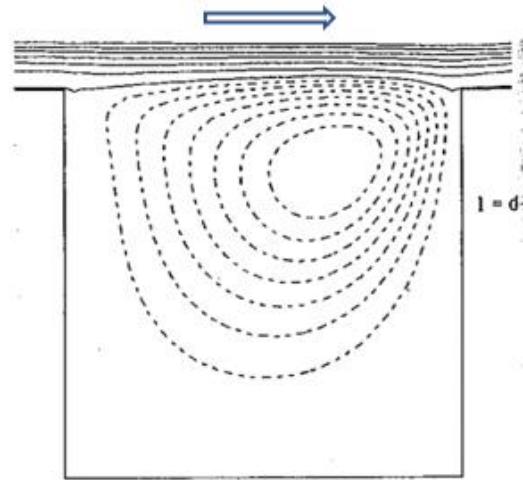


Figure 2.2.2: Cavity vortex for $l = d = 1$. Gatski and Groch [6]

2.3 SURFACE DRAG REDUCTION DUE TO THE CAVITY VORTEX

Gatski and Groch [6] numerically examined the drag characteristics of laminar cavity flow induced to form by the presence of a boundary layer passing above a single square cavity. They varied the cavity AR from 0.25 to 1 boundary layer thickness (δ) and found that throughout cavities with higher AR had a larger vortex embedded in it. For AR greater than 0.5 and $Re_\delta = 1188$, the center of the vortex shifts towards the downstream side of the cavity. Figure 2.2.2 shows the asymmetry of the vortex inside the cavity. Since, a larger portion of the cavity is characterized by a strong recirculating vortex, the interface between the cavity and outer BL flow experiences a local positive acceleration followed by deceleration. So, a local

favorable pressure gradient is induced on the interface towards the downstream section of the cavity due to the vortex underneath. They concluded that the increase in shear stress on the downstream wall rendered any drag reduction due to the presence of a single cavity as minimal overall. However, they did mention that the reduction could be significant for a series of cavities with minimum spacing between them upon which the increased skin friction would act.

In addition, to the laminar boundary layer flow over a cavity, studies have also been performed with different flow scenarios. Wang [38] performed an analytical study of pressure-driven Stokes flow through a channel composed of two parallel grooved plates. Stokes flow is characterized by the low velocity flow typically of $Re \ll 1$ where the viscous forces dominate the inertial forces. Wang's study showed that an increase in slip velocity results in lower drag and it varies with the cavity geometry as well. It also means that there would be an optimum geometry for which the slip velocity and the drag reduction would be maximum.

Wang [39] performed another study using a Couette flow scenario. A typical Couette flow consists of two smooth flat plates placed parallel to the direction of the flow. The lower plate is kept stationary, and the upper plate is moved at a constant velocity such that the velocity profile at any point towards the x-direction is linear. The study of Stokes flow with smooth plate sliding over a finned plate (cavities parallel to the flow direction) showed the drag was higher in comparison to a flat plate condition irrespective to the flow orientation with the fins[40]. They showed the drag increase for the flow parallel to the fins was because of the increase in surface area encountered by the flow. Wang[39] also concluded that for flow transverse to the cavities the drag was higher compared to the flat plate. However, in his study, Wang included the calculation based on the BL height from the bottom of the cavity labeled

as ‘y’ in the figure 2.3.1. As mentioned earlier, if the vortex remains intact throughout the flow, the interface between the cavity and outer BL is considered as the boundary or wall conditions. Thus, distance from the interface to the top plate labeled as ‘h’ should be the correct Couette flow height for this scenario.

Lang and Johnson [41, 42] predicted that from Wang’s [39] theoretical calculations, considering a proper reference height for flow perpendicular to the cavities, 20% drag

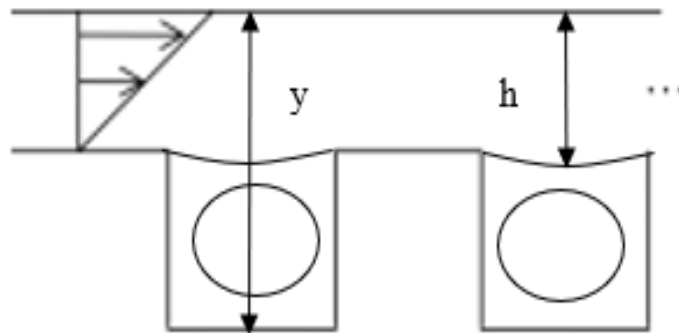


Figure 2.3.1: Couette flow composed of stationary cavity embedded plate on bottom and sliding smooth plate on top

reduction is possible in comparison to a regular Couette flow. Lang and Johnson performed an experimental study of Couette flow consisting of lower plates with cavity surfaces and smooth upper plate. Their Couette flow setup [41] was inspired by Bechert [43], who compared the net change in drag for flow normal to the cavities and flow parallel to the cavities for a finned plate. Lang and Johnson [42] found that the drag reduction is a function of Re_d and for $Re_d < 15$ the drag reduction was in the range of the predicted 20%. The drag reduction decreased with increasing Re_d and for Re_d 20 to 50, the value was only around 3-5%. The cavity model was of AR 1 and they also mentioned that for AR 2, the drag reduction could be higher.

Jones [3], using the same set up as Lang & Johnson [41], studied Couette flow over cavities of AR 2 with wall inclination 45° and its role in drag reduction. Jones found a drag reduction of 35% with the 45° cavity. They also performed experiments with the flow parallel to cavity walls which resulted in net increase of 50% drag due to increase in surface area encountered by the flow. Figure 2.3.2 shows the drag profile of a flat plate and a plate with embedded cavities. Similarly, figure 2.3.3 shows the comparison of flat plate drag results with

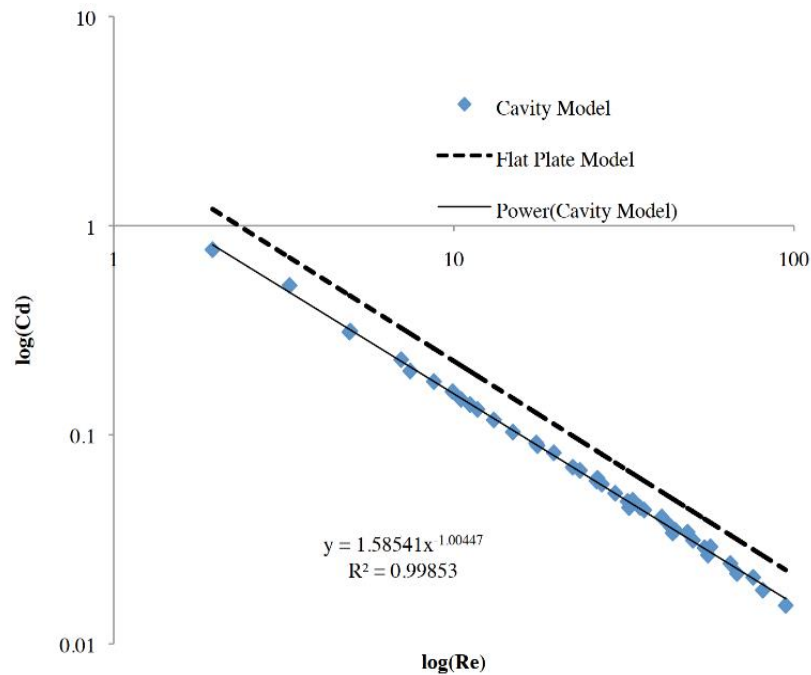


Figure 2.3.2: C_d vs Re on log scale for flow over flat plate with cavities, Jones [3]

the plate with cavity walls arranged parallel to the flow direction. Jones' work also verified that in cavity models the drag reduction occurred for reverse direction of the flow as well. The drag reduction of 35% was higher than expected possibly because of the overestimation on the

correction factor of drag values. The correction factor was included to cancel out the drag from flat surface that Jones' model had which surrounded the cavities on the edges.

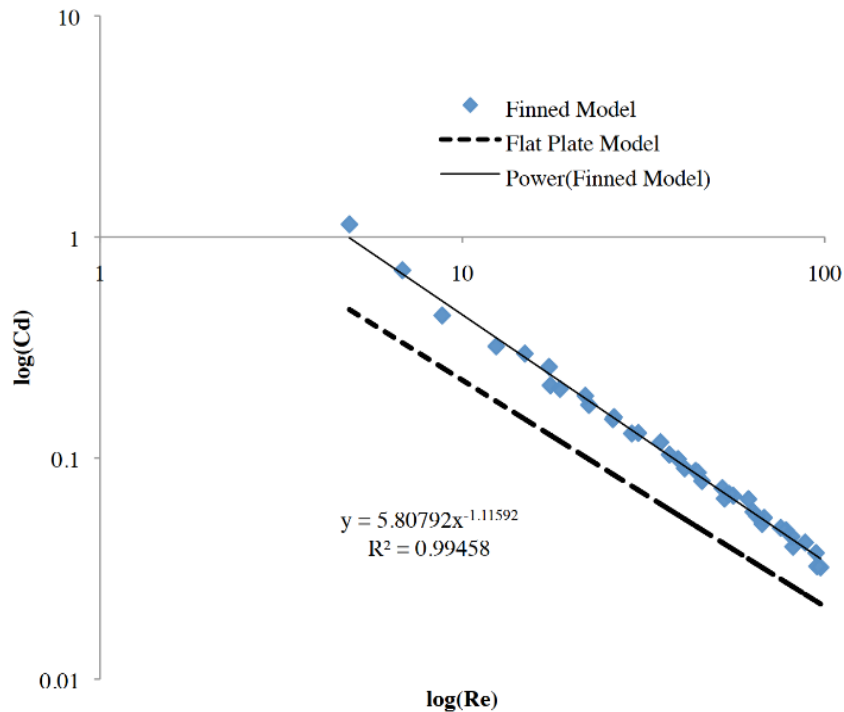


Figure 2.3.3: C_d vs Re on log scale for flow over flat plate with fins, Jones [3]

The effect of change in cavity geometry and orientation on drag reduction for Couette flow conditions are shown in the figure 2.3.4 [2]. The experimental drag reduction for 45° angled cavity AR 2 and 26° angled cavity AR 3 on Couette flow conditions shows higher drag reduction compared to computational results from similar setup. Also, the drag reduction decreases as the flow Re_d increases and the maximum drag reduction is calculated at lower $Re_d < 5$. Although the values from computation and experiment did not match each other, both the studies show drag reduction for flow past a series of cavities.

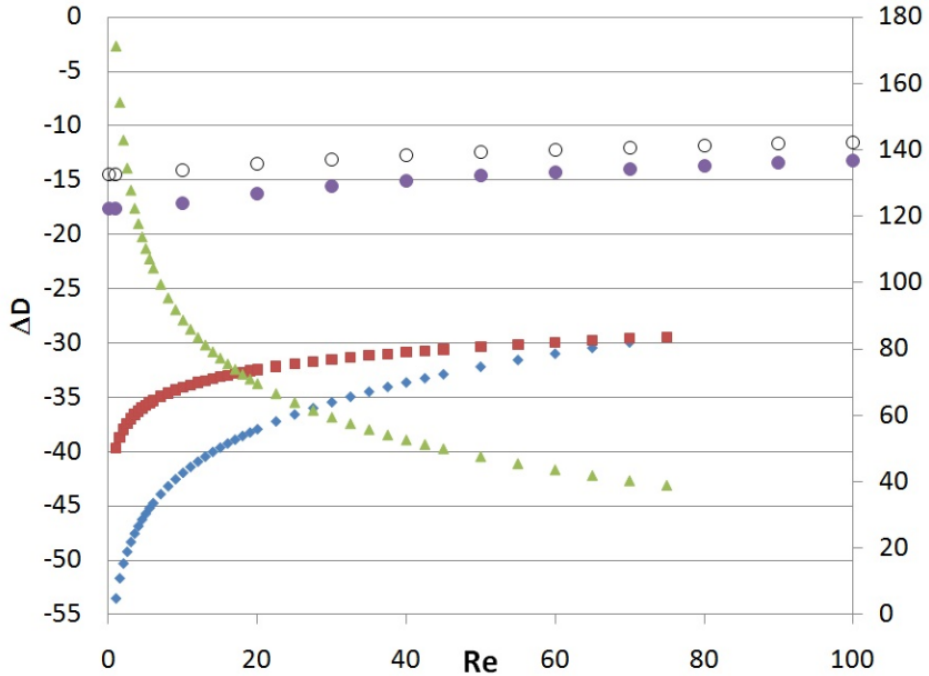


Figure 6: Change in drag measured either experimentally or calculated using FLUENT. Experimental data (only trends in data plotted): (♦) AR=3, 26 deg wall angle, transverse (■) AR=2, 45 deg wall angle, transverse (▲) AR=2, 45 deg wall angle, parallel (use right axis). Computational data: (●) AR=3, 26 deg wall angle, transverse (○) AR=2, 45 deg wall angle, transverse.

Figure 2.3.4: ΔD vs Re for various cavity geometry and orientation on Couette flow. [2][3][5]

Leibenguth [5] attempted to computationally verify Jones' drag reduction results and found that the values were almost half of Jones's [3] experimental results. The reason was the assumption of an infinitely thin cavity wall which resulted in a discontinuity because the velocity at the top of cavity is zero and the adjacent node had to follow a linear profile of the BL flow. Also, as mentioned before, Jones' model was surrounded by a smooth flat plate portion and their experimental results might have overestimated the drag reduction. Leibenguth also verified that there was no directional preference of cavity orientation in the case of flow perpendicular to rectangular cavities, and the shear stress distribution on the dividing streamline changes with an increase in Re_d of the flow. Figure 2.3.5 a), b) and c) shows the

shear stress distribution along the cavity length for Re_d 1, 10 and 100 respectively for 90° cavity with AR 1. From figure 2.3.5, it can be predicted that as Re_d increases above 100, the shear layer between the cavity and outer boundary layer could collapse and mixing between the regions might occur. The model used for the shear comparison is cavity with 90° wall angle with AR 1.

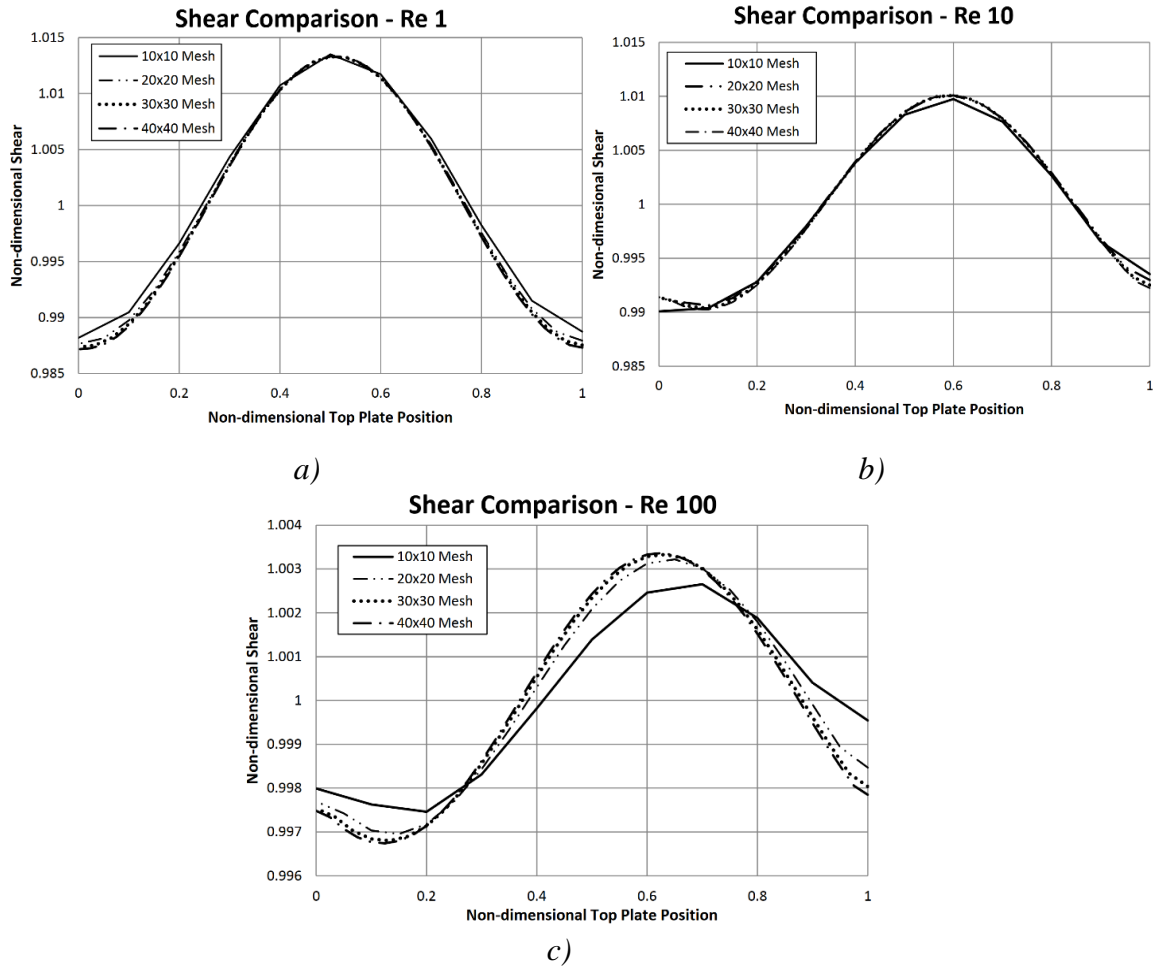


Figure 2.3.5: Non-dimensional shear comparison along the top plate position as a function of cavity length for a) Re_d 1 b) Re_d 10 and c) Re_d 100 for 90° cavity and AR 1, Leibenguth [5]

2.4 SUMMARY

Previous work has demonstrated that the flow passing over a cavity has the tendency to form either a single vortex or multiple corner vortices depending on the size of the cavity. The presence of cavity vortex is attributed to result in a reduced surface friction to the outer BL just as a roller bearing would cause to reduce the friction of the surface sliding over it. This phenomenon was termed as “micro-air bearing effect” or “roller-bearing effect”. The presence of the roller-bearing effect for Couette flow and the resulting surface drag reduction had been quantified both computationally and experimentally. Although the values from computation and experiment did not match, the flow over a cavity embedded flat plate in a Couette condition resulted in reduced surface drag for low Re_d flows.

However, the butterfly’s flight is more comparable with a typical flat plate boundary layer flow. All the former studies mentioned above that involved a boundary layer flow over embedded cavities included flow visualization and qualitative analysis only. This study aims to quantify the potential drag reduction due to cavities embedded in a flat plate for a laminar boundary layer flow. Previous studies had pointed out that the surface drag varies with varying the cavity geometry as well. Although the studies were performed in Couette condition, the results due to the variation in cavity geometry will help provide context to the results of this study of normal boundary layer flow.

CHAPTER 3
EXPERIMENTAL SETUP, MODELS AND VALIDATION

3.1 EXPERIMENT SETUP

3.1.1 Tow tank structures and equipment

Usually an experiment regarding fluid flow is associated with a water tunnel facility. The water tunnel facility located on Hardaway Hall 110 of the University of Alabama has a lower limit of minimum 50 mm/s flow velocity for the experiments to obtain a conclusive result. For this study, Re_d is a function of cavity depth (d), flow velocity and viscosity of the fluid used in the experiments. Experiments performed on water tunnel with the minimum flow velocity of 50 mm/s on models with cavity depth 3.5 mm results in Re_d 175. Since we are interested in butterfly's flight Re_d regime of 5 to 25, experiments are conducted on tow tank facility located in Hardaway Hall 103 of the University of Alabama. Tow tank is preferred for low speed flows because the speed of the traverse that tows the plates, sets the flow Re_d , which allows us to experiment in lower Re_d .

The tow tank is 152.4 cm high, 91.4 cm long and 60.9 cm wide. It is made up of plexiglass and has 2.54 cm thickness. Figure 3.1.1 shows the setup which consists of the vertical tow tank 80/20 t-slotted extruded aluminum bars, the structures, and the arrangement of optics along with the laser for experiments using DPIV (Digital Particle Image Velocimetry). A structure rests on the top of the tank which consists of a linear drive traverse

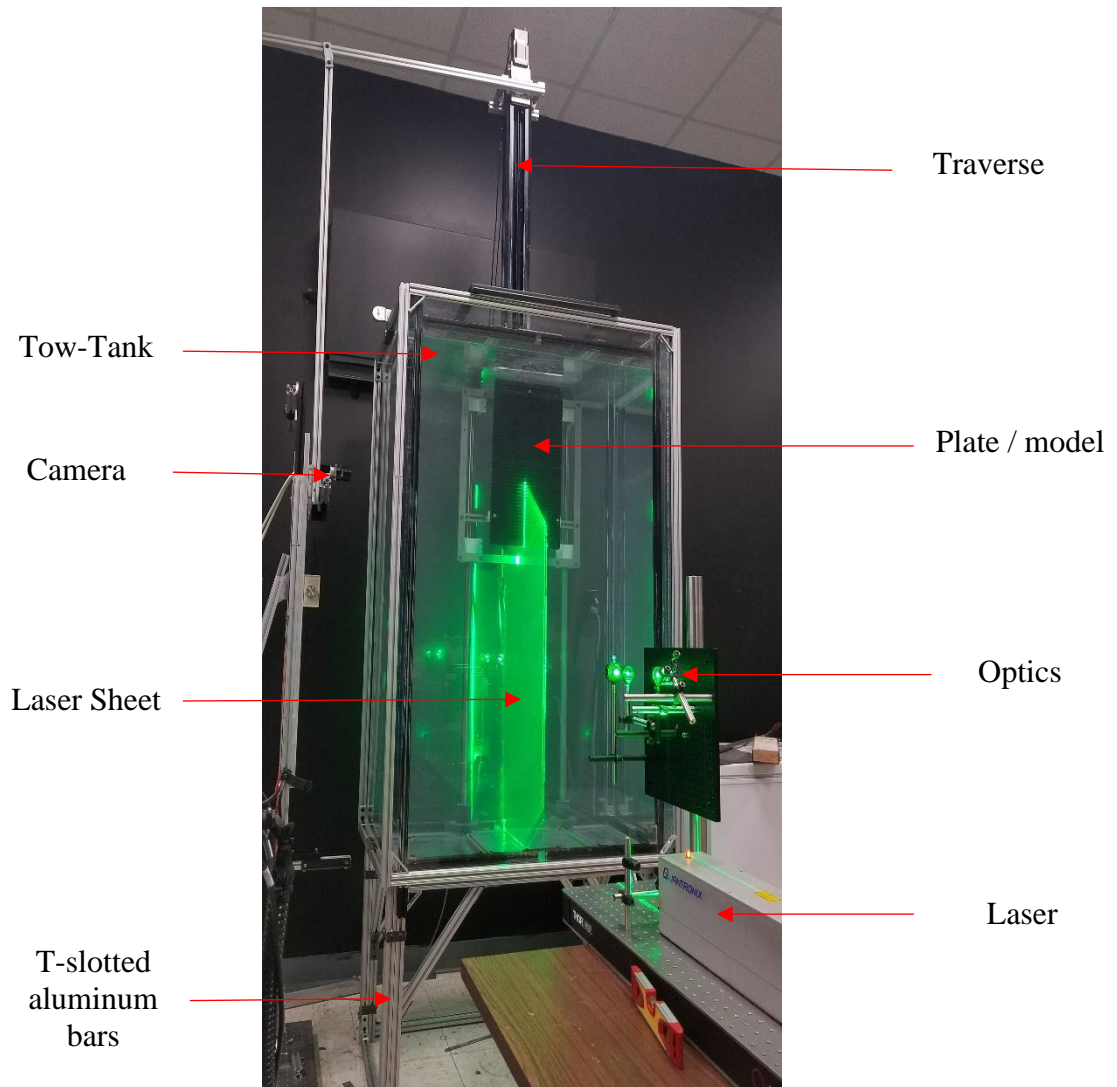


Figure 3.1.1: Experimental setup

and a vertical aluminum bar that connects the traverse carriage to the plate to be towed. An L-bracket connects the traverse carriage to the camera on the side of the tow tank such that the plate and camera has the same velocity when towed. The inside of the tank consists of two vertical stainless-steel rods that acts as guide rails to the linear bearings attached to the corners of the plate. This design ensures that the plate moves in a vertical path with the minimum vibration as possible.

The following are equipment involved in the experimental setup:

- 1) Fluid: Initially, the experiments are performed in water at around 20° C and kinematic viscosity of $1.003 \times 10^{-6} \text{ m}^2/\text{s}$. For low Re_d data, experiments are performed in a high viscous mineral oil from US Lubricants known as Prima 100 (Star 4) of viscosity 20 cSt which is equal to $2.006 \times 10^{-5} \text{ m}^2/\text{s}$.
- 2) Quantronix Darwin series 527-30-M Nd:YLF Laser: This is a diode-pumped solid-state class IV discrete laser (527 nm) with an adjustable Pulse Repetition Frequency (PRF Hz) which is set to match the camera acquisition rate.. The operational current range of the laser is from 16 to 30 A and the current input value depends on the experiment. The laser is water cooled by a separate cooling system that maintains the coolant outflow temperature to remain below 23° C as the coolant regulates the core temperature of the laser head.
- 3) Optics: The set of optics consists of special purpose mirrors that reflect the 527 nm laser beam and a pair of convex lenses of focal length 40 mm and 100 mm to increase the intensity of the laser beam. The diameter of the beam emitted from the laser source is 2.5 mm and as it passes through the pair of convex lenses, the beam is reduced to a diameter of 1 mm. Finally, the concentrated beam hits the cylindrical concave lens that converts the single cylindrical beam into a 2D vertical laser sheet of 1 mm thickness. The width of laser sheet can be adjusted at the expense of its brightness.
- 4) Zaber ALST0750B-E01-KT07U: This is a motorized linear stage lead screw drive system high load traverse produced by Zaber Technologies. It has a maximum travel distance of 750 mm. However, for our study, the usable towing distance is limited to 675 mm due to structural limitations on the tow-tank. The maximum usable speed of

the traverse for our study is determined to be 45 mm/s which sets the upper limit of the Re_d for the experiment. More details of the traverse are provided on Appendix B.

- 5) Basler A2000-340km camera: This is a c-mount camera-link CMOS high speed camera that can capture images at 340 FPS at 2048 pixels x 1088 pixels resolution. The FPS of the camera is set to match the PRF of the laser to ensure consistent brightness throughout the series of images captured. Depending on the experiments, the camera is coupled with lenses of 50 mm and 25 mm focal length and f1.4 aperture size.

3.1.2 DPIV

The development of DPIV dates back to the laser Doppler anemometry, which utilizes the scattered light from an illuminated particle to obtain its displacement at a single location [44]. In solid mechanics, Laser Speckle Velocimetry (LSV) uses the speckle-patterns formed by the light scattered from solid surfaces to obtain displacement measurements on the whole surface [45]. Articles written by Dudderar and Simpkins [46], Barker and Fourney [47] explains how the LSV could be used in the field of fluid mechanics to obtain a full velocity field. The basic principle is that a double pulsed speckled photograph of seeded liquid would give a distinct Young's fringe pattern that would contain information to calculate velocity field. Adrian [48] mentioned that a perfect fringe pattern from LSV required high density seeding of the particles. Further studies in utilizing the scattered light from the particles and photographic image led to the development of Particle Image Velocimetry (PIV) [48-50]. PIV provides accurate results even for low density of seeding particles in the fluid. Digital Particle Image Velocimetry (DPIV) utilizes the technique of PIV with digitally acquired images which

requires a different method for particles correlation in subsequent images to obtain the velocity field [51, 52].

DPIV is used to obtain a 2D velocity field from an image series of the test section filled with seeding particles. The tow tank is seeded with neutrally buoyant, silver-coated, hollow glass spheres, which has an average diameter of $14\ \mu\text{m}$. These seeding particles have reflective properties that are visible in the test section when illuminated with the 2D laser sheet. A high-speed camera is used to capture images from a plane perpendicular to the incident laser sheet. Then, as shown in figure 3.1.2, the correlation between the group of particles in subsequent images is used to determine the displacement of each particle. Eventually, correlation on the whole image results in the full velocity field associated with the flow.

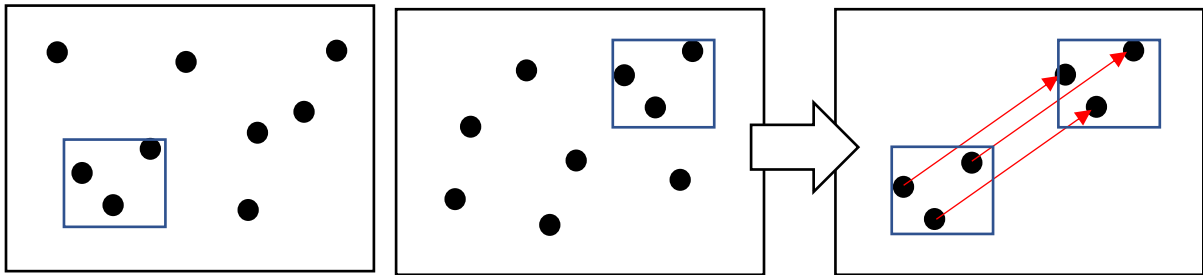


Figure 3.1.2: Displacement vector using correlation of two images in DPIV

3.1.3 Data

This study consists of two categories of data cases. The data for the first case represents the qualitative visualization of cavity vortex for different model. The objective of qualitative data is to visualize the change in cavity vortex as Re_d and cavity geometry is varied. The data from the second case is for the quantitative analysis of the skin friction drag associated with the models. The purpose of the quantitative data is to compare the skin friction drag reduction of various cavity models with respect to the flat plate model.

Data Acquisition

A typical data acquisition procedure consists of setting up the laser, camera and data acquisition software. The laser is switched on and the PRF and current values are set as shown in the table 3.1. The camera's exposure time is set such that the camera's FPS is synchronous with the PRF of the laser. This synchronization is necessary to obtain data with consistent image brightness.

Table 3.1: Operating parameters of the laser and the camera

Case	Laser		Camera			
	PRF (Hz)	Current(A)	Exposure Time (millisecond)	FPS	Lens	
					Focal length (mm)	Aperture size (f-no.)
1	100	19	10	100	50	2.2 (1.4-16)
2	100	19	10	100	25	2.2 (1.8-16)

The steady data acquisition time and total number of images acquired depends on the towing velocity of the plate. For this study, the maximum steady data acquisition time is 27 seconds, and the number of images acquired is 2700 for an experiment with towing velocity of 18.67 mm/s for a total towing distance of 675 mm. Similarly, the minimum steady data acquisition time is 9 seconds, and the number of images acquired is 900 for an experiment with towing velocity of 45.33 mm/s for a total towing distance of 675 mm.

Different camera lenses are used for the two different cases. For vortex visualization case, a lens of focal length 50 mm and f-number 1.4 lens is used to obtain magnified view of the cavity to better visualize the vortex. Whereas, for skin friction drag quantification, a lens of focal length 25 mm and f number 1.8 lens is used. A smaller focal length is used for this

case to obtain wider field of view for conclusive result from momentum deficit calculations.

A program is coded on LabVIEW such that the camera and the traverse operate simultaneously to acquire the data. The program controls the downward movement of the plate, and the corresponding acquisition of images is perpendicular to the laser sheet plane. Figure 3.1.3(a) and figure 3.1.3(b) show the image obtained from the experiments with case 1 and case 2 setup, respectively.

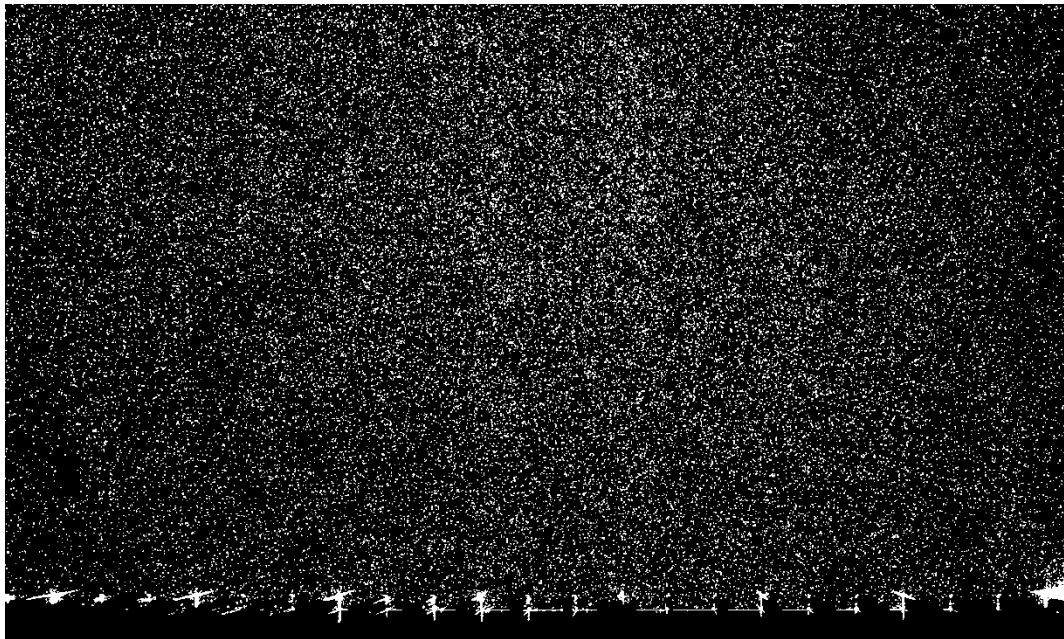


Figure 3.1.3(a): Image obtained from experiment with case 1 setup for 90° cavity model of AR 3

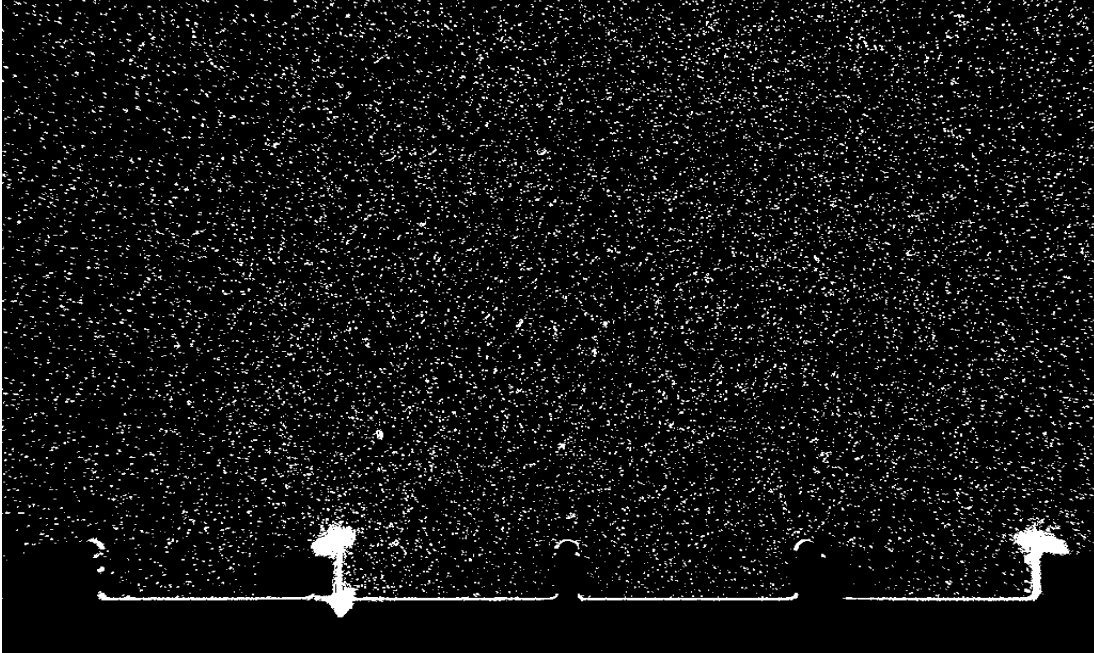


Figure 3.1.3(b): Image obtained from experiments with case 2 setup for 90° cavity model of AR 3

Data Processing and post-processing:

Insight 4G is the software used for processing the images acquired from data acquisition. Insight 4G utilizes the same core principle of DPIV processing, which includes finding a correlation between a group of particles between subsequent images and obtaining the velocity field based on displacement of those particles. The initial and final processing spot size are different for different cases and are shown in table 3.2.

Table 3.2: Processing window size

Case	Initial Window		Final Window	
	Spot A	Spot B	Spot A	Spot B
1	160 X 160	160 X 160	16 X 16	16 X 16
2 (Water)	40 X 20	40 X 20	10 X 10	10 X 10
2 (Oil)	48 X 48	48 X 48	24 X 24	24 X 24

The processing windows are different for each case because the images were acquired using lenses of different focal length which affects the pixel displacement of particles in subsequent images. As the average pixel size of a particle is 3 to 4 pixels, for better correlation, 8 to 10-pixel movement of particles between the consecutive images is recommended [53]. For case 2, experiments in water results in much smaller BL compared to experiments on the viscous oil. So, the window size is reduced to obtain a greater number of vectors inside the BL. The displacement vector obtained from processing the data is validated on the post processing section. In this section, the correlation peak of a group of particles is compared with the median of its neighboring particles. The processed result is validated if the difference of the peak and the median vector is within the specified tolerance. Further details on data processing and post processing for this study are on Appendix B.

Insight 4G has an output of good vector percentage which is a measure of accuracy of the validation of vectors obtained from the image processing to obtain the velocity field of the flow. In our study, the good vector percentage is consistently maintained around 95%. It also provides the standard deviation of velocity displacement that is used in the uncertainty calculation which is explained in Chapter 4. The result from Insight 4G is a text file which saves the vector field of the flow. The vector field is then further analyzed using MATLAB and Tecplot for desired results.

3.3 MODELS

3.3.1 Experimental plate models

Previous findings from collaborative work of Lang [2] concluded that butterfly's scales align to form a cavity of AR 2 of wall angle 45° as well as AR 3 with a cavity wall inclination

of 26° using the SEM image shown in figure 3.3.1(a). These differences are mainly because the images under consideration are from different regions on the wing and neither of these images provide a true perpendicular side view. However, recent investigations performed by biologists at the University of South Florida showed that the cavity on the forewings of a monarch butterfly were nearly AR 2.7 and wall angle around 15° . Figure 3.3.1 (b) shows the image of the butterfly wing used for determining the cavity geometry. The images from this investigation do not provide the true side view as well. So, the measurements of the butterfly cavities are not exact and therefore are approximated as AR 2 with 45° wall angle and AR 3 with 22° wall angle based on manufacturing limitations.



Figure 3.3.1 (a): Sagittal cut of butterfly wing SEM image

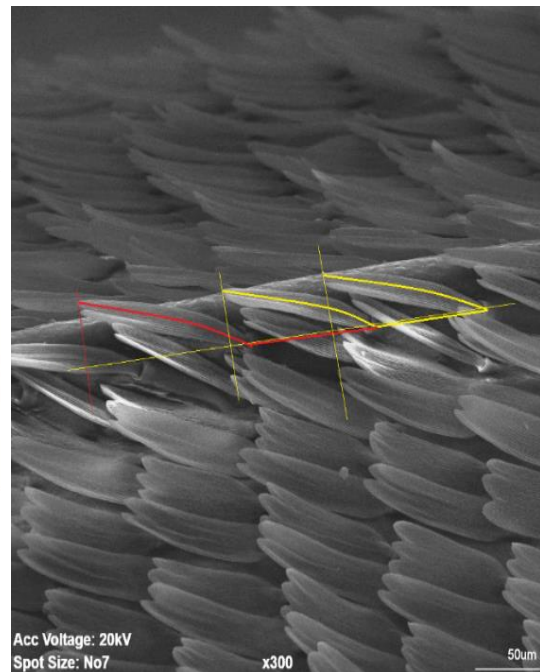


Figure 3.3.1 (b): Butterfly scales

For this study, the experiments are carried out on plate models as shown in table 3.3.

Table 3.3: Geometry and dimensions of cavity of the grooved plate models

Cavity Depth (mm)	Aspect Ratio (AR)	Wall angle	No. of cavities
3.5	2	90°	59
3.5	2	45°	60
3.5	2	22°	60
3.5	3	90°	41
3.5	3	45°	41
3.5	3	22°	41

The 90° cavity models are used for documenting the roller-bearing effect on a simple rectangular cavity for a boundary layer flow. Inclined cavities for the plate are modeled based on the SEM (Scanning Electron Microscope) findings of actual butterfly scales in the forewing. Since, the actual butterfly's cavity geometry were estimated values, different models with a varying range of AR and cavity wall inclination angles are tested.

3.3.2 Model design

The smooth flat plate model is 609.6 mm (24 inches) in length, 254 mm (10 inches) in width and 12.2 mm (0.5 in) thick and the dimension is chosen because of ease in manufacturing based on availability of 20 x 10 x 0.5 in³ blank pieces, which reduces the manufacturing cost as well. Also, larger models would lead to decrease in the effective towing distance of the model that ultimately would affect the resolution of the results. The cavity models are designed

with similar dimension for consistency. The cavity models are printed on a Lulzbot 3D-printer using PLA and ABS as the primary material for printing.

The LE is designed based on the study conducted by Davis [7] to ensure our testing models does not encounter boundary layer flow separation. The LE is an elliptical profile with the ratio of major to minor axis equal to 4. The thickness of the LE is 12.2 mm for all the

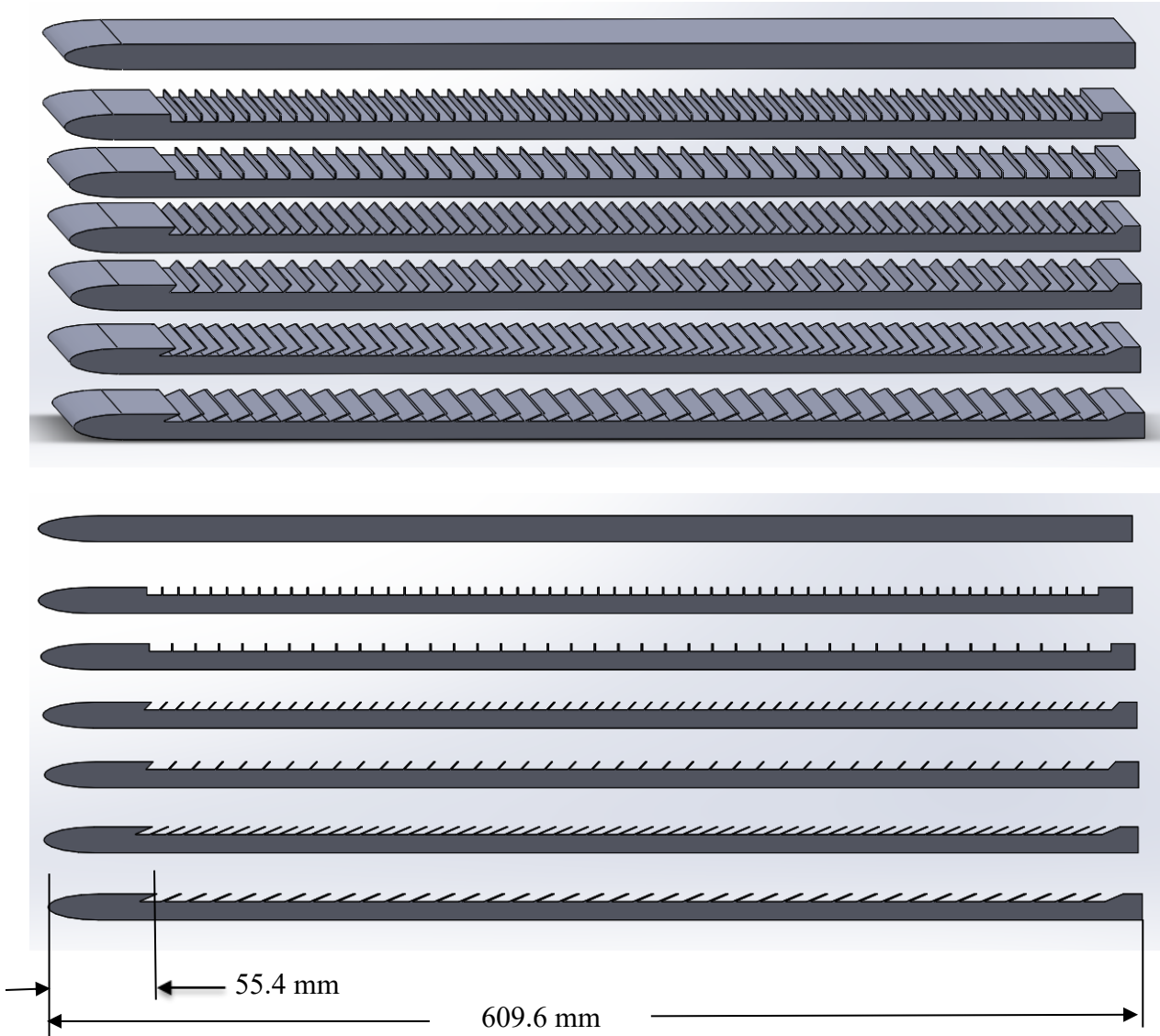


Figure 3.3.2: Smooth and cavity models diagram obtained from Solidworks. Models from top to bottom; flat plate, 90° AR 2, 90° AR 3, 45° AR 2, 45° AR 3, 22° AR 2 and 22° AR 3.

models used for our study. The details on design of LE is discussed on Appendix C. Figure 3.3.2 shows the Solidworks diagram of the models that are used for experiments in this study.

3.4 VALIDATION OF EXPERIMENTAL SETUP

To ensure that the results obtained from this study are conclusive and are not influenced by a faulty setup, a validation test of the experimental set up was performed. The following section consists of results associated with laminar boundary layer flow over a smooth flat plate. Operating parameters from case 2 in table 3.1 and 3.2 are used for the validation experiment.

3.4.1 Comparison of Velocity profiles

Figure 3.4.1.1(a) shows the comparison of velocity profile at Re_d 3.5 from the experiment performed with oil as the fluid medium. The upstream and downstream profile are

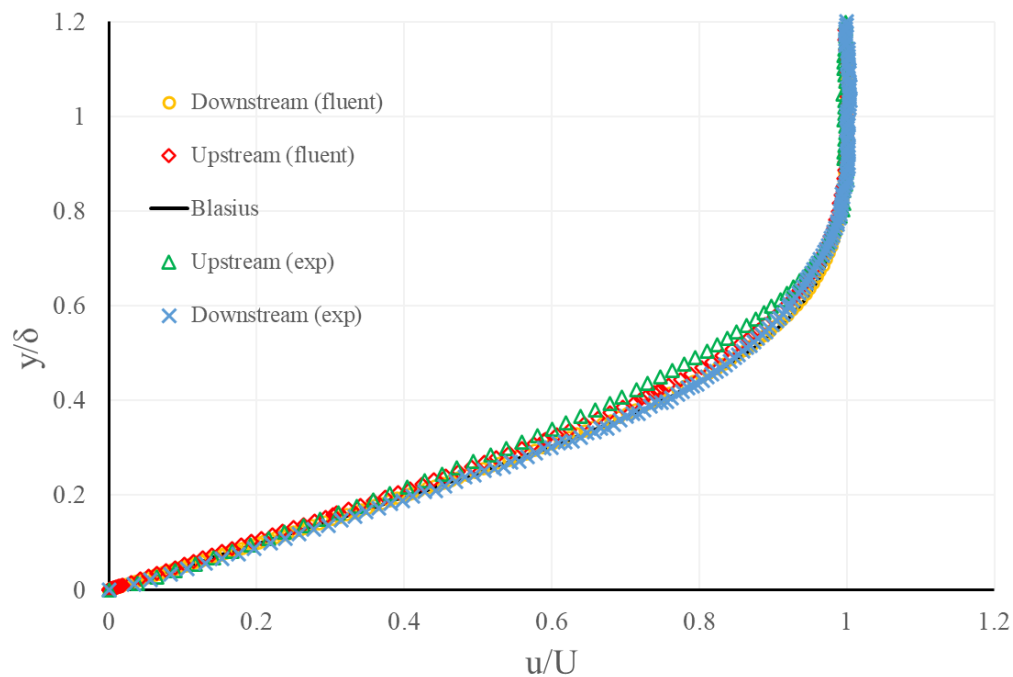


Figure 3.4.1.1(a): Velocity profile comparison of experimental, computational, and theoretical laminar boundary layer flow at Re_d 3.5

at 55.4 mm and 290 mm from the LE. The upstream distance is picked close to the LE because shear stress distribution is higher near the LE and decreases towards the downstream as the BL grows bigger. So, the cavity embedded models will experience stronger potential roller-bearing effect for cavities near the LE. The downstream location is the furthest distance from the LE in the data acquisition window. For the skin friction drag calculation on the cavity and smooth plate models, these upstream and downstream locations are the inlet and outlet of the control surface. The significance of these two upstream and downstream locations are mentioned in detail in Chapter 4. The upstream velocity profile obtained from the experimental data shows slight difference in comparison to the Blasius solution. The reason for this is because Blasius assumes that the plate is infinitely thin such that there is no effect of the LE thickness to the oncoming flow. However, the experimental models consist of a LE with curved elliptical profile and thickness of 12.7 mm. This causes the flow to accelerate as it passes around the curved portion of LE on towards the flat section of the plate. A computational simulation of the experimental setup carried out using Ansys Fluent (Appendix D) also shows the accelerated region as measured in the experiment.

Figure 3.4.1.1(b) and figure 3.4.1.1(c) show a contour plot of the u-velocity component obtained from the computational results and the experimental data for Re_d 3.5. The blue and green vertical line show the upstream and downstream positions, respectively, where the velocity profiles are compared. The upstream position is 55.4 mm and downstream position is 290 mm from the LE. The experiment is limited to the white box (330 mm x 170 mm) drawn in the contour plot from Fluent. The velocity profile from upstream and downstream location shows different trends for experimental results and does not collapse on top of each other as in Blasius solution. The presence of higher velocity region above the BL that creates a slight

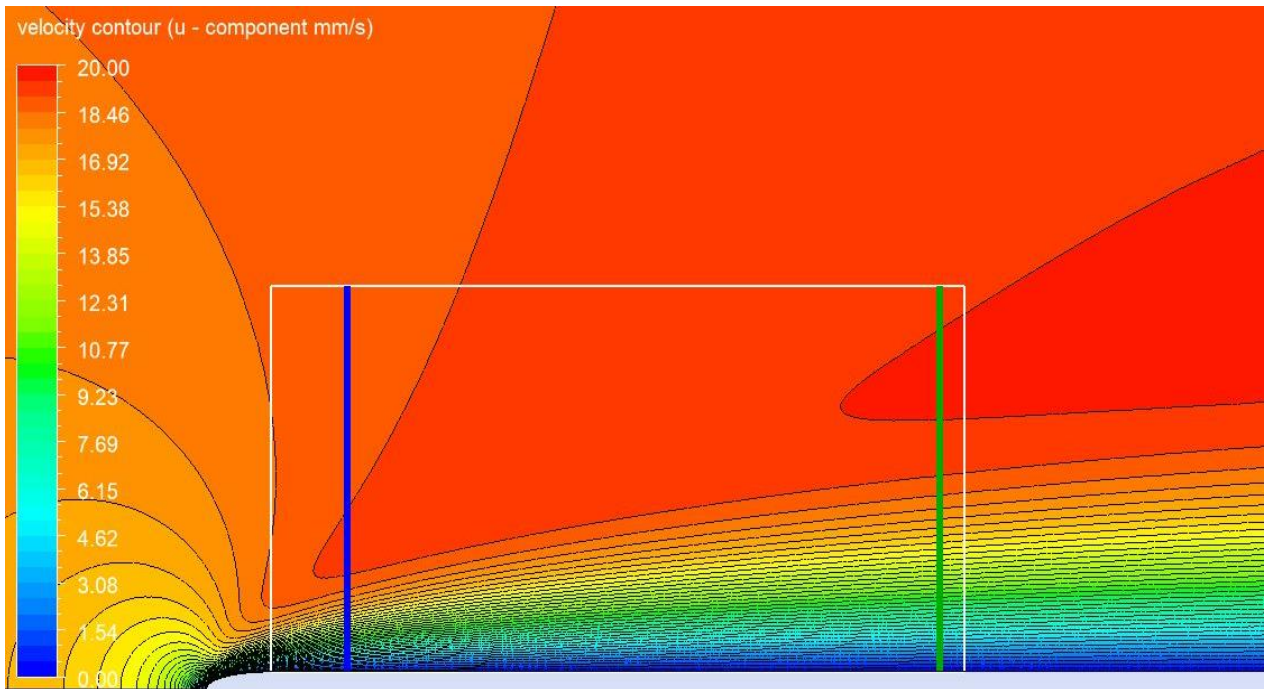


Figure 3.4.1.1(b): Velocity contour of u-component of velocity from computational result for $Re_d 3.5$

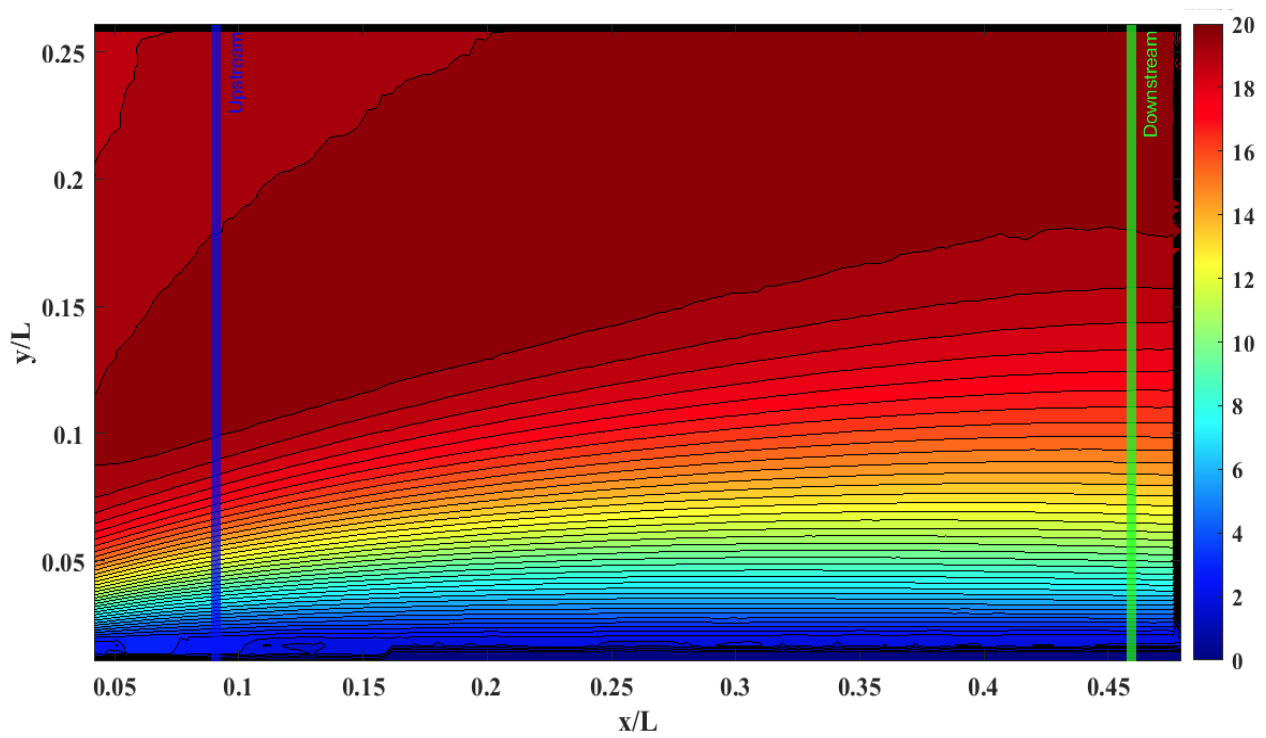


Figure 3.4.1.1(c): Velocity contour of u-component of velocity from experimental data for $Re_d 3.5$

for upstream and downstream location. The difference in velocity profiles at the upstream and downstream location should not affect the result of this study because the surface drag obtained from the cavity embedded models are compared to those from the flat plate, and both models has the same LE profile.

Figure 3.4.1.2(a) shows the velocity profile comparison when the experiments are performed using water as the fluid medium for $Re_d 70$. Like $Re_d 3.5$, the velocity profile from experimental and fluent shows overshoot above the freestream velocity in the inviscid region above the viscous BL.

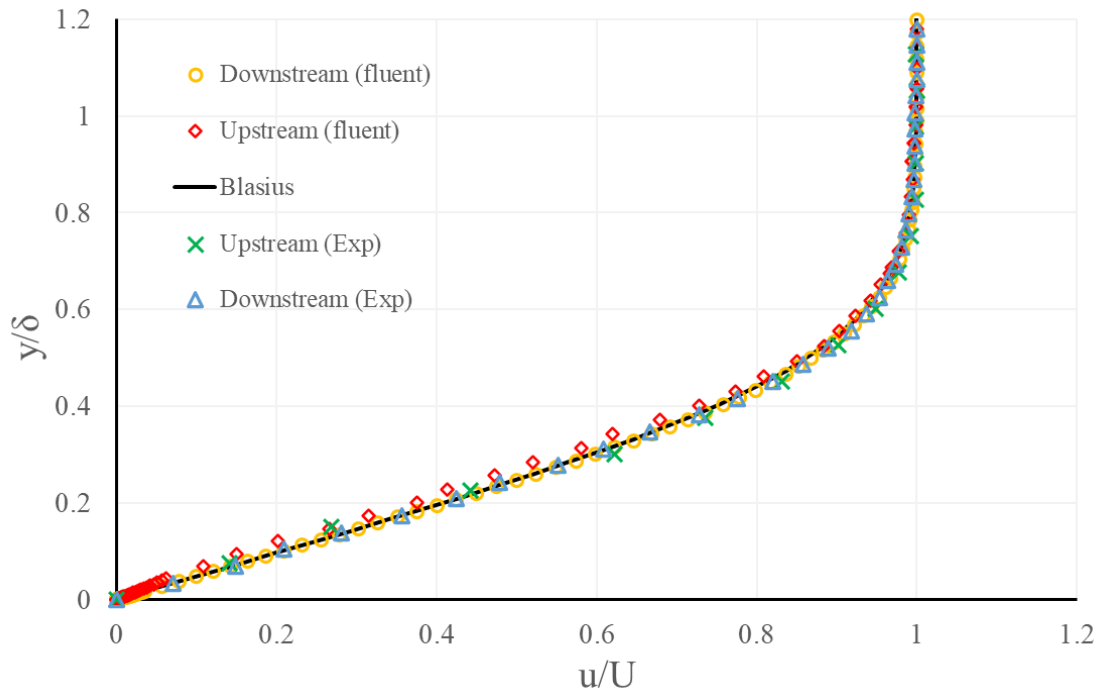


Figure 3.4.1.2(a): Velocity profile comparison of experimental, computational, and theoretical laminar boundary layer flow at $Re_d 70$

Figure 3.4.1.2(b) and figure 3.4.1.2(c) show the velocity contour for $Re_d 70$ obtained from the computational and the experimental result. The contour with velocity higher than the freestream reduces in size when compared to $Re_d 3.5$. As the Re_d increases, the inertial effect becomes more dominant than the viscous effect.

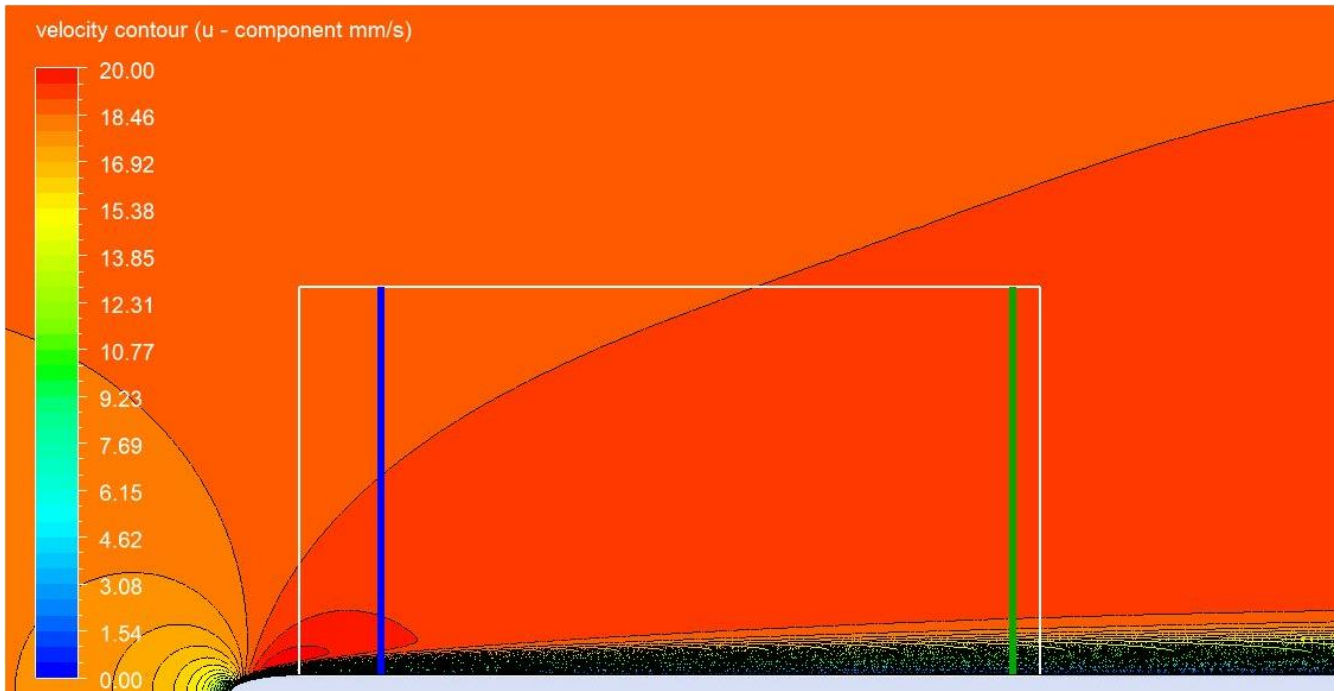


Fig. 3.4.1.2(b): Velocity contour of u -component of velocity from computational result for $Re_d 70$

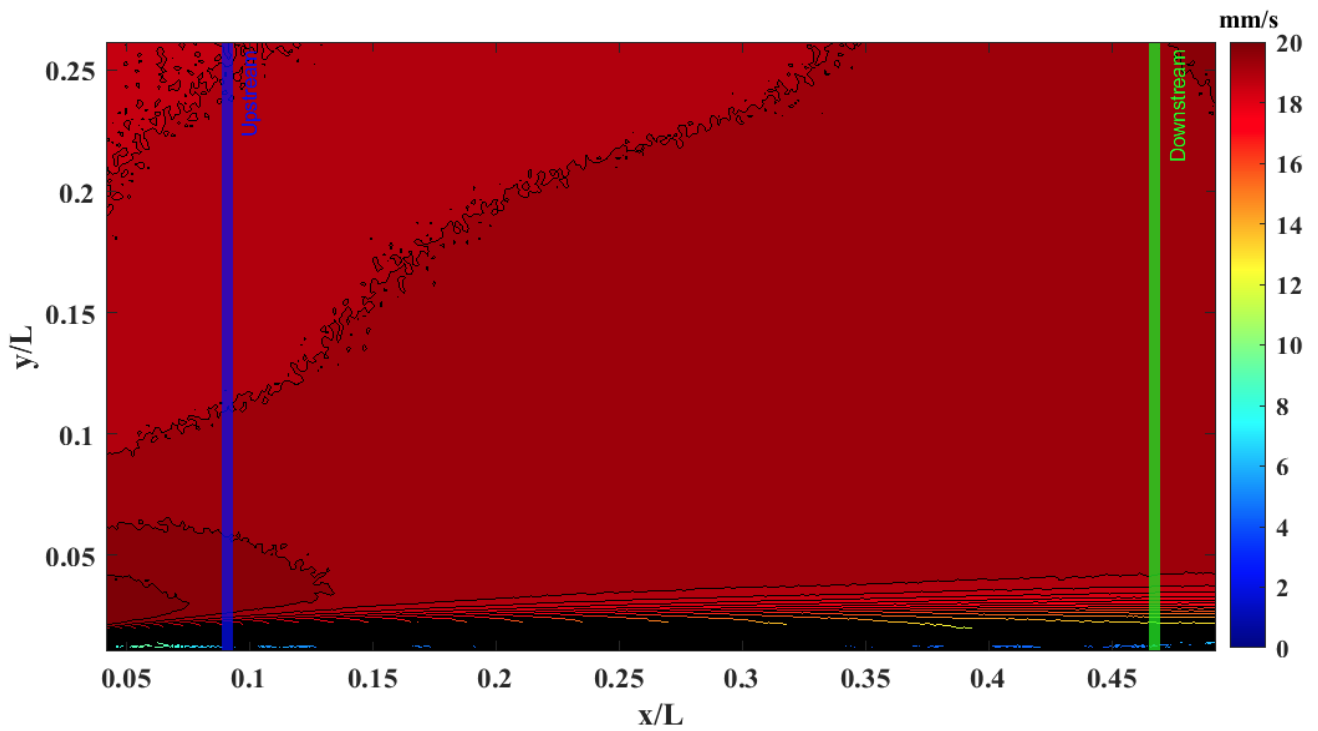


Figure 3.4.1.2(c): Velocity contour of u -component of velocity from experimental result for $Re_d 70$

The BL thickness for Blasius solution was calculated from equation 3.1 [54, 55].

$$\delta = \frac{5 * x}{\sqrt{Re_x}} \quad (3.1)$$

BL thickness for experimental and Fluent data was obtained by approximating the vertical distance (y-values) from the plate where the shear stress approximates to zero value.

The displacement thickness for Blasius solution was calculated from equation 3.2 shown below.

$$\delta^* = \frac{1.727 * x}{\sqrt{Re_x}} \quad (3.2)$$

For the Fluent and the experimental data, the displacement thickness was calculated by integrating equation 3.3 from the limit 0 to height of the BL thickness (δ) obtained from previous calculation.

$$\delta^* = \int_0^{\delta} \left(1 - \frac{u}{U_0}\right) dy \quad (3.3)$$

Similarly, the momentum thickness for the Blasius solution was calculated from equation 3.4 shown below.

$$\theta = \frac{0.664 * x}{\sqrt{Re_x}} \quad (3.4)$$

For the Fluent and the experimental data, the displacement thickness was calculated by integrating equation 3.5 from the limit 0 to δ .

$$\delta^* = \int_0^{\delta} \frac{u}{U_0} \left(1 - \frac{u}{U_0}\right) dy \quad (3.5)$$

Table 3.4 shows the list of characteristic BL parameters (momentum thickness, displacement thickness and boundary layer thickness) obtained from experimental data, computation, and Blasius solution at upstream position $x = 55.4$ mm from the LE.

Table 3.4: Characteristic upstream boundary layer properties of a flat plate flow calculated for the theoretical Blasius solution, using Fluent and measured experimentally

Re_d	θ (mm)			δ^* (mm)			δ (mm)		
	Blasius	Fluent	Exp	Blasius	Fluent	Exp	Blasius	Fluent	Exp
3.5	5.12	5.53	6.59	13.25	14.60	17.16	38.52	43.00	50.40
70	11.70	13.37	13.77	30.44	35.79	36.31	88.13	88.13	105.59

Table 3.5 shows the BL parameters for downstream position $x = 290$ mm from the LE.

Table 3.5: Characteristic downstream boundary layer properties of a flat plate flow

Re_d	θ (mm)			δ^* (mm)			δ (mm)		
	Blasius	Fluent	Exp	Blasius	Fluent	Exp	Blasius	Fluent	Exp
3.5	1.14	1.18	1.26	2.97	3.12	3.37	8.61	10.16	10.57
70	2.62	3.07	3.27	6.81	8.40	8.87	19.70	25.72	26.03

CHAPTER 4

RESULTS AND DISCUSSION

The primary result for this study is the direct comparison of the surface drag of a smooth flat plate and the surface drag of a cavity embedded model measured using the velocity data over the plates using DPIV. As the cavity geometry is altered, it is expected that the drag for each test model will be different. The size and shape of the cavity vortex will also vary based on cavity geometry and Re_d . To understand the differences in surface drag between various experimental models, it is necessary to understand the nature of the vortices formed in various cavity geometries under different Re_d . Section 4.1 focuses on the visualization of the cavity vortex (or vortices) for different models at various Re_d and the surface drag reduction results in section 4.2.

4.1 FLOW VISUALISATION OF CAVITY VORTEX

This section consists of results obtained from data acquired in case 1 as stated in Table 3.1 which is using a higher focal length lens to zoom in the cavity for qualitative analysis. The pathlines of the particles forming the vortex are visualized by the superposition of all the instantaneous images on top of each other. Flow direction is from left to right on all the flow visualization images of this section. The MATLAB code used to generate these images can be found in Appendix E1.

4.1.1 Rectangular cavity (90° cavity wall inclination) with AR 2

Figure 4.1.1 (a), (b), (c) and (d) shows the vortex formed in a rectangular cavity of AR 2 at Re_d 3.5, 8.5, 70 and 170 respectively. Each of these cases shows a dominant vortex formed

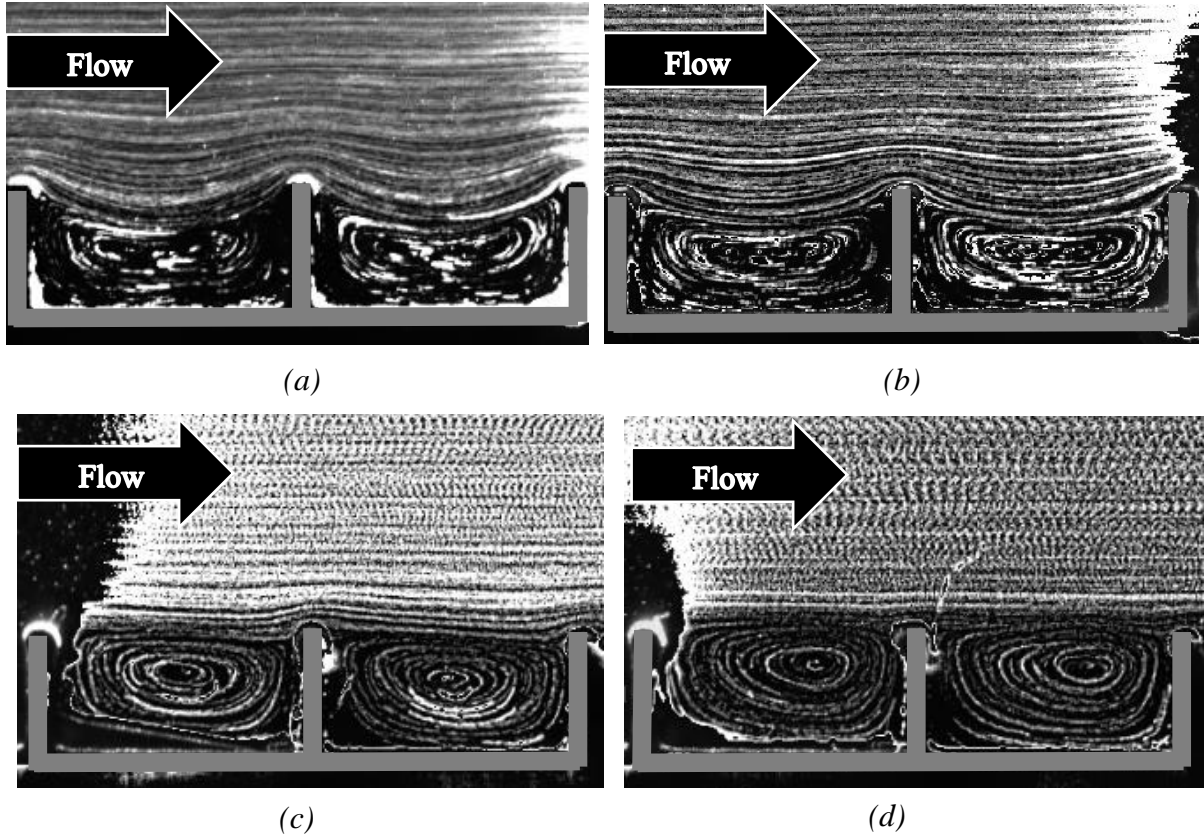


Figure 4.1.1: Cavity vortex visualization for models with rectangular cavity of AR 2 for (a) Re_d 3.5, (b) Re_d 8.5, (c) Re_d 70 and (d) Re_d 170

inside the cavity with the dividing streamline above it. The dividing streamline has an upward concave profile for the lower Re_d which suggests that roller-bearing effect is present and there is a potential decrease in the surface drag. As the flow Re_d passes 70, the dividing streamline has less curvature than that in lower Re_d . This is where the shear layer forming on the dividing streamline breaks and the flow from the outer BL mixes with the cavity. It is hypothesized that

the mixing of fluid between these two regions will result in an increase in net surface drag. The vortex visualization results match the flow visualization of Taneda [14] and computational results of Shen [4] as previously shown in figure 2.1.3 (c) and figure 2.1.5 (c).

4.1.2 Rectangular cavity (90° cavity wall inclination) with AR 3

Figure 4.1.2 (a), (b), (c) and (d) shows the vortex formed in a rectangular cavity of AR 3 at Re_d 3.5, 8.5, 70 and 170 respectively. Unlike the rectangular cavity of AR 2, the AR 3

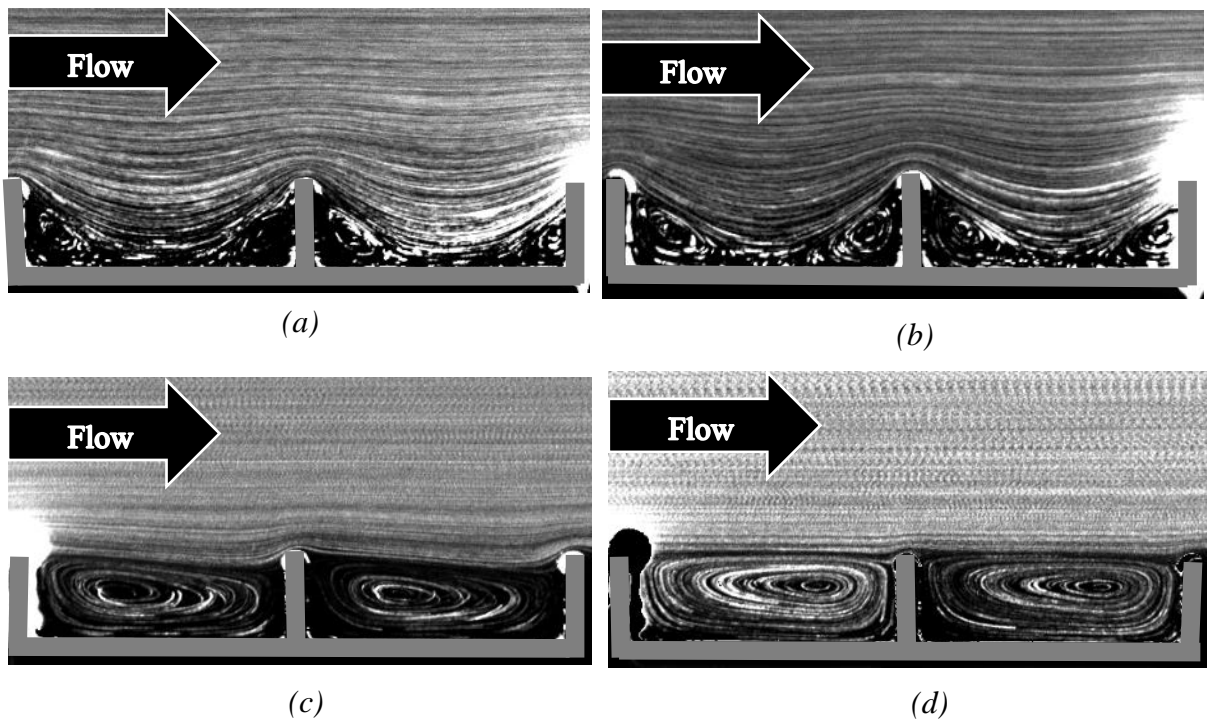


Figure 4.1.2: Cavity vortex visualization for models with rectangular cavity of AR 3 for (a) Re_d 3.5, (b) Re_d 8.5, (c) Re_d 70 and (d) Re_d 170

cavities do not always show a single dominant cavity vortex. For Re_d 3.5 and 8.5, there are two corner vortices and an upward concave profile of dividing streamline forming above both vortices, but not quite impacting the cavity floor. Flow visualization of Taneda [14] and computational results of Shen [4] as shown in figure 2.1.3 (d) and figure 2.1.5 (d) also show similar qualitative results. For Re_d 70, the two distinct corner vortices are replaced by a single

vortex with the center shifted towards the upstream edge, and the dividing streamline dips towards the downstream end of the cavity. For the Re_d 170, the vortex is again asymmetric as the center of vortex shifts more towards the downstream end of the cavity. This was also mentioned in Zhang's study for Re 1.1×10^5 as shown in figure 2.1.4.

4.1.3 45° cavity wall inclination with AR 2

Likewise, figure 4.1.3 (a), (b), (c) and (d) shows the vortex formed in a cavity of wall inclination 45° and AR 2 at Re_d 3.5, 8.5, 70 and 170 respectively. The results are similar to

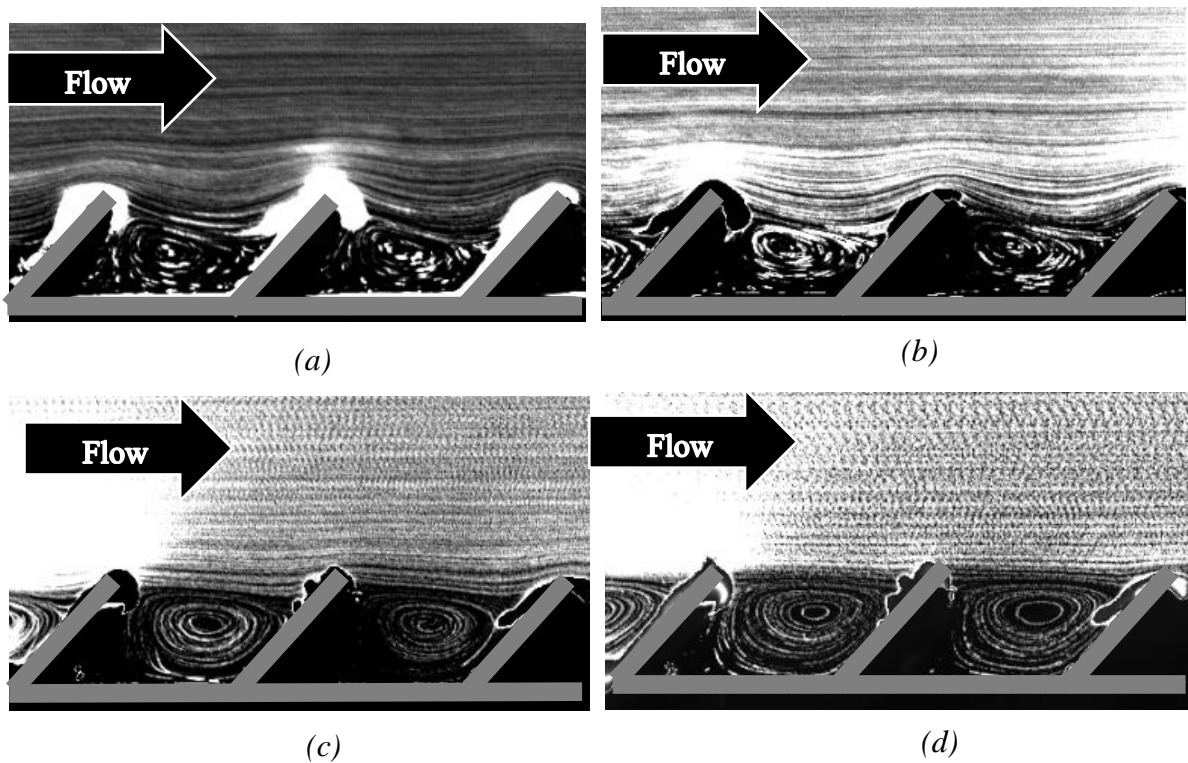


Figure 4.1.3: Cavity vortex visualization for models with cavity wall inclination of 45° and AR 3 for (a) Re_d 3.5, (b) Re_d 8.5, (c) Re_d 70 and (d) Re_d 170

those obtained for rectangular cavities of AR 2 as in figure 4.1.1. The notable differences are the reduced size of the dominant vortex for all the Re_d and the asymmetric upward concave profile of the dividing streamline. The flow visualization results obtained here are similar to

the computational streamline contours shown in figure 2.1.6 (a) and (b) [5]. Note that the secondary corner vortices for all the models with angled cavity wall inclination (45° and 22°) were not visible. This is mainly because the flow visualization images are obtained from the superposition of instantaneous images from the DPIV and the movement in these small vortices is very slow. Also, for the experimental DPIV setup the laser sheet is incident perpendicular to the plate such that the inclined cavity wall always casts a shadow on the cavity, hence partially blocking the upstream portion of the cavity.

4.1.4 45° cavity wall inclination with AR 3

Figure 4.1.4 (a), (b), (c) and (d) shows the vortex formed in a cavity of wall inclination 45° and AR 3 at Re_d 3.5, 8.5, 70 and 170 respectively. For Re_d 3.5 and 8.5, a single vortex is

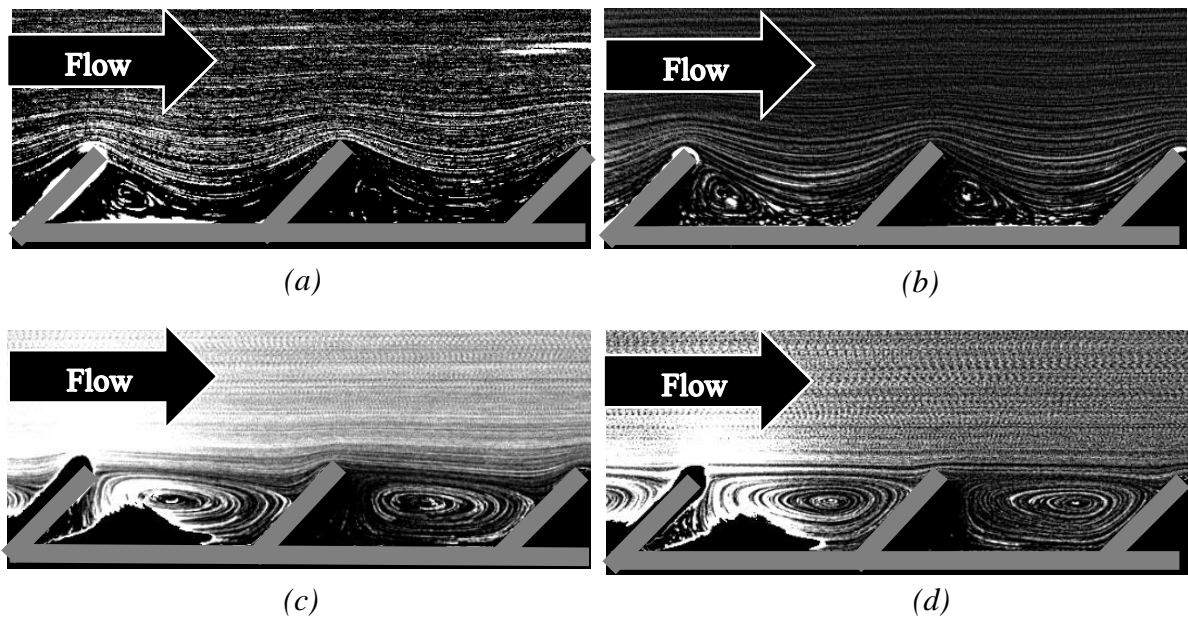


Figure 4.1.4: Cavity vortex visualization for models with cavity wall inclination of 45° and AR 3 for (a) Re_d 3.5, (b) Re_d 8.5, (c) Re_d 70 and (d) Re_d 170

formed on the upstream corner region of the cavity and the dividing streamline dips after it passes the cavity. As the Re_d is increased to 70, a single contorted vortex covers the entire

cavity. Again, the shift of the center of the vortex from the upstream to the downstream side is observed from Re_d 70 to 170.

4.1.5 22° cavity wall inclination with AR 2

Figure 4.1.5 (a), (b), (c) and (d) shows the vortex formed in a cavity of wall inclination 22° and AR 2 at Re_d 3.5, 8.5, 70 and 170 respectively. As mentioned in section 4.1.3, it is difficult to visualize the vortex inside the cavity because the angled wall of the cavity blocks the laser sheet giving a limited view of the vortex forming at Re_d 3.5 and 8.5. As the Re_d increases, the dividing streamline changes to a more linear profile such that the vortex resides on the upper portion of the cavity as shown for Re_d 70 and 170. Among all the models studied, the cavity vortex is the smallest for 22° wall inclination and AR 2.

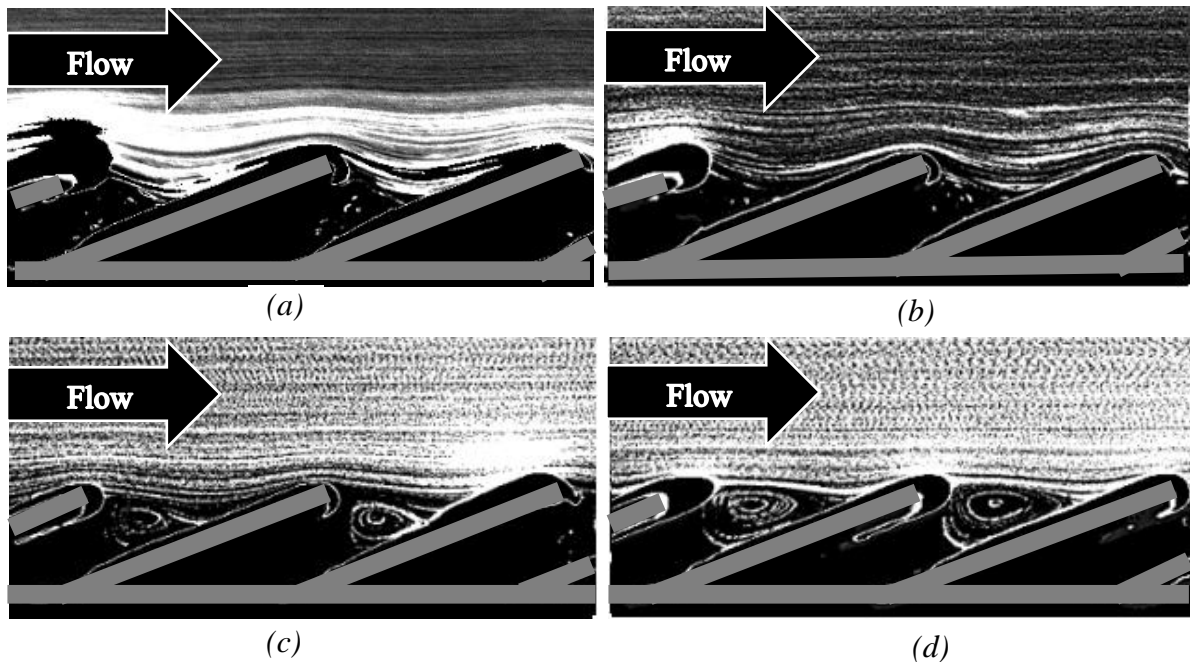


Figure 4.1.5: Cavity vortex visualization for models with cavity wall inclination of 22° and AR 2 for (a) Re_d 3.5, (b) Re_d 8.5, (c) Re_d 70 and (d) Re_d 170

4.1.6 22° cavity wall inclination with AR 3

The vortex visualization for 22° cavity wall and AR 3 as shown in figure 4.1.6 resembles the results of 45° cavity wall and AR 3 from section 4.1.4. For Re_d 3.5 and 8.5, the vortex shifts towards the upstream corner of the cavity and the dividing streamline dips around the downstream corner of the cavity. As the flow Re_d is increased, the dividing streamline straightens, and the vortex fills out most of the cavity. The flow visualization results obtained here match well with the computational streamline contours shown in figure 2.1.6 (c) and (d) [5].

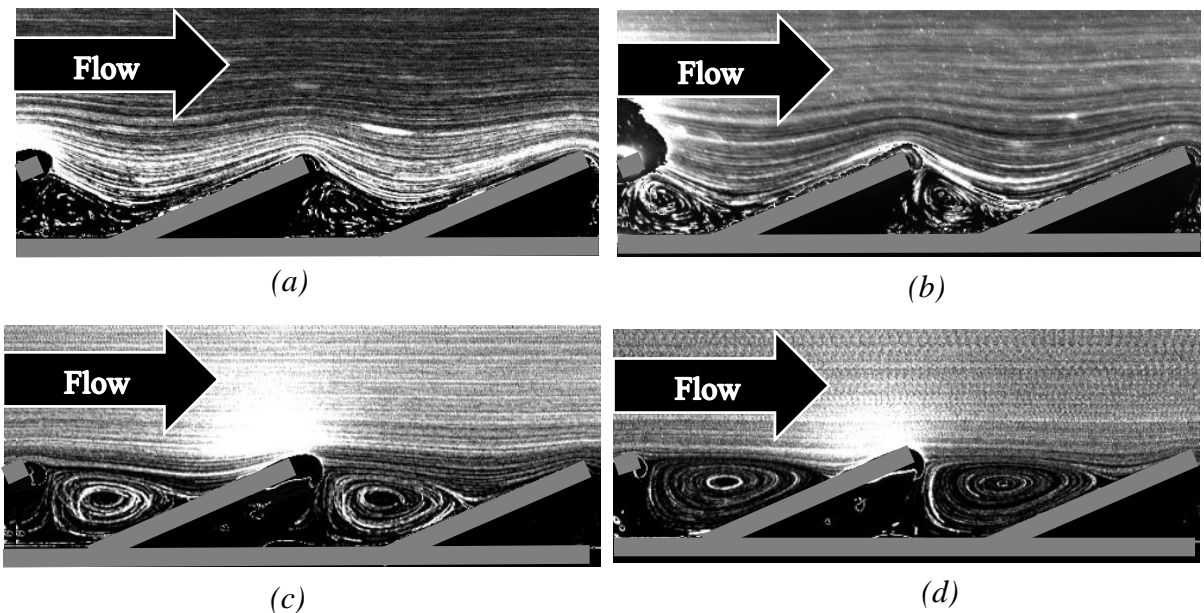


Figure 4.1.6: Cavity vortex visualization for models with cavity wall inclination of 22° and AR 3 for (a) Re_d 3.5, (b) Re_d 8.5, (c) Re_d 70 and (d) Re_d 170

If the AR is kept constant and the cavity wall inclination is decreased, the size of the single dominant vortex also decreases. Although the secondary corner vortices could not be visualized in this study, with the decrease in wall inclination angle, the size of the secondary vortex formed in the upstream corner of the cavity should increase. The variation in the size of

the largest and most dominant vortex may contribute to the variation of potential surface drag reduction.

4.2 SURFACE DRAG

As hypothesized in chapter 1, the presence of a single cavity vortex can exhibit a roller-bearing effect on the outer BL flow and reduce the net surface drag. This section consists of the results obtained from data acquired for case 2 of table 3.1.

4.2.1 Theory

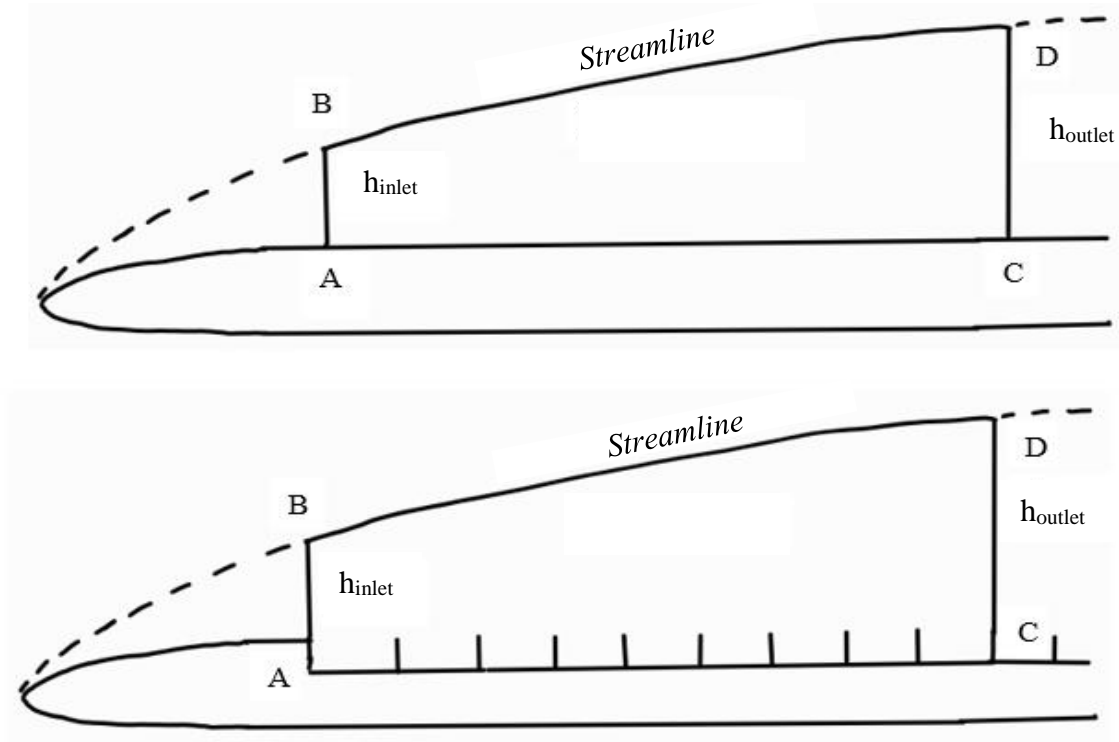


Figure 4.2.1: Control surface ABDCA for calculating surface drag along the length AC

The surface drag is calculated based on a control volume analysis and calculating the difference in rate of momentum of the flow between the inlet and outlet regions. Figure 4.2.1

shows the diagram of the control surface used to calculate the 2-D surface drag for a flat plate and a cavity embedded model. AB and CD are the height of the inlet and outlet of the control surface. For cavity embedded models, the height of the outlet is measured from the tip of the cavity wall to the BL height. The top of the control surface is the streamline that includes point B and D.

Equation 4.1[56] shows the result of the conservation of momentum analysis with the sum of forces in the x-direction relevant to formulating the surface drag analysis for this study.

$$\sum F_x = F_p - D = \left(\int_0^{h_{outlet}} \rho u_o^2 dy - \int_0^{h_{inlet}} \rho u_i^2 dy \right) \quad (4.1)$$

Where, u_i and u_o are the local u-component of the velocity at the inlet and outlet, respectively. F_p is the net pressure force acting on the control surface, and D is the surface drag of the flat plate/model. Appendix E shows the calculation of the net pressure force acting on the control surface. The pressure force acting on the control surface is found to be negligible. Thus, the surface drag per unit width and the corresponding drag coefficient per unit width is then calculated from equation 4.2 and 4.3, respectively.

$$-D = \left(\int_0^{h_{outlet}} \rho u_o^2 dy - \int_0^{h_{inlet}} \rho u_i^2 dy \right) \quad (4.2)$$

$$c_d = \frac{2D}{\rho U_\infty^2 l} \quad (4.3)$$

Where, U_∞ is the freestream velocity of the flow and l is the distance between the upstream and downstream position in the plate. The surface drag coefficient percentage change is then calculated from equation 4.4, which gives a direct comparison to the flat plate and shows when models are resulting in drag reduction.

$$\Delta C_d \% = \frac{C_{d_{model}} - C_{d_{flat\ plate}}}{C_{d_{flat\ plate}}} \quad (4.4)$$

4.2.2 Results of surface drag

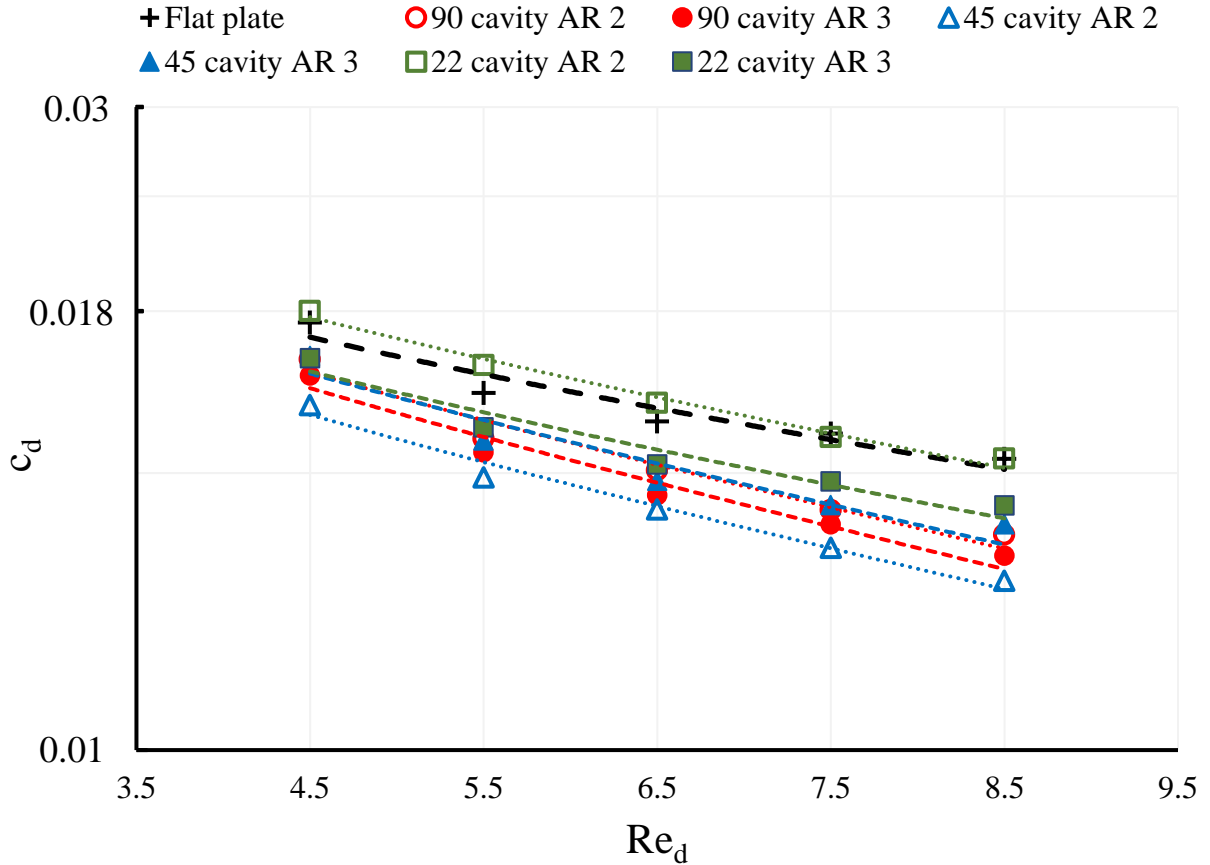


Figure 4.2.2(a): Drag coefficient per unit width vs lower Re_d

Figure 4.2.2(a) shows the change in surface drag coefficient per unit width as the Re_d is increased for the various models, plotting the data in log scale makes it easier to visualize. The experiments used oil as the flow medium for data acquisition for low Re_d range. All the models, except the 22° cavity wall AR 2 case, show a drag reduction in comparison to the flat plate. Figure 4.2.2(b) shows the same result in terms of percentage of surface drag coefficient change. The drag reduction for various models can be attributed to the ‘roller-bearing effect’.

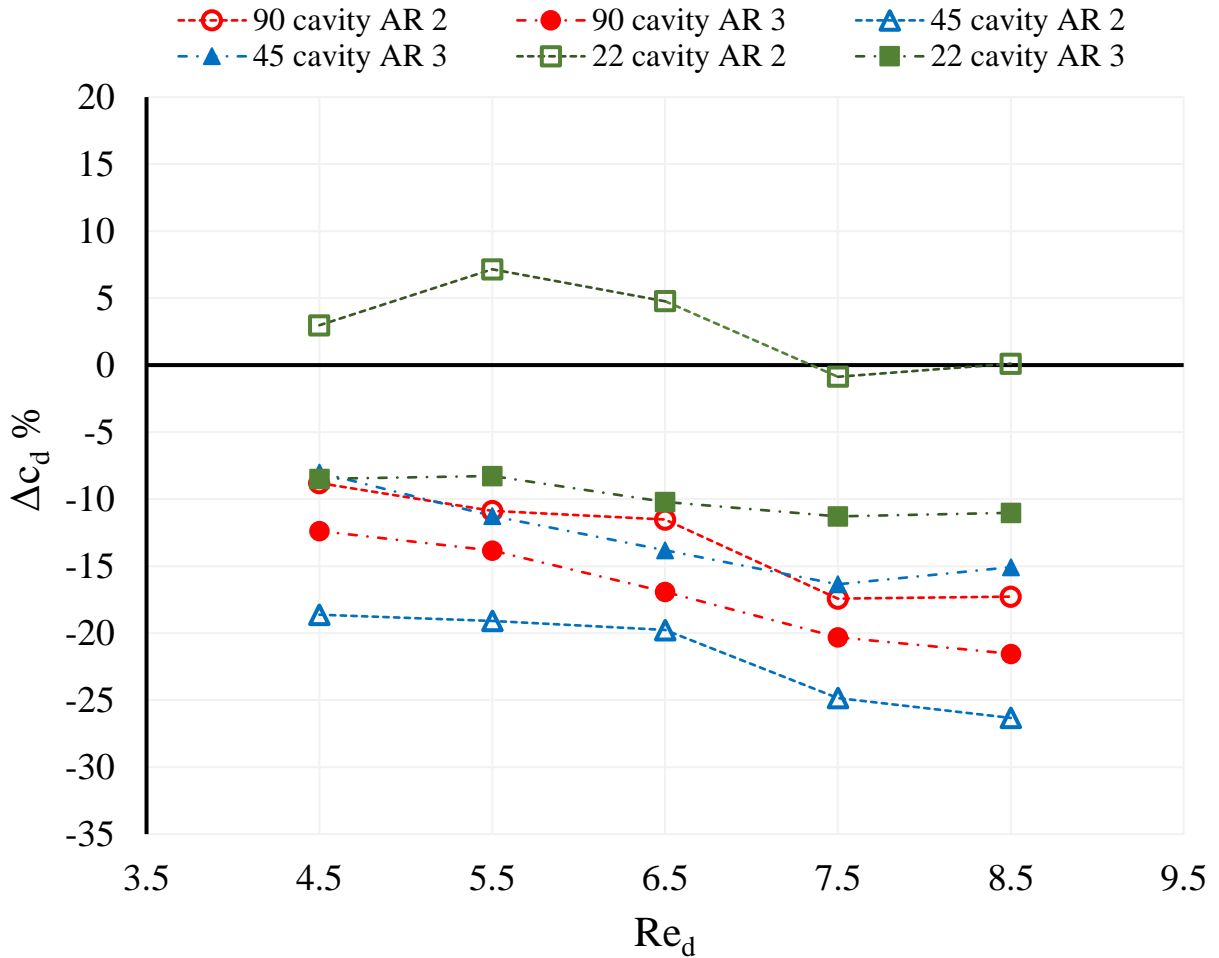


Figure 4.2.2(b): Percentage change in surface drag coefficient for various low Re_d

Each of the models form a cavity vortex that is trapped beneath the dividing streamline such that the BL experiences a reduced surface friction compared to the skin friction offered by the surface of a smooth flat plate. As long as there is no exchange between the cavity flow and the outer BL flow, the vortex acts as a roller-bearing to the flow above it. Most interestingly, the drag reduction is highest for the 45° cavity with AR 2 and lowest for the 22° cavity with AR 3 indicating there is an optimal shape for the cavity geometry that at low Re (which is the flow regime of the butterfly) to achieve surface drag reduction.

The model with 22° cavity with AR 2 does not seem to offer any drag reduction. The flow visualization of the cavity vortex for this model showed the smallest vortex of all the cases and the dividing streamline appears to be more in contact with the cavity walls as shown in figure 4.1.5(a) & (b). Even though figure 4.1.2 (a) and (b) does not show a single dominant vortex formed inside the cavity, the 90° cavity with AR 3 model shows a significant drag reduction of around 15 to 20%. It could be mainly because the dividing streamline does not dip down enough to touch the bottom of the cavity. The reasoning for drag reduction due to roller-bearing effect is still valid if the dividing streamline forms above the cavity floor still resulting in a partial slip condition for the outer flow passing over the cavity. Table 4.2 shows the comparison of surface drag reduction obtained in this BL experimental study for 45° cavity AR 2 and 22° cavity AR 3 with the results shown in figure 2.3.4 [2].

Table 4.2: Percentage of drag reduction of various models at various Re_d

Models	Source	Δc_d % reported	Difference from BL Exp
	Couette Exp	-35	13
45 cavity AR 2	Couette Comp	-14	-8
	BL Exp	-22	
26 cavity AR 3	Couette Exp	-45	35
	Couette Comp	-17	7
22 cavity AR 3	BL Exp	-10	

The 45° cavity AR 2 drag reduction values for this study is 8% higher than the results from the computational study in Couette conditions [5]. The 22° cavity AR 3 results in less drag reduction for this study in comparison to the results from the 45° cavity AR 2. However, for Couette flow study the 45° cavity AR 2 has less drag reduction than the 26° cavity AR 3 model. It could be because the 22° cavity AR 3 shows more dip in the dividing streamline. This would increase the gap height between the upper plate and the lower surface, and in Couette flow, the velocity gradient decreases as the gap height increases. This would lead to decrease in the shear stress as the velocity gradient decreases which in turn decreases the surface drag. However, there is no such issues in the normal boundary layer flow because the BL grows and adjust naturally to the geometry.

The difference in drag reduction for this study of normal BL flow over the 22° cavity AR 3 and the drag reduction than the 26° cavity AR 3 model in Couette condition is 7% less. Likewise, the drag reduction decreases as the Re_d increases to the critical Re_d for Couette flow. The reason for it could be the decreasing gap height for increasing Re_d as the curve of the dividing streamline reduces. On contrary, the results from BL flow shows that the drag reduction increases as the Re_d increases from 4.5 to 8.5. Since, the gap height issue from Couette flow is not relevant to the BL flow, the increase in Re_d increases the vortex size and with that the partial slip velocity on the interface of the vortex and outer BL should also increase, leading to reduced surface drag.

When the Re_d is increased beyond a critical value, the dividing streamline collapses and the low momentum fluid inside the cavity and high momentum fluid from the outer BL mixes. This causes an increase in net surface drag. Figure 4.2.3(a) shows the change in surface drag coefficient per unit width for various models as the Re_d is increased. Unlike the lower Re_d

results, the trendline of drag coefficient for the models crosses over the trendline of the flat plate. So, there exists a critical region from Re_d 90 to Re_d 120 beyond which there is a net surface drag increase.

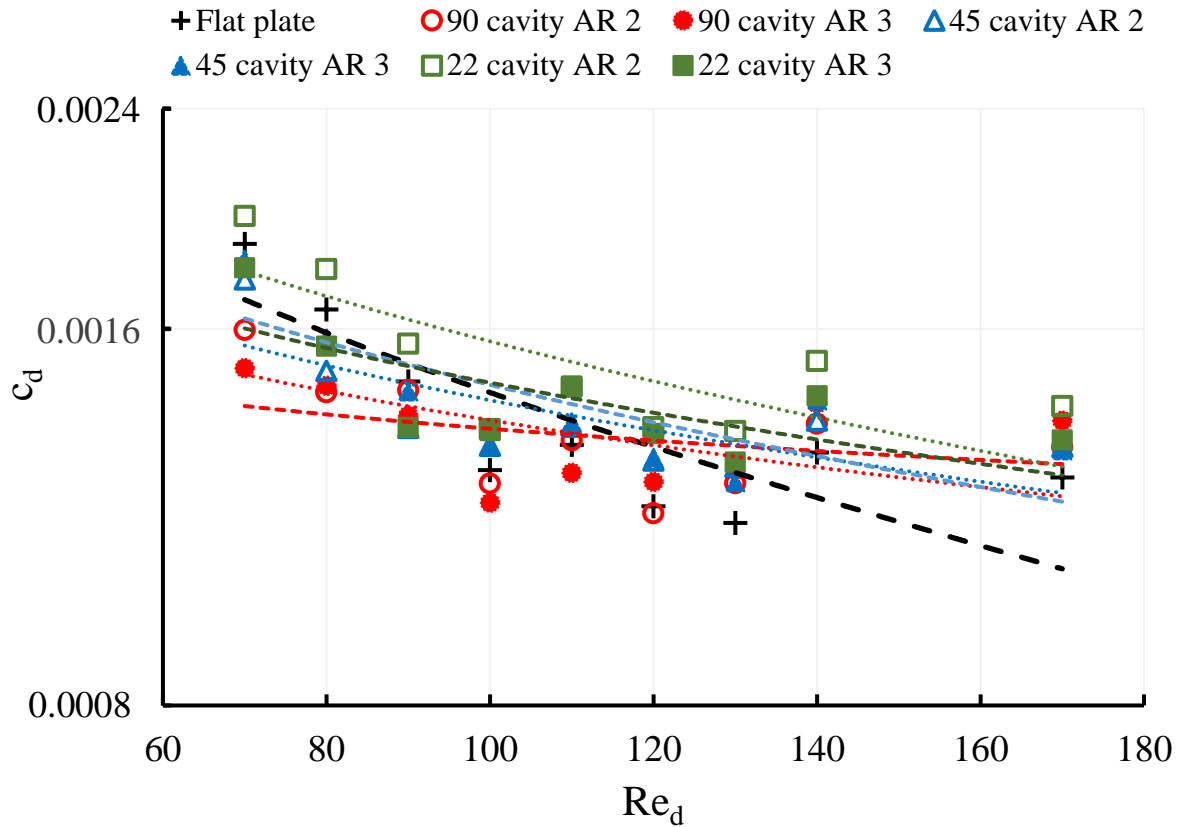


Figure 4.2.3(a): Drag coefficient per unit width vs higher Re_d

Figure 4.2.4(b) shows the results in terms of percentage change in surface drag coefficient with respect to the flat plate. At the higher Re_d range of 130 to 170, there is a net increase of surface drag from around 5 to 15%. As the Re_d increases beyond 170 we expect even higher increase in drag due to increased vigorous mixing of the flow between the BL region and the cavity. In this study, cavity vortex shedding as in shown by Savoie [12] in figure 2.1.7(b) was not visualized because Savoie's study was at Re_d 624 and the highest Re_d tested in this study was 170.

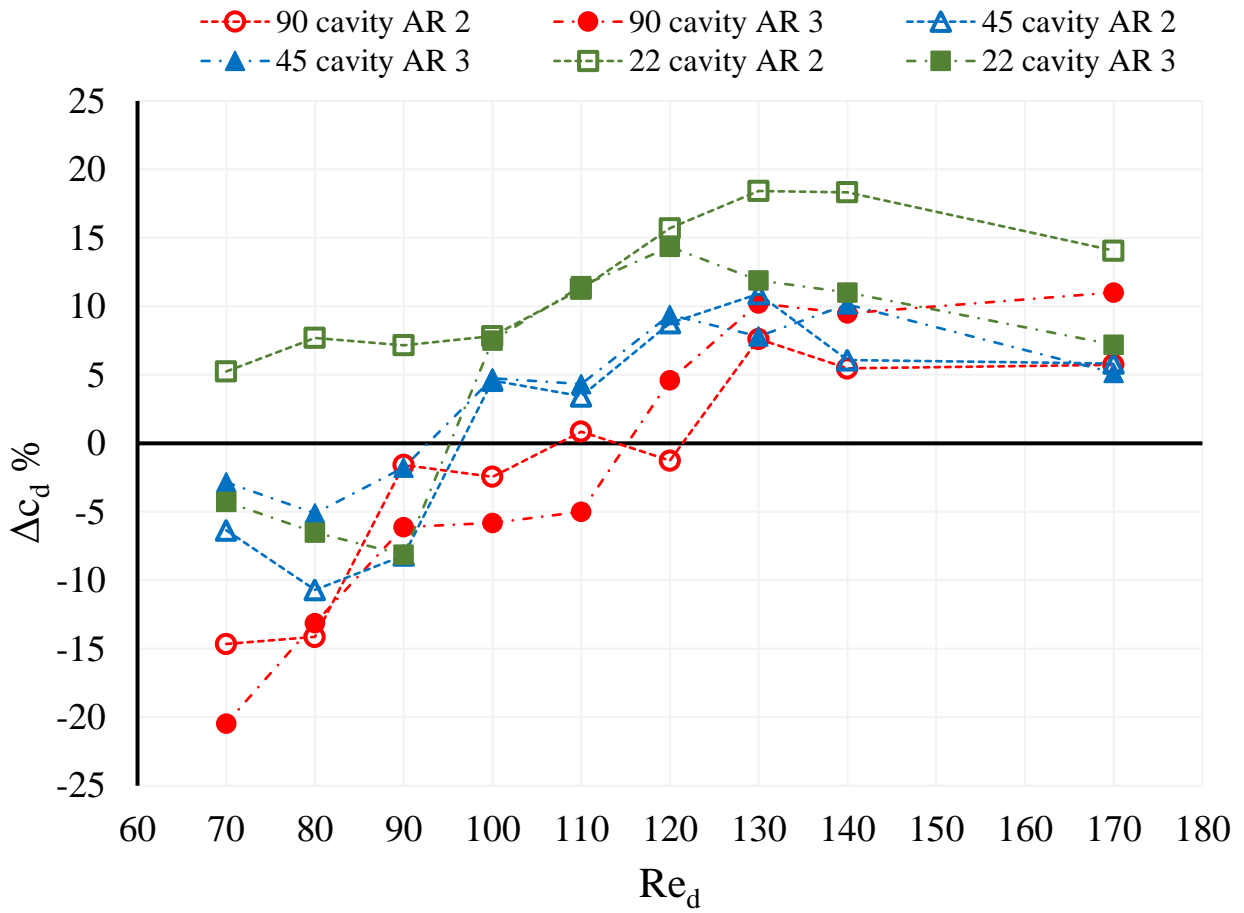


Figure 4.2.3(b): Percentage change in surface drag coefficient for various higher

The variation in drag reduction for the different models suggests that there is an optimum cavity geometry for which the drag reduction is highest at a certain Re_d . Also, there exists a critical Re_d region for each of these models beyond which there is a net increase in surface drag. Table 4.3 shows the percentage of drag reduction of various models at various Re_d .

Table 4.3: Percentage of drag reduction of various models at various Re_d

Models/ Re	4.5	5.5	6.5	7.5	8.5	70	80	90	100	110	120	130	140	170
90° cavity AR 2	-8.80	-10.88	-11.53	-17.43	-17.28	-14.65	-14.14	-1.58	-2.44	0.86	-1.26	7.62	5.47	5.74
90° cavity AR 3	-12.38	-13.83	-16.91	-20.30	-21.54	-20.45	-13.13	-6.11	-5.82	-4.99	4.62	10.23	9.48	11.02
45° cavity AR 2	-18.63	-19.08	-19.76	-24.84	-26.33	-6.36	-10.70	-8.18	4.58	3.44	8.77	10.91	6.07	5.83
45° cavity AR 3	-8.01	-11.26	-13.81	-16.36	-15.09	-2.85	-5.10	-1.78	4.76	4.32	9.37	7.82	10.14	5.14
22° cavity AR 2	2.97	7.15	4.77	-0.87	0.10	5.25	7.70	7.17	7.83	11.27	15.70	18.42	18.33	14.07
22° cavity AR 3	-8.49	-8.28	-10.20	-11.29	-11.03	-4.28	-6.52	-8.13	7.52	11.47	14.35	11.91	11.01	7.20

Table 4.4 shows the list of mean velocity magnitudes (\bar{V}) at the dividing streamline for all the models at $Re_d 8.5$.

Table 4.4: Mean slip velocity magnitude for various models

Model	\bar{V} (mm/s)	$\frac{\bar{V}}{U_0} \times 100\%$
90° cavity AR 2	1.166	2.57
90° cavity AR 3	1.157	2.55
45° cavity AR 2	1.192	2.63
45° cavity AR 3	1.155	2.55
22° cavity AR 2	1.022	2.55
22° cavity AR 3	1.163	2.56

The mean slip velocity at the dividing streamline is approximately 2.55% of the freestream velocity for all the models. As a result for the cavity embedded models, the outer BL flow experiences a reduced friction drag because of this partial slip condition as measured on the dividing streamline. Figure 4.2.4 shows the u-velocity profile at the center of a single arbitrarily chosen cavity which is located halfway between the tip of the upstream cavity wall to the tip of the downstream cavity wall. The velocity is non-dimensionalized with respect to the mean slip velocity magnitude of respective models (from table 4.4) and the y distance is non-dimensionalized with respect to cavity depth. The y/d value where the plots reach $u/\bar{V} = 1$ shows the estimation of the non-dimensional height of the dividing streamline as measured from the bottom of the cavity. As seen from the vortex visualization, the AR 3 models have diving streamlines that dip closer towards the bottom of the cavity. Table 4.5 shows the

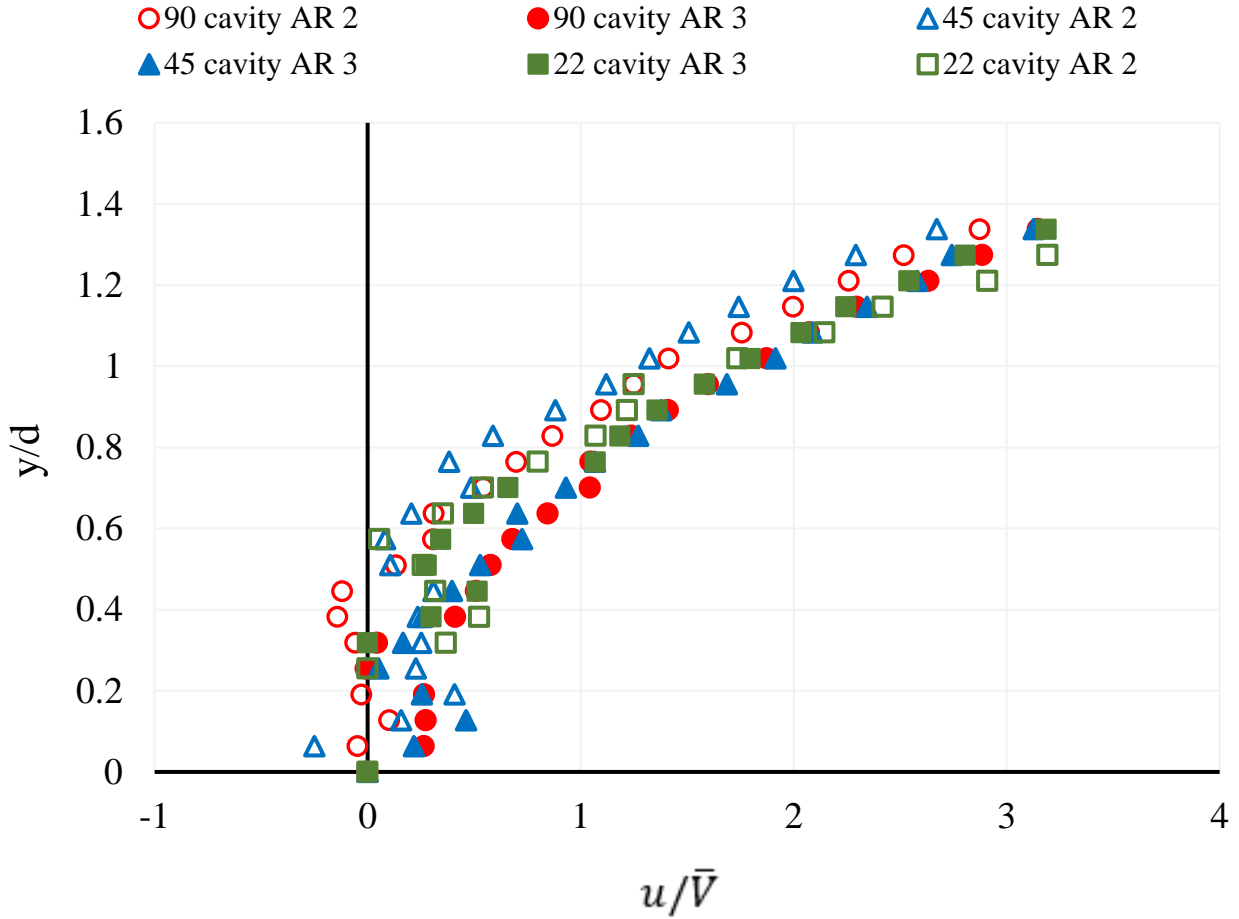


Figure 4.2.4: u -velocity profile at the center of a cavity for all the models at $Re_d 8.5$

comparison of the non-dimensional height of the dividing streamline at the center of a cavity for all the models at the $Re_d 8.5$.

Similarly, figure 4.2.5 shows the velocity distribution of the local u velocity along the top of a single cavity for all the models at $Re_d 8.5$. The figure shows that the velocity distribution is similar for all the AR 3 models. Except for the model 22° cavity AR 2, both the AR 2 models of cavity inclination 90° and 45° show a similar velocity distribution along the top of the cavity. The AR 2 models exhibit a lower maximum value because the dividing

streamline for these models did not curve as far downwards towards the bottom of the cavity as the AR 3 models.

Table 4.5: Dividing streamline height at the center of cavity for $Re_d 8.5$

Model	y/d
90 cavity AR 2	0.83
90 cavity AR 3	0.64
45 cavity AR 2	0.89
45 cavity AR 3	0.70
22 cavity AR 2	0.83
22 cavity AR 3	0.70

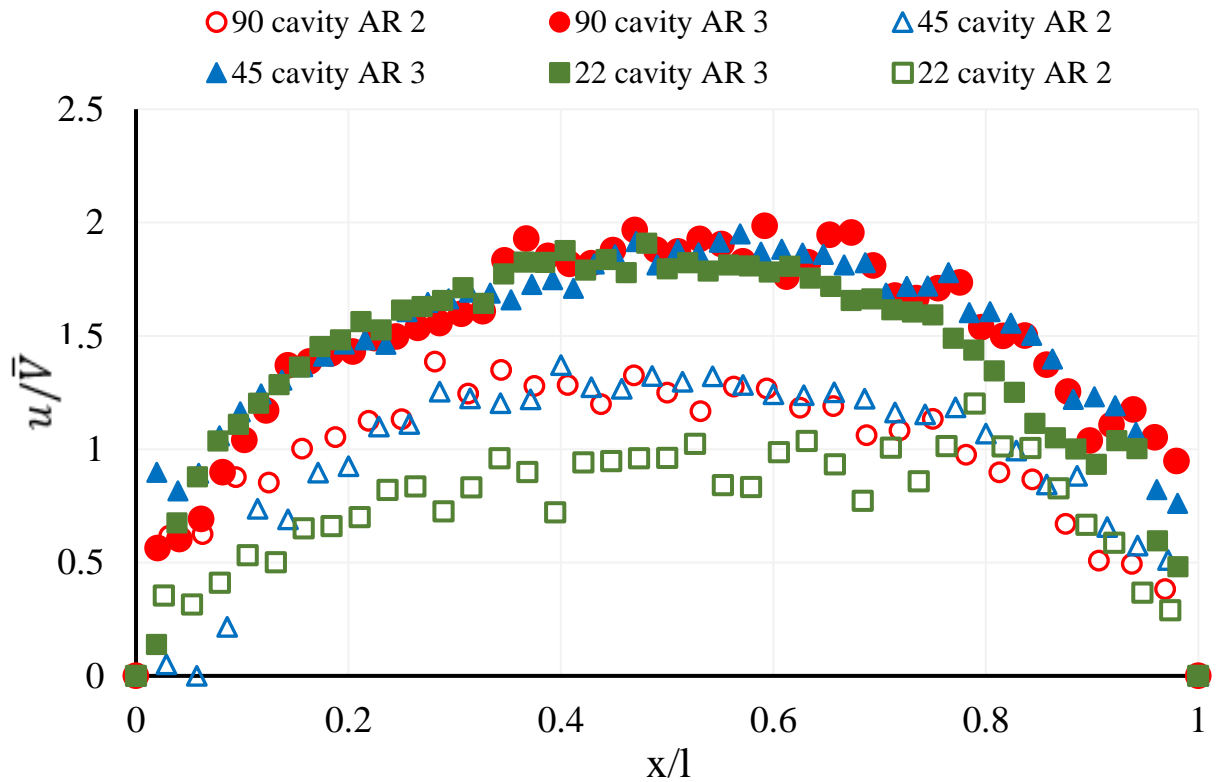


Figure 4.2.5: u -velocity distribution on the top of a cavity for all the models at $Re_d 8.5$

4.3 UNCERTAINTY CALCULATION

Uncertainty of any variable ‘x’ in an experiment is associated with the bias error and the precision error as shown in equation 4.4 [57].

$$\epsilon_X = \sqrt{\epsilon_{bX}^2 + \epsilon_{pX}^2} \quad (4.4)$$

Where, ϵ_X is the uncertainty, ϵ_{bX} is the bias error and ϵ_{pX} is the precision error of the variable ‘x’. The precision error is calculated using the equation 4.5 [57],

$$\epsilon_{pX} = t_{95\%,\nu} \frac{\sigma_x}{\sqrt{N_x}} \quad (4.5)$$

Where, N_x is the number of samples of x. $t_{95\%,\nu}$ is the t-value distribution for 95% confidence interval and σ_x is the standard deviation of variable ‘x’. The bias error from the DPIV measurements is dependent on the type of correlation algorithm, method used to determine the peak, the size of the processing window and its overlapping percentage [58, 59]. If the condition stated in equation 4.6 is fulfilled, then the bias error due to the displacement gradient error is negligible [58].

$$\frac{M\Delta t\Delta u}{\sqrt{d_r^2 + d_e^2}} < 1 \quad (4.6)$$

Where, M is the magnification of the camera lens, Δt is the time step between an image pair, Δu is the deviation of u-velocity from the mean velocity in the interrogation region, d_r is the pixel size, and d_e is the diameter of a particle. The value of the left hand side expression of equation 4.8 is calculated as 9.04×10^{-4} for the nominal case. Based on the parameters of Insight mentioned in Appendix B, the DPIV bias error for this study is ensured to be less than 0.01 pixels which is equal to $\epsilon_{bu} = 1.6 \times 10^{-4}$ mm/s for the velocity variable. The bias error for

the height of inlet and outlet is the least value (0.8 mm) of the y-axis in the flow field which is dependent on both the resolution of the camera and the size of the processing window in the insight.

Finally, the uncertainty for the surface drag coefficient and the percentage change of drag coefficient is obtained numerically from the normalized uncertainty of the variables u-velocity and Δy . To understand the propagation of error from u and Δy to the drag coefficient, the data is randomly varied for the u-velocity and Δy within their respective normalized uncertainty. The uncertainty of the drag coefficient is then obtained from comparison of drag coefficient from randomly varied data set and the actual experimental values. Due to the nature of the random function used, the steps are repeated 16 times to obtain an average uncertainty of the experiment. Equation 4.7 is then used to calculate the uncertainty in the percentage change of drag coefficient in comparison to the flat plate.

$$\varepsilon_{\Delta c_d\%} = \sqrt{\varepsilon_{c_{d\ flat\ plate}}^2 + \varepsilon_{c_{d\ cavity\ plate}}^2} \quad (4.7)$$

Table 4.3 shows the precision and bias error of the control surface height and velocity variable for a nominal case of Re_d 70 and Re_d 4.5 for the flat plate. Δc_d % value includes comparison with the surface drag coefficient obtained from 90° cavity AR 2 model. DPIV is known to produce an accurate velocity field if the parameters used for correlation of particles and peak finding algorithm are well-suited for the study [60]. The bias error from DPIV is much smaller for the velocity variable so the uncertainty of velocity is mainly due to the precision error. However, for the calculation of control surface height, the bias error is more dominant. This is not due to the error from DPIV calculation but rather results from the limitation of the camera's resolution. The percentage change of surface drag coefficient with

the uncertainty for the 90° cavity AR 2 model is $14.64 \pm 5\%$ for Re_d 70 and $8.805 \pm 1.4 \%$ for Re_d 4.5. The uncertainty for other cases are in similar range and are within the bounds to come to a conclusive result for this study.

Table 4.3: List of error values and uncertainty

	Variable	Bias error	Precision error	Uncertainty	Measured value
Higher Re_d	h_{inlet} (mm)	0.8	0.068	0.8	8.95
	h_{outlet} (mm)	0.8	0.23	0.83	19.52
	u (mm/s)	0.00016	0.55	0.55	18.67
	c_d			0.00047	0.0019
	Δc_d %			5	14.64
Lower Re_d	h_{inlet} (mm)	0.8	0.23	0.83	28
	h_{outlet} (mm)	0.8	0.57	0.98	64
	u (mm/s)	0.00016	0.39	0.39	18.67
	cd			0.002	0.0175
	Δcd %			1.4	8.805

The plots from section 4.2 with the addition of uncertainty as error bars are shown in figure 4.3.1(a) & (b) for the lower and higher Re_d experiments, respectively.

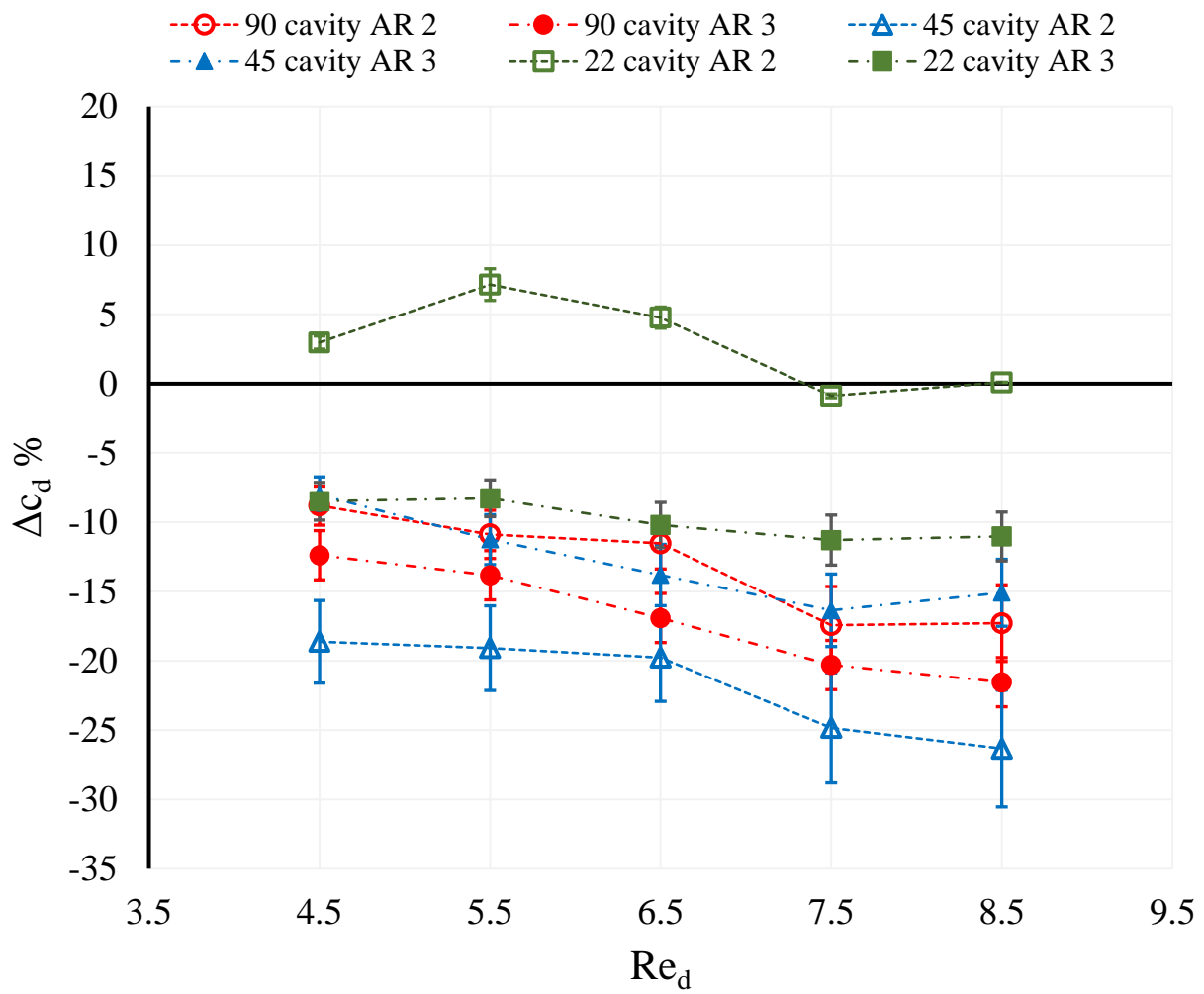


Figure 4.3.1: Percentage change in surface drag coefficient for various low Re_d with the error bars

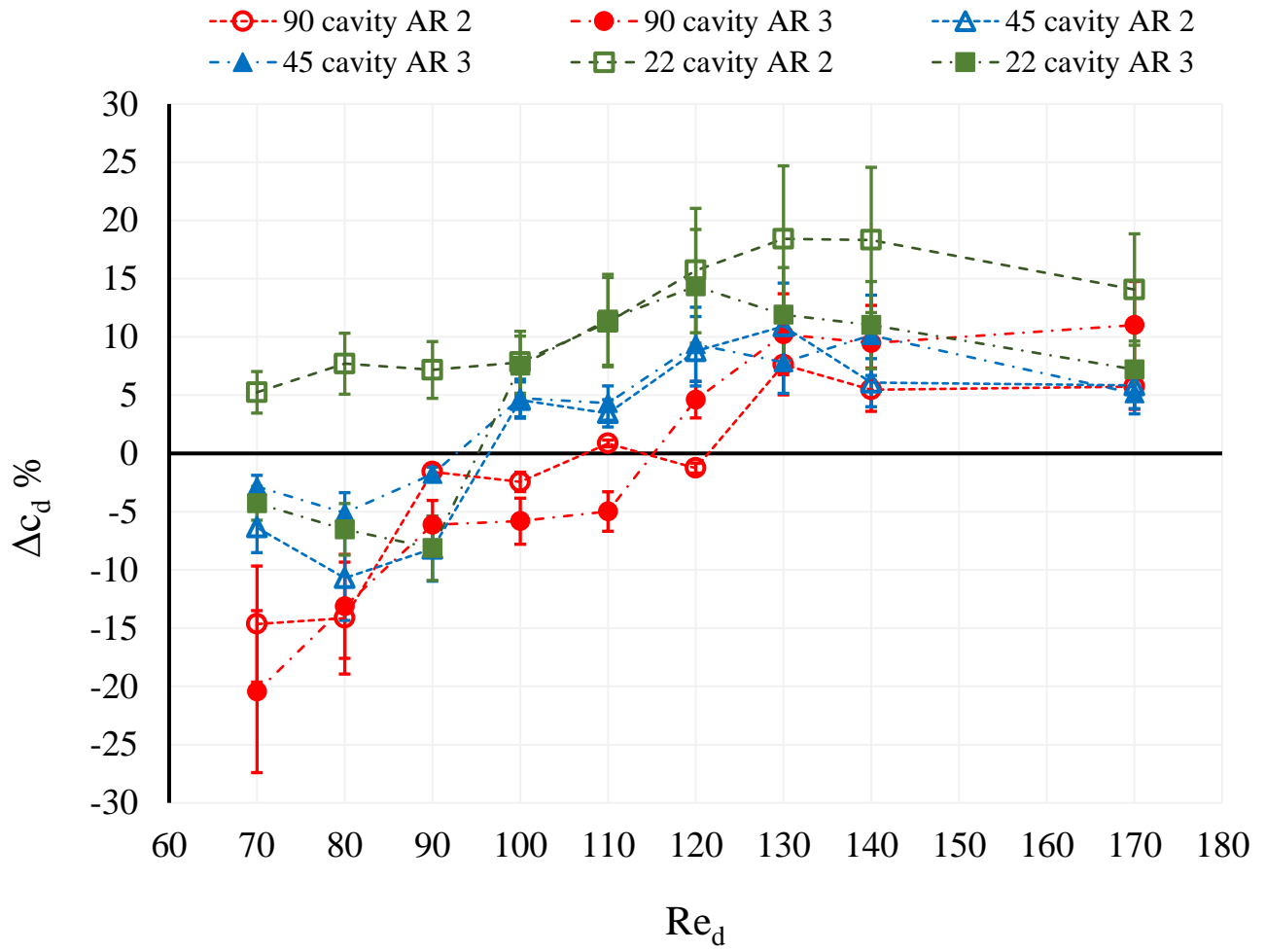


Figure 4.3.2: Percentage change in surface drag coefficient for various higher Re_d including error bars

CHAPTER 5

CONCLUSION

This is a bio-inspired study that aimed to explain the aerodynamic benefits offered by the presence of scales on the wings of the Monarch butterfly [28]. Studies have shown that the presence of scales do have a benefit on the formation of the leading edge vortex [61, 62]. However, this study focused on the potential reduction of surface or skin drag due to the presence of the scales, particularly for the regime of the flight Re_d of 5 to 25, but to also show that slightly higher Re_d would result in an increase in drag. As mentioned on chapter 1, it was hypothesized that the beneficial effect of the scales for flow passing transverse to the rows was attributed to the vortices trapped inside each cavity between the scales resulting in a partial slip condition to the BL flow resulting in a reduction of surface drag or skin friction. This mechanism is referred to as the ‘roller-bearing effect’ which is analogous to the reduced friction for a solid object sliding over a roller-bearing surface. Initially, this study documented the cavity vortex and the roller-bearing effect for a model with embedded rectangular cavities of AR 2. The surface drag reduction was calculated to be 8.8% to 17.53% for the lower Re_d regime of 4.5 to 8.5. For the critical Re_d region of 90 to 120, the drag reduction decreased to approximately zero which suggested the breaking up of the dividing streamline resulting in the mixing of low momentum fluid in the cavity with the high momentum fluid from the outer BL flow. This resulted in a net increase in surface drag for higher Re_d 130 to 170.

With the favorable results on the first cavity model studied, more models with varied cavity geometries were constructed. Experiments were conducted on models with cavity walls of 90° , 45° and 22° inclination with AR 2 and 3. The purpose was to better replicate the Monarch butterfly's cavity geometry formed by the scales which is estimated from scale measurements to be around 45° with AR 2 [2] and 22° with AR 3, depending on the location of the wing. Experimentation on the various cavity embedded models identified the geometry with the best surface drag reduction result. For lower Re_d 4.5 to 8.5, a 45° cavity with AR 2 had the highest surface drag reduction ranging from 18.63% to 26.33%. The drag reduction for the 22° cavity with AR 3 ranged from 8.28% to 11.29%. As the flow Re_d was increased, all the models exhibited a critical Re_d region from around 90 to 120, beyond which there was an increase in surface drag. This showed that the angled cavities, more accurately replicating the butterfly scales, did in fact have the highest surface drag reduction at the flight Re_d for the butterfly.

On the contrary, models with 22° cavity with AR 2 resulted in net surface drag increase even for the low Re_d cases. The reason for the surface drag increase could be the much smaller size of the single dominant vortex and more contact of the outer BL flow with the cavity walls. The maximum surface drag increase was up to 18.42% for this model. The rectangular model with AR 3 had the second best surface drag reduction result ranging from 12.38% to 21.54% for lower Re_d . This is interesting as the lower Re_d 4.5 to 8.5 vortex visualization of this model did not show a single dominant vortex, but rather two distinct smaller corner vortices. Thus, to achieve surface drag reduction the presence of a single entrapped vortex is not necessary as long as the existence of the dividing streamline is intact along which a partial slip condition to the outer BL flow is maintained. Both the rectangular cavities resulted in surface drag reduction

for the lower Re_d and even had the best surface drag reduction results for Re_d 70 and 80 as the cavity vortex increased in size. Not only did the angled scales perform better at lower Re_d (consistent with Monarch flight speeds), but the scales serves other functions as well for the animal. The inclined scales also function better as a hydrophobic surface to help keep the wings dry and less contaminated [25] while lying more flat also provides the rich color [24]. Vertical scales could impede these functionalities for the butterfly.

5.1 LIMITATIONS

This study was limited to the results of Re_d 4.5 to 8.5 on the lower regime and Re_d 70 to 170 on the higher range. These two different Re_d regimes were obtained using two different fluids, water (viscosity 1 cSt) and oil (viscosity 20 cSt). The higher and lower Re_d were capped based on the highest and lowest operable speed of the traverse. Likewise, the experiments were performed in the tow tank, so the timeframe of the data acquisition was limited and directly proportional to the length of the tow-tank. Another limitation of this study was the laser sheet perpendicular to the surface of the model. This resulted in the inclined cavity embedded models casting shadows in its respective cavity and blocking the view inside of it. To work around this, the laser sheet was angled up to 45° for inclined cavity models. It helped to view the cavity vortex with more clarity but still blocked the corner vortices. Moreover, with the increase in inclination of the laser sheet, its brightness decreased because more of the laser light reflected back. This effect was noticed particularly on the vortex visualization results.

5.2 FUTURE WORK

It is hypothesized that the increase in surface drag as the Re_d increases beyond the critical region is because of the mixing of the high momentum BL fluid with the lower momentum cavity vortex fluid that slowly begins to occur as instability of the cavity flow begins to take place. This process results in net surface drag increase as it reduces the momentum in the BL. Comparison of u_{rms} and v_{rms} values on the dividing streamline for a drag reduction case and a drag increase case should be able to confirm if the increase in surface drag is actually due to the fluids mixing between the two regions. Likewise, the analysis of correlation of slip velocity along the dividing streamline and the surface drag reduction would be able to provide more insight on why some of the cavity models have better drag reduction than others.

Finally, more experiments could be carried out for Re_d from 10 to 60 to study the trend of surface drag change with Re_d as it reaches the critical region. This could be achieved by using a different oil with viscosity of 5 cSt or by varying the cavity depth 'd'

REFERENCES

1. Industries, Z. *Product information for linearized motor traverse*. Available from: <https://www.zaber.com>.
2. Lang, A., Slegers, N., Yoder, J., Schreiber, W., , *The beneficial effect of butterfly scales*, in *Collaborative research proposal for NSF*. 2014.
3. Jones, R.A., *Drag measurements over embedded cavities inspired by the microgeometry formed by butterfly scales*. 2011: The University of Alabama.
4. Shen, C. and J. Floryan, *Low Reynolds number flow over cavities*. *The Physics of fluids*, 1985. **28**(11): p. 3191-3202.
5. Leibenguth, C.M., *Drag reduction over a low Reynolds number cavity surface*. 2012: The University of Alabama.
6. Gatski, T. and C. Grosch, *Embedded cavity drag in steady laminar flow*. *AIAA journal*, 1985. **23**(7): p. 1028-1037.
7. Davis, M., *Design of flat plate leading edges to avoid flow separation*. *AIAA Journal*, 1980. **18**(5): p. 598-600.
8. Weiss, R.F. and B.H. Florsheim, *Flow in a cavity at low Reynolds number*. *The Physics of Fluids*, 1965. **8**(9): p. 1631-1635.
9. Takematsu, M., *Slow viscous flow past a cavity*. *Journal of the Physical Society of Japan*, 1966. **21**(9): p. 1816-1821.
10. Ashcroft, G. and X. Zhang, *Vortical structures over rectangular cavities at low speed*. *Physics of Fluids*, 2005. **17**(1): p. 015104.
11. Scholle, M., A. Rund, and N. Aksel, *Drag reduction and improvement of material transport in creeping films*. *Archive of Applied Mechanics*, 2006. **75**(2): p. 93-112.
12. Savoie, R. and Y. Gagnon, *Numerical simulation of the flow over a model of the cavities on a butterfly wing*. *Journal of Thermal Science*, 1995. **4**(3): p. 185-192.

13. Bomphrey, R.J., et al., *The aerodynamics of Manduca sexta: digital particle image velocimetry analysis of the leading-edge vortex*. Journal of Experimental Biology, 2005. **208**(6): p. 1079-1094.
14. Taneda, S., *Visualization of separating Stokes flows*. Journal of the Physical Society of Japan, 1979. **46**(6): p. 1935-1942.
15. Howard, E. and A.K. Davis, *The fall migration flyways of monarch butterflies in eastern North America revealed by citizen scientists*. Journal of Insect Conservation, 2009. **13**(3): p. 279-286.
16. Urquhart, F. and N. Urquhart, *Autumnal migration routes of the eastern population of the monarch butterfly (Danaus p. plexippus L.; Danaidae; Lepidoptera) in North America to the overwintering site in the Neovolcanic Plateau of Mexico*. Canadian Journal of Zoology, 1978. **56**(8): p. 1759-1764.
17. Urquhart, F.A., *Found at last: the monarch's winter home*. National Geographic, 1976. **150**(2): p. 161-173.
18. Brower, L.P., *Understanding and misunderstanding the migration of the monarch butterfly(Nymphalidae) in North America: 1857-1995*. Journal of the Lepidopterists Society, 1995. **49**(4): p. 304-385.
19. Shyy, W., et al., *An introduction to flapping wing aerodynamics*. Vol. 37. 2013: Cambridge University Press.
20. Sun, M., *Insect flight dynamics: stability and control*. Reviews of Modern Physics, 2014. **86**(2): p. 615.
21. Garber, S.D., *The urban naturalist*. 2013: Courier Corporation.
22. ; US Forest service, USDA]. Available from: <https://www.fs.usda.gov/>.
23. Klots, A.B., *Field guide to the butterflies of North America, East of the Great Plains*. 1951.
24. Ingram, A., *Functional Surfaces in Biology* Vol. Ch. 15. 2009, Berlin: Springer-Verlag.
25. Fang, Y., et al., *Effects of methanol on wettability of the non-smooth surface on butterfly wing*. Journal of Bionic Engineering, 2008. **5**(2): p. 127-133.
26. Goodwyn, P.P., et al., *Waterproof and translucent wings at the same time: problems and solutions in butterflies*. Naturwissenschaften, 2009. **96**(7): p. 781-787.

27. Wagner, T., C. Neinhuis, and W. Barthlott, *Wettability and contaminability of insect wings as a function of their surface sculptures*. Acta Zoologica, 1996. **77**(3): p. 213-225.
28. Slegers, N., et al., *Beneficial aerodynamic effect of wing scales on the climbing flight of butterflies*. Bioinspiration & biomimetics, 2017. **12**(1): p. 016013.
29. Bushnell, D. *Turbulent drag reduction for external flows*. in *21st Aerospace Sciences Meeting*. 1983.
30. Nachtigall, W., *Aerodynamische Messungen am Tragflügelssystem segelnder Schmetterlinge*. Zeitschrift für vergleichende Physiologie, 1967. **54**(2): p. 210-231.
31. Tavoularis, S., A. Goldman, and J. Floryan. *Separation and reattachment in flows over asymmetric cavities at small Reynolds numbers*. in *Tenth Canadian Congress of applied mechanics: CANCAM'85. Proceedings*. 1985.
32. Chebbi, B. and S. Tavoularis, *Low Reynolds number flow in and above asymmetric, triangular cavities*. Physics of Fluids A: Fluid Dynamics, 1990. **2**(6): p. 1044-1046.
33. Prandtl, L., *On the Motion of a Fluid with Very Small Viscosity* Verh. Int. Math. Kongr. 3rd. Heidelberg, 1904: p. 484-491.
34. Tani, I., *History of boundary layer theory*. Annual review of fluid mechanics, 1977. **9**(1): p. 87-111.
35. Goldstein, S., *Modern developments in fluid dynamics: an account of theory and experiment relating to boundary layers, turbulent motion and wakes*. 1938: Clarendon Press.
36. Hocking, L., *A moving fluid interface on a rough surface*. Journal of Fluid Mechanics, 1976. **76**(4): p. 801-817.
37. Priezjev, N.V. and S.M. Troian, *Influence of periodic wall roughness on the slip behaviour at liquid/solid interfaces: molecular-scale simulations versus continuum predictions*. Journal of Fluid Mechanics, 2006. **554**: p. 25-46.
38. Wang, C., *Flow over a surface with parallel grooves*. Physics of Fluids, 2003. **15**(5): p. 1114-1121.
39. Wang, C., *Stokes flow due to the sliding of a smooth plate over a slotted plate*. European Journal of Mechanics-B/Fluids, 2001. **20**(5): p. 651-656.
40. O'Brien, V., *Closed streamlines associated with channel flow over a cavity*. The Physics of Fluids, 1972. **15**(12): p. 2089-2097.

41. Johnson, T.J., et al., *Low Reynolds number Couette flow facility for drag measurements*. Review of Scientific Instruments, 2010. **81**(9): p. 095103.
42. Lang, A., Johnson, T., , *Drag reduction over 2D square embedded cavities in Couette flow*.
43. Bechert, D., M. Bartenwerfer, and G. Hoppe, *Turbulent drag reduction by nonplanar surfaces—A survey on the research at TU/DLR Berlin*, in *Structure of Turbulence and Drag Reduction*. 1990, Springer. p. 525-543.
44. Durst, F., J. Jovanović, and J. Sender, *LDA measurements in the near-wall region of a turbulent pipe flow*. Journal of Fluid Mechanics, 1995. **295**: p. 305-335.
45. Archbold, E. and A. Ennos, *Displacement measurement from double-exposure laser photographs*. Optica Acta: International Journal of Optics, 1972. **19**(4): p. 253-271.
46. Dudderar, T. and P. Simpkins, *Laser speckle photography in a fluid medium*. Nature, 1977. **270**(5632): p. 45-47.
47. Barker, D. and M. Fourney, *Measuring fluid velocities with speckle patterns*. Optics letters, 1977. **1**(4): p. 135-137.
48. Adrian, R.J., *Scattering particle characteristics and their effect on pulsed laser measurements of fluid flow: speckle velocimetry vs particle image velocimetry*. Applied optics, 1984. **23**(11): p. 1690-1691.
49. Pickering, C.J. and N.A. Halliwell, *Speckle photography in fluid flows: signal recovery with two-step processing*. Applied optics, 1984. **23**(8): p. 1128-1129.
50. Adrian, R.J. and C.-S. Yao, *Pulsed laser technique application to liquid and gaseous flows and the scattering power of seed materials*. Applied optics, 1985. **24**(1): p. 44-52.
51. Willert, C.E. and M. Gharib, *Digital particle image velocimetry*. Experiments in fluids, 1991. **10**(4): p. 181-193.
52. Adrian, R.J., *Particle-imaging techniques for experimental fluid mechanics*. Annual review of fluid mechanics, 1991. **23**(1): p. 261-304.
53. TSI, *Insight 4G manual*.
54. White, F.M. and J. Majdalani, *Viscous fluid flow*. Vol. 3. 2006: McGraw-Hill New York.
55. Schlichting, H. and K. Gersten, *Boundary-layer theory*. 2016: Springer.

56. Janna, W.S., *Introduction to fluid mechanics*. 2020: CRC press.
57. Coleman, H.W. and W.G. Steele, *Experimentation, validation, and uncertainty analysis for engineers*. 2018: John Wiley & Sons.
58. Forliti, D., P.J. Strykowski, and K. Debatin, *Bias and precision errors of digital particle image velocimetry*. *Experiments in Fluids*, 2000. **28**(5): p. 436-447.
59. Raffel, M., et al., *Particle image velocimetry: a practical guide*. 2018: Springer.
60. Huang, H., D. Dabiri, and M. Gharib, *On errors of digital particle image velocimetry*. *Measurement Science and Technology*, 1997. **8**(12): p. 1427.
61. Wilroy, J.A., *The effect of butterfly-scale inspired patterning on leading-edge vortex growth*. 2016: The University of Alabama.
62. Wilroy, J., R.A. Wahidi, and A. Lang, *Effect of butterfly-scale-inspired surface patterning on the leading edge vortex growth*. *Fluid Dynamics Research*, 2018. **50**(4): p. 045505.

APPENDIX A: TRAVERSE SPECIFICATION

Figure A1 below shows the thrust vs speed comparison of the Zaber ALST0750B-E01-KT07U traverse [1]. The net load that is towed by the traverse is around 60 lb which includes the camera setup, plate and structure that connects the model to the traverse. Based on the blue curve that represents the type-B traverse, the maximum limit is capped around 50 mm/s.

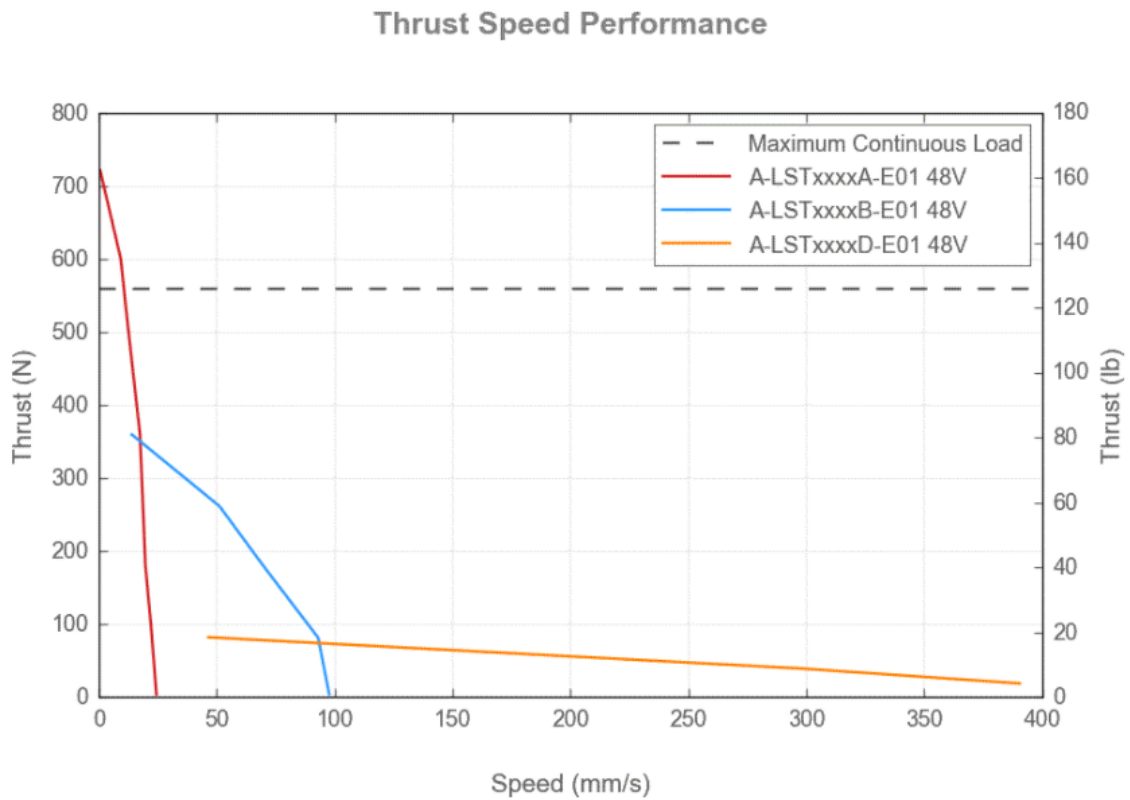


Figure A1: Thrust vs speed for different types of A-LST models, Zaber industries [1]

APPENDIX B: DATA PROCESSING AND POST PROCESSING

Figure B1 shows a typical processing window of Insight 4G.

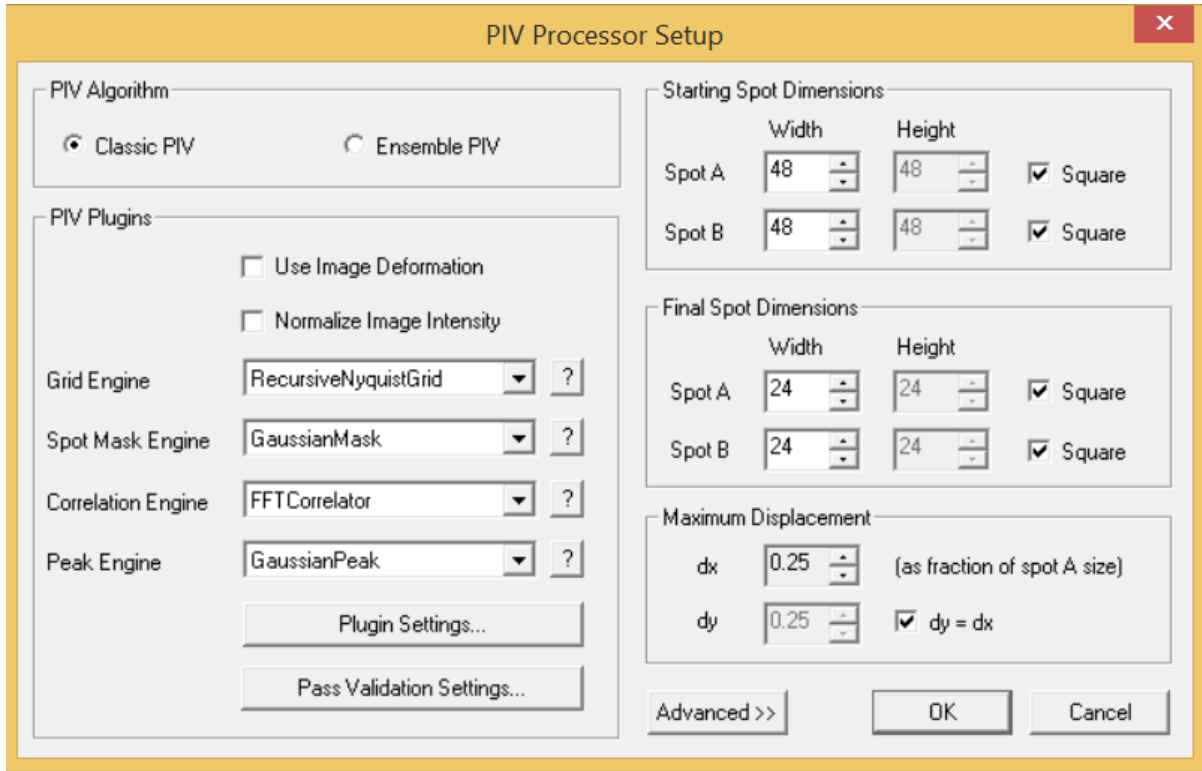


Figure B1: Processing window from Insight 4G

The Recursive Nyquist grid engine processes the images in multiple passes. The results from the first pass, which resembles a typical PIV grid processing, is used for optimization in the second processing pass. Zero pad mask is used to compute the average of all pixels and subtract each pixel value from the average to reduce the gray value of pixels from the noise. Fast Fourier Transform (FFT) is the correlation used to identify the group of particles. Gaussian peak is

used for the peak engine to locate the correlation peak by fitting a Gaussian curve to the highest peak and other four nearest neighbors.

In some cases, the highest correlation peak might result due to pairing of random particles rather than the actual group of particles. So, validation of vector field is necessary to accurately represent the vector field of the flow. A typical validation window is shown in figure B2. Local

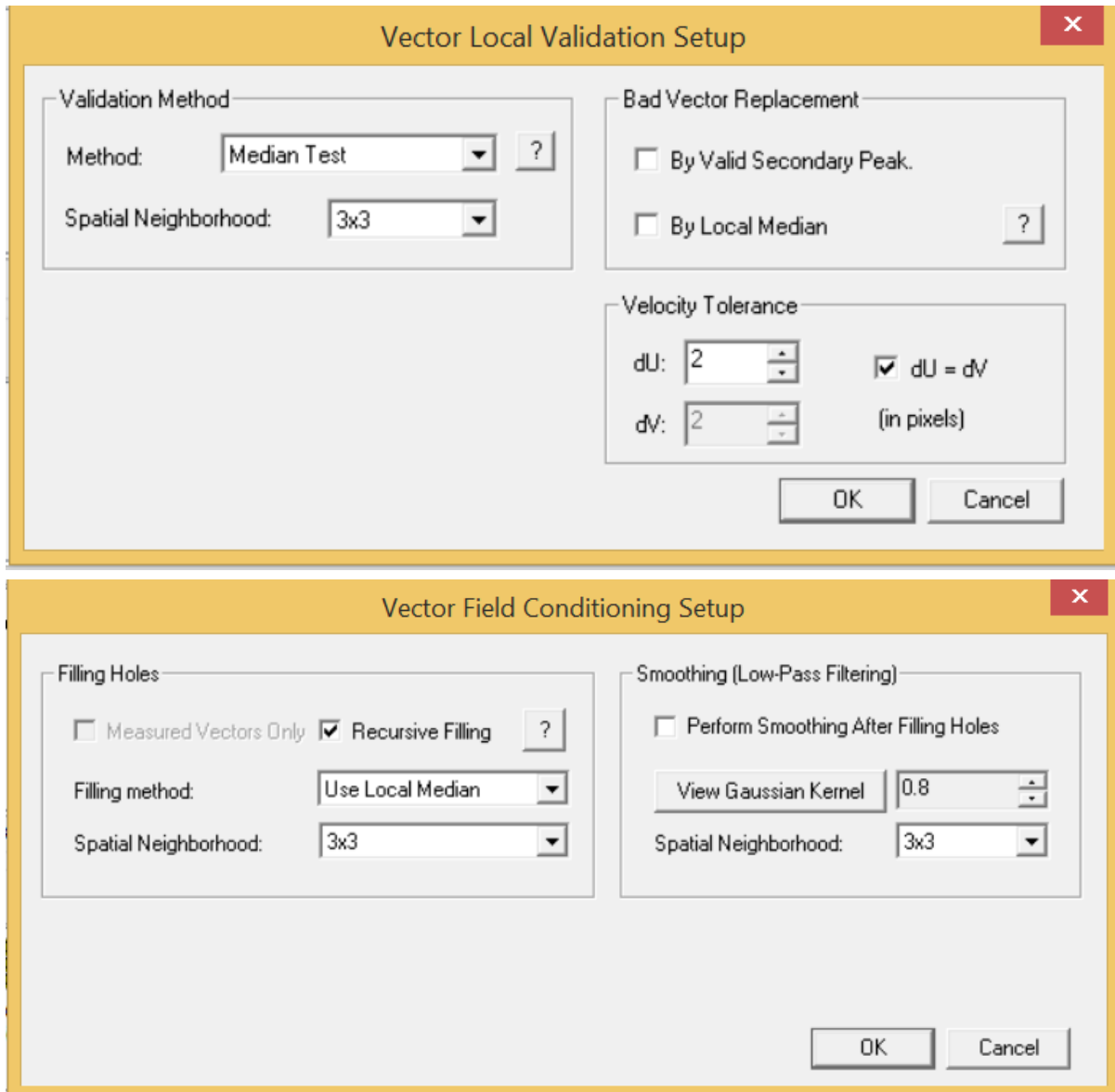


Figure B2: Post processing window from Insight 4G for the vector validation and the vector conditioning

median method is used for the vector validation, in which a reference vector is calculated as the median of the vectors around the current vector. If the difference between the reference vector and the current vector exceeds the pre-defined tolerance, the result is failed validation, and the current vector is interpolated by replacing it with either the secondary peaks or the median vector.

APPENDIX C: LEADING EDGE DESIGN

The LE profile is designed to be elliptical based on the numerical study of Davis [7] as shown in the figure C1. The elliptical profile consists of a single low pressure coefficient region which then gradually increases as the flow slows down to the freestream velocity.

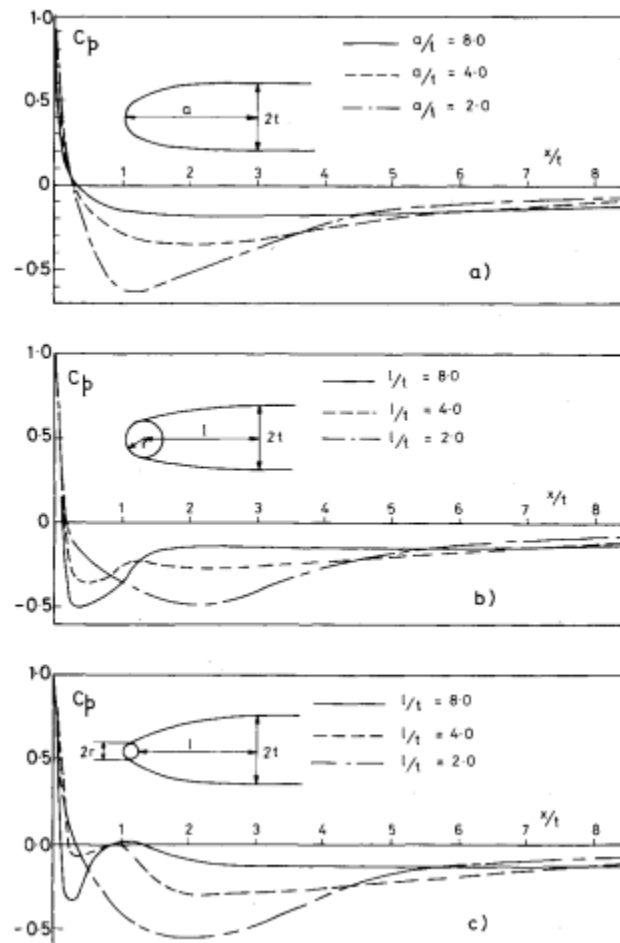


Figure C1 Distribution of surface pressure coefficient for a) elliptical nose profiles b) double arc nose profiles $r/t = 0.5$ c) $r/t = 0.25$, Davis [7]

The study recommends that to ensure that there is no boundary layer separation on the nose of the LE, the ratio for major to minor axis of elliptical profile should be $a/t > 5$. However, for

our study, $a/t = 4$ because we do not want the boundary layer to grow larger in the upstream location.

Also, the study mentions that for experiments with $a/t = 4$, the flow did not separate even when subjected to intense disturbances. From figure C2, we can conclude that the boundary layer parameter λ is far from the critical value -12 where the boundary layer separation occurs.

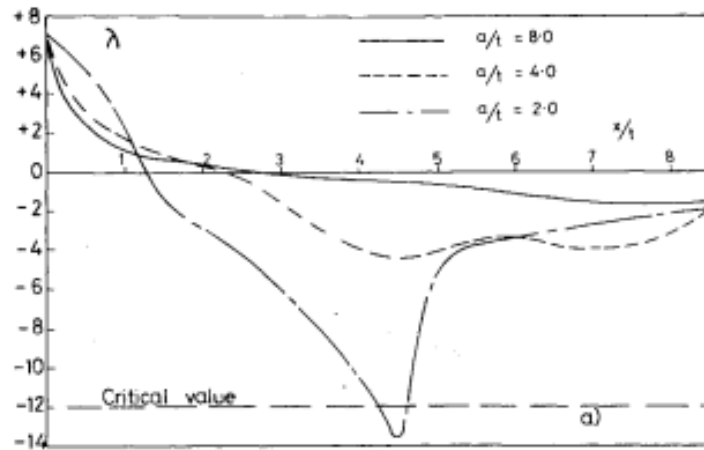


Figure C2: Distribution of boundary layer parameter for elliptical nose, Davis [7]

Diagram of LE

Figure C3 shows the elliptical LE design used for all the models in this study.

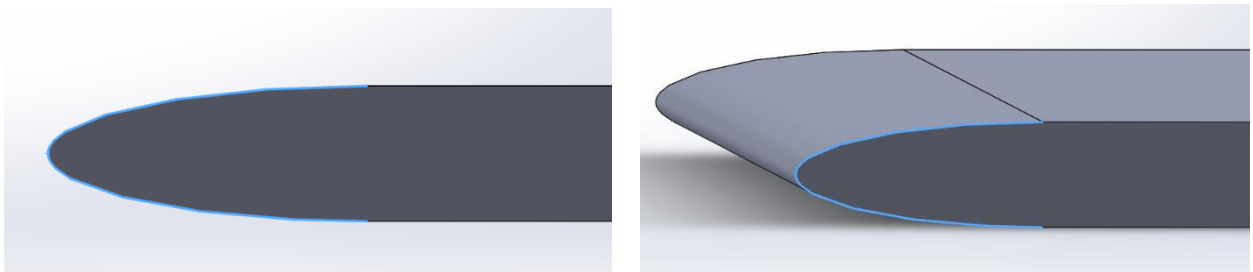


Figure C3: LE of the smooth flat plate

APPENDIX D: ANSYS FLUENT SIMULATION OF FLOW OVER SMOOTH FLAT PLATE

PLATE

This section includes the supplement information for 2D steady simulation of flow over a smooth flat plate on Ansys Fluent. Figure D1 shows the diagram of the flat plate model and the flow domain used for the simulation.



Figure D1: 2D smooth flat plate model

Figure D2 shows the mesh of the domain and a zoomed in view of the mesh around the flat plate. The total height of the domain is 6 m and the radius of the curvature is 3 m from the LE of the plate.

The solver used for this simulation is steady, pressure based, viscous laminar model. The inlet is modeled with a velocity inlet of the freestream velocity and the plate is modeled as a no-slip condition wall. The outlet is based on pressure-outlet and solved for 10,000

iterations. It was also confirmed that refining the mesh also provided results similar to the less refined mesh.

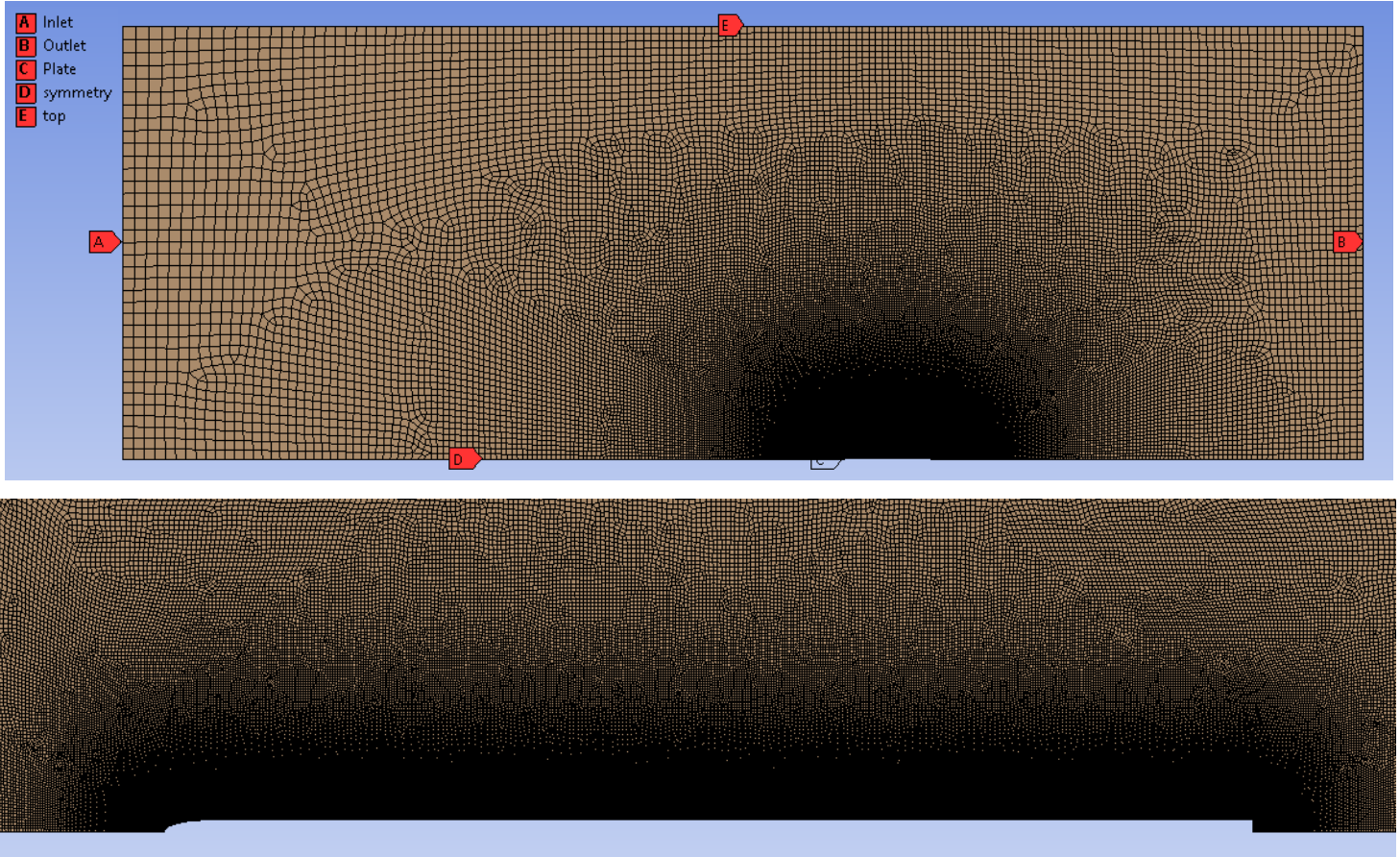


Figure D2: Mesh of the fluent simulation

The height of the first layer is 1×10^{-6} m from the surface of the plate. The number of inflation layers is 40 with a growth rate of 1.1.

Details of "Mesh" ▾ 🔍 □ ×	
+ Display	
- Defaults	
Physics Preference	CFD
Solver Preference	Fluent
Element Order	Linear
<input type="checkbox"/> Element Size	Default (0.45587 m)
Export Format	Standard
Export Preview Surface Mesh	No
- Sizing	
Use Adaptive Sizing	No
<input type="checkbox"/> Growth Rate	1.015
Mesh Defeaturing	No
Capture Curvature	Yes
<input type="checkbox"/> Curvature Min Size	Default (4.5587e-003 m)
<input type="checkbox"/> Curvature Normal Angle	18.0°
Capture Proximity	Yes
<input type="checkbox"/> Proximity Min Size	Default (4.5587e-003 m)
<input type="checkbox"/> Num Cells Across Gap	Default (3)
Proximity Size Function Sou...	Faces and Edges
Bounding Box Diagonal	9.1173 m
Average Surface Area	25.825 m ²
Minimum Edge Length	6.35e-003 m
+ Quality	
+ Inflation	
+ Batch Connections	
+ Advanced	
- Statistics	
<input type="checkbox"/> Nodes	340686
<input type="checkbox"/> Elements	339445

Figure D3: Mesh statistics

APPENDIX E

CALCULATION OF PRESSURE FORCE

To ensure that the surface drag is the result of momentum deficit only, the pressure force is calculated from equation 4.2 for the flow over a smooth flat plate for Re_d 4.5. It is the lowest Re_d of this study as it has the largest BL thickness among the different scenarios and thus will have the highest pressure force.

$$F_p = F_{p,inlet} - F_{p,outlet} + \frac{P_{inlet} + P_{outlet}}{2} \Delta h \quad (E1)$$

Where, $F_{p,inlet}$ and $F_{p,outlet}$ are the pressure force at the inlet and outlet, respectively. P_{inlet} and P_{outlet} are the pressure at the inlet and outlet. $\Delta h = h_{outlet} - h_{inlet}$ is the difference of outlet and inlet height. The pressure values P at the inlet and outlet are the gage pressure values based on the reference pressure at a point before the LE.

Table E1 shows the relevant values for the calculation of net pressure force acting on the control surface for the smooth flat plate at Re_d 4.5.

Table E1: Calculation of Pressure force on the control surface

$F_{p,inlet}$ (mN)	$F_{p,outlet}$ (mN)	$F_{p,streamline}$ (mN)			F_p (mN)	Force due to momentum deficit (mN)	
		P_{inlet} (Pa)	P_{outlet} (Pa)	Δh (mm)			
-0.7622	-1.332	-0.0272	-0.0208	36	-0.864	-0.2942	-93.33

The negative sign indicates that these forces are acting against the flow direction. The pressure force (-0.2942 mN) will have negligible contribution to the surface drag as the force due to momentum deficit (-93.33 mN) on the outlet of control surface is significantly larger.

APPENDIX F

MATLAB CODE

F.1 SUPERPOSITION OF IMAGES

```
clc
clear all
close all
warning off;
%% This code superimposes images to get a pathline of the particles.

%Enter the directory for data images to read
workingDir='D:\Sashank\December 2019\Oil\Vortex\90 cavity 2_1\Re
3.5\Stabilised 1';

%Enter the folder where you want the superimposed image
writingDir = 'D:\Sashank\December 2019\Oil\Vortex\90 cavity 2_1\Re 3.5\New
folder';

Range = 450:3600; %Range of images to superimpose/work with

    superimposed_img = 0;
for ii = 450:3600
    imageName = strcat('img',num2str(ii),'.tif');
    img = fullfile(workingDir,imageName);
    I2 = imread(img);
    I2 = I2/60; %change it depending on brightness of the final result
    superimposed_img = superimposed_img + I2;
end
superimposed_image = superimposed_img;
imageName = strcat('img',num2str(ii),'.tif');
img_to_save = fullfile(writingDir,imageName);
plates_only = superimposed_image;
thresh = 0.98 * max(plates_only(:));
plates_only(plates_only < thresh) = 0;

% If you want to subtract the plates or brightest part of image
superimposed_image = superimposed_image-(plates_only);

% If the final image needs a outline of the plate boundary
ini_img_name = strcat('img',num2str(Range(1)),'.tif');
initial_image = imread(fullfile(workingDir,ini_img_name));

% Need to play around with this to get the best result
```

```

superimposed_image = imadjust(superimposed_image);
superimposed_image = imreducehaze(superimposed_image);
superimposed_image = 2 * superimposed_image;

superimposed_image_and = superimposed_image + initial_image;
imwrite(superimposed_image_and, img_to_save)

imshow(superimposed_image_and)

```

F.2 IMAGE STABILIZATION

```

clc
clear all
close all
warning off;

%% Updated code Jan 1, 2021. Now it can stablize the whole data (All Re) for
a particular model at once.
Re_range = [4.5 5.5 6.5 7.5 8.5];
% Re_range = [3.5 6 8.5];

Range_of_images_list = {900:2800,750:2250,650:1900,550:1650,550:1450};
% Range_of_images_list = {1100:3600,650:2100,450:1450 };

for Re_loop = 1: length(Re_range)
    for Setnum = 1:5

        Re = "Re " + num2str(Re_range(Re_loop));
        path_Re = strcat('D:\Sashank\December 2019\Vortex\45 cavity\', Re);

        run_folder = strcat('Run',sprintf(' %d',Setnum));
        workingDir = fullfile(path_Re,run_folder);

        b = Range_of_images_list(Re_loop);
        Range_of_images = cell2mat(b);

        ref_img_no = Range_of_images(1);

        cd(workingDir);
        n= length(dir('*.tif'));
        l = 20; %how far down should the horizontal line be?
        stabilised_folder = strcat('Stabilised',sprintf(' %d',Setnum));
        writingDir = fullfile(path_Re,stabilised_folder);

        imageName = (strcat('img',num2str(ref_img_no),'.tif'));
        image_path = convertStringsToChars(fullfile(path_Re,'\Run
1\',imageName));
        I = imread(image_path);
        reference_image = I;

        x1x2_vert_line = [1113 1113];

```

```

yly2_vert_line = [746 970];

x1x2_hor_line = [1446 1585];
yly2_hor_line = [788 788];
figure, imshow(reference_image); %('visible','off'),
h1 = imline(gca,x1x2_vert_line,yly2_vert_line);
h2 = imline(gca,x1x2_hor_line,yly2_hor_line);

sub_reference_image1 =
reference_image(yly2_vert_line(1):yly2_vert_line(2), (x1x2_vert_line(1)-
1):(x1x2_vert_line(1)+1));
sub_reference_image1(sub_reference_image1 < 100) = 0;
chk_sum_row = sum(sub_reference_image1,2);
chk_sum_row(chk_sum_row < (max(chk_sum_row)/2)) = 0;
y_reference = mean(find(chk_sum_row > 0));

sub_reference_image2 = reference_image(yly2_hor_line(1)-
1:yly2_hor_line(1)+1,x1x2_hor_line(1):x1x2_hor_line(2));
sub_reference_image2(sub_reference_image2 < 70) = 0;

[a1,b1] = size(sub_reference_image2);
non_zero_values_0 = 0;
for COLUMN = 1:b1-15
    for ROW = 1:a1-18
        sub_matrix =
sub_reference_image2(ROW:ROW+17,COLUMN:COLUMN+14);
        non_zero_values_c_0 = nnz(sub_matrix);
        if non_zero_values_c_0 > non_zero_values_0
            non_zero_values = non_zero_values_c_0;
            C_0 = COLUMN;
        end
    end
end
x_reference = C_0;

for ii = Range_of_images
    imageName = strcat('img',num2str(ii),'.tif');
    img = convertStringsToChars(fullfile(workingDir,imageName));
    target_image = imread(img);

    %    figure,imshow(target_image)
    sub_target_image1 =
target_image(yly2_vert_line(1):yly2_vert_line(2), (x1x2_vert_line(1)-
1):(x1x2_vert_line(1)+1));
    sub_target_image1(sub_target_image1 < 100) = 0;

    chk_sum_row_target = sum(sub_target_image1,2);

chk_sum_row_target(chk_sum_row_target < (max(chk_sum_row_target)/2)) = 0;
y_target = mean(find(chk_sum_row_target > 0));

%% translation part
y_pixel_displacement = y_reference-y_target;

```

```

        tform_y = [0 y_pixel_displacement];
        target_fixed_y = imtranslate(target_image,tform_y,'linear');
        sub_target_image2 = target_fixed_y(yly2_hor_line(1)-
1:yly2_hor_line(1)+1,xlx2_hor_line(1):xlx2_hor_line(2));
        sub_target_image2(sub_target_image2 < 70) = 0;
        counter = 0;non_zero_values = 0;
        for COLUMN = 1:b1-15
            for ROW = 1:a1-18
                sub_matrix_target =
sub_target_image2(ROW:ROW+17,COLUMN:COLUMN+14);
                non_zero_values_c = nnz(sub_matrix_target);
                if non_zero_values_c > non_zero_values
                    non_zero_values = non_zero_values_c;
                    C = COLUMN;
                end
            end
        end
        x_target = C;
        x_pixel_displacement = x_reference-x_target;

        tform_xy = [x_pixel_displacement 0];
        target_fixed_xy = imtranslate(target_fixed_y,tform_xy,'linear');
        %saving the fixed images
        imageName = strcat('img',num2str(ii),'.tif');
        img_to_save =
convertStringsToChars(fullfile(writingDir,imageName));
        imwrite(target_fixed_xy,img_to_save);
        a = 1;
    end
    fprintf('\n[Finished folder no. %d ]\n', Setnum)
end
    fprintf('\n\n... Finished Re %s ...\n\n', Re)
end

```

F.3 RATE OF CHANGE OF MOMENTUM CALCULATION

```

clear all;
clc;
close all;

%% Settings
Re_range = 4.5:8.5;
tic
Run_range = 1:5;
up_index = 333; down_index =38; h0 = 192; top = 40; Col_end = 346;Row_end =
192;

storing_drag = zeros(450,length(Re_range));
storing_drag_runs = cell(1,length(Re_range));

for Re_loop = 1:length(Re_range)
    fprintf('\n[Started Re %d]\n', Re_range(Re_loop))

```

```

fprintf('\t Reading the analysis files... ')
clear X Y U V C
for Run_loop =1:length(Run_range)

    % for oil
    Uo = 20*Re_range(Re_loop)/3.75;
    rho =849.5;

    Re1 = num2str(Re_range(Re_loop));
    Re_str = Re1;
    Run_str = num2str(Run_range(Run_loop));

    Main_folder = 'G:\DATA\Drag Calculation\Oil\Smooth Plate';
    File_folder_cell = strcat(Main_folder,'\Re',{
'},Re_str,'\Analysis',{ ' },Run_str);
    File_folder = cell2mat(File_folder_cell);

    cd(File_folder);
    no_of_files = length(dir('*.vec'));
    ind =0;
    for j = 10:no_of_files
        ind = ind +1; %sometimes j does not start with 1 when we have
initial unsteady BL, so this step
        file_name = sprintf('img%05d.T000.D000.P000.H001.L.vec',j); %the
filename
        file_path = strcat(File_folder,'\ ',file_name); %the path of the
vector file
        fileID = fopen(file_path); %this opens
the file

        str = fgetl(fileID); %reads the
first line of the vector file
        [matchstart,matchend]=regexp(str,'I=.*?(?=(,)', 'start','end');
%finding where I and J is on that first line
        I=str2double(str(matchstart+2:matchend));
        [matchstart,matchend]=regexp(str,'J=.*?(?=(,)', 'start','end');
        J=str2double(str(matchstart+2:matchend));

        %% This section is going to be different from oil and water as
they were processed differently
        %oil
        formatSpec = '%f %f %f %f %f %f';
%specifying the format
        C = textscan(fileID,formatSpec, 'delimiter',' ',' '); %loading the
values into different cells
        fclose(fileID);
        C = [C{1},C{2},C{3},C{4},C{5},C{6}];
%converting into matrix form

        %%
        % we only need these variables
        X(:,ind) = C(:,1); % x-direction in mm
        Y(:,ind) = C(:,2); % y-direction in mm
        U(:,ind) = C(:,3); % x-velocity in m/s

```

```

V(:,ind) = C(:,4); % y-velocity in m/s

% reshaping the vector U into matrix resembling the vector field
U_matrix_original = reshape(U(:,ind), [I,J]);U_matrix_original =
transpose(U_matrix_original);
X_matrix_original =
reshape(X(:,ind), [I,J]);X_matrix_original=transpose(X_matrix_original);
Y_matrix_original =
reshape(Y(:,ind), [I,J]);Y_matrix_original=transpose(Y_matrix_original);
V_matrix_original =
reshape(V(:,ind), [I,J]);V_matrix_original=transpose(V_matrix_original);

%extracting a sub-matrix excluding the columns and rows with
zeros
counter =1;
for Row = 1:J
    if sum(U_matrix_original(Row,:)) ~= 0
        R(counter) = Row; counter = counter +1;
    end
end
counter =1;
for Column = 1:I
    if sum(U_matrix_original(:,Column)) ~= 0
        Col(counter) = Column; counter = counter +1;
    end
end

%The matrices without the zeroes
U_matrix_smo = U_matrix_original(1:Row_end,1:Col_end);
%sub_matrix
V_matrix_smo = V_matrix_original(1:Row_end,1:Col_end);
%sub_matrix
X_matrix_smo = X_matrix_original(1:Row_end,1:Col_end);
%sub_matrix
Y_matrix_smo = Y_matrix_original(1:Row_end,1:Col_end);
%sub_matrix
%some values in the velocity field are incorrect(outliers), so we
need to fix it,
%any values larger than 1.5*Uo is considered zero (outliers). Any
u values inside
%the sub-BL cannot be equal to Uo so thats also zero (outliers).
for ii = 20:190
    for jj = [down_index up_index]
        if U_matrix_smo(ii,jj) >= 0; U_matrix_smo(ii,jj)=0;end
    end
end
U_matrix_smo(abs(U_matrix_smo) >= 1.5*Uo/1000) =0;

U_matrix_cell{Re_loop}{Run_loop,ind} = U_matrix_smo;
V_matrix_cell{Re_loop}{Run_loop,ind} = V_matrix_smo;

end
end

```

```

fprintf(' ...Completed \n')

total = 0;
for index = 1:ind
    for Run_loop = 1:length(Run_range)
        total = total +1;
        dummy_matrix_U{total} = U_matrix_cell{Re_loop}{Run_loop,index};
        dummy_matrix_V{total} = V_matrix_cell{Re_loop}{Run_loop,index};
    end
end
U_mean_matrix= mean(cat(3,dummy_matrix_U{1:end}),3);
V_mean_matrix = mean(cat(3,dummy_matrix_V{1:end}),3);

fprintf('\t Calculating streamlines and pressure ...')

%%%plot the streamline on original mean matrix and then extract values
out from the
%%%control volume domain

%finding BL at upstream and downstream locations

u_up = U_mean_matrix(top:h0,up_index);
u_up_store{Re_loop} = u_up;
y_up = Y_matrix_smo(top:h0,up_index);
u_dn = U_mean_matrix(top:h0,down_index);
u_dn_store{Re_loop} = u_dn;
y_dn = Y_matrix_smo(top:h0,down_index);
half_uup = sort(u_up(((length(u_up))/2):(end-3)));half_udn =
sort(u_dn(((length(u_dn))/2):(end-3)));
Uo_up = mean(half_uup(1:10)); Uo_dn = mean(half_udn(1:10));

i = 0;
for ch = 1:(length(u_up)-1)
    i = i +1;
    du(ch,1) = abs(u_up(i)) - abs(u_up(i+1));
end
l1 = find(du < 0); h_up = l1(end)+1;
if du(l1(end)-1) > 0 && du(l1(end)-2) > 0&& du(l1(end)-3) > 0&&
du(l1(end)-4) > 0&& du(l1(end)-5) > 0
    h_up = l1(end-1)+1;
end

i = 0;
for ch = 1:(length(u_dn)-1)
    i = i +1;
    dn(ch,1) = abs(u_dn(i)) - abs(u_dn(i+1));
end
l2 = find(dn < 0); h_down = l2(end)+1;
if dn(l2(end)-1) > 0 && dn(l2(end)-2) > 0 && dn(l2(end)-3) > 0&&
dn(l2(end)-4) > 0 && dn(l2(end)-5) > 0
    h_down = l2(end-1)+1;
end

```

```

    h_up_stor(1,Re_loop) = h_up;h_down_stor(1,Re_loop) = h_down;
h_dif_sto(1,Re_loop) = -h_up + h_down;
    BL_up = y_up(h_up) - Y_matrix_smo(h0,1); BL_dn = y_dn(h_down) -
Y_matrix_smo(h0,1);
    BL_up_stor(1,Re_loop) = BL_up;BL_dn_stor(1,Re_loop) = BL_dn;
BL_dif_sto(1,Re_loop) = -BL_up + BL_dn;
    % BL_up = BL_up_stor(1,1);BL_dn = BL_dn_stor(1,1);
    BL_dif = BL_dn-BL_up;
    % h_up = h_up_stor(1,1);h_down = h_down_stor(1,1);

    y_upstream = BL_up + Y_matrix_smo(h0,1); %(in mm)this is how high I want
the upstream top (streamline)
    h_u = find(Y_matrix_smo(:,1)<=y_upstream);
    h_upstream = h_u(1);
    actual_y_upstream = Y_matrix_smo(h_upstream,1);

    x_upstream = X_matrix_smo(1,up_index); x_downstream =
X_matrix_smo(1,down_index);

    u_streamline = U_mean_matrix;
    v_streamline = V_mean_matrix;
    x_streamline = X_matrix_smo;
    y_streamline = Y_matrix_smo;
    x_streamline(1,end-1);
    starty =y_streamline(:,end);
    startx =ones(length(starty),1)*323;
    h =
stream2(x_streamline,y_streamline,u_streamline,v_streamline,startx,starty);
    figure(Re_loop)
    yy = streamline(h);
    xlim([0 350]); ylim([0 170])
    quiver(x_streamline,y_streamline,u_streamline,v_streamline);

    fprintf('\t Calculating the surface drag...')

    clear u_up u_dn U_matrix_inst
    clear momentum_deficit_BLo ao bo gaus_momentum_deficit_BL
    %finding the boundary layer

    % Working on instantaneous freestream velocity difference
    for Run_loop = 1:length(Run_range)
        for index = 1:ind
            U_matrix_inst = U_matrix_cell{Re_loop}{Run_loop,index};
            % %finding BL at upstream and downstream locations
            u_up = U_matrix_inst(top:h0,up_index);
            u_dn = U_matrix_inst(top:h0,down_index);

            u_up_BL = u_up(h_up:end); u_dn_BL = u_dn(h_down:end);
            u_dn_BL(end) = 0;u_up_BL(end) = 0;
            u_up_BL2 = (u_up_BL).^2; u_dn_BL2 = (u_dn_BL).^2;
            u_up_BL2sum = sum(u_up_BL2); u_dn_BL2sum = sum(u_dn_BL2);

```

```

        momentum_deficit_BLo(index,Run_loop) = -rho*(BL_up)*u_up_BL2sum +
rho*(BL_dn)*u_dn_BL2sum;
    end
    %filtering the noise? More like smoothing data
    bo=momentum_deficit_BLo(:,Run_loop);
    ao=smoothdata(bo,'gaussian',5);
    gaus_momentum_deficit_BL(:,Run_loop)=ao;

storing_gaus_momentum_deficit_BL{Re_loop}(:,Run_loop)=gaus_momentum_deficit_B
L(:,Run_loop);
    end

    %Get rid of that weird outliers by defining top and low limit
    storing_gaus_momentum_deficit_BL_iso = storing_gaus_momentum_deficit_BL;
    for run_i = 1:length(Run_range)
        for iterat = 1000
            [del_S1,L1,U1,C1] =
isoutlier(storing_gaus_momentum_deficit_BL{Re_loop}(:,run_i),'mean','Threshol
dFactor',3);
            for g = 1:length(del_S1)
                if del_S1(g) == 1
                    storing_gaus_momentum_deficit_BL_iso{Re_loop}(g,run_i) =
mean(storing_gaus_momentum_deficit_BL{Re_loop}(:,run_i));
                end
            end
        end
    end
    end
    fprintf('Completed\n')
    fprintf('[Finished Re %d]\n', Re_range(Re_loop))
    toc
end

```

APPENDIX G

LABVIEW VI

G.1 VI FOR DATA ACQUISITION

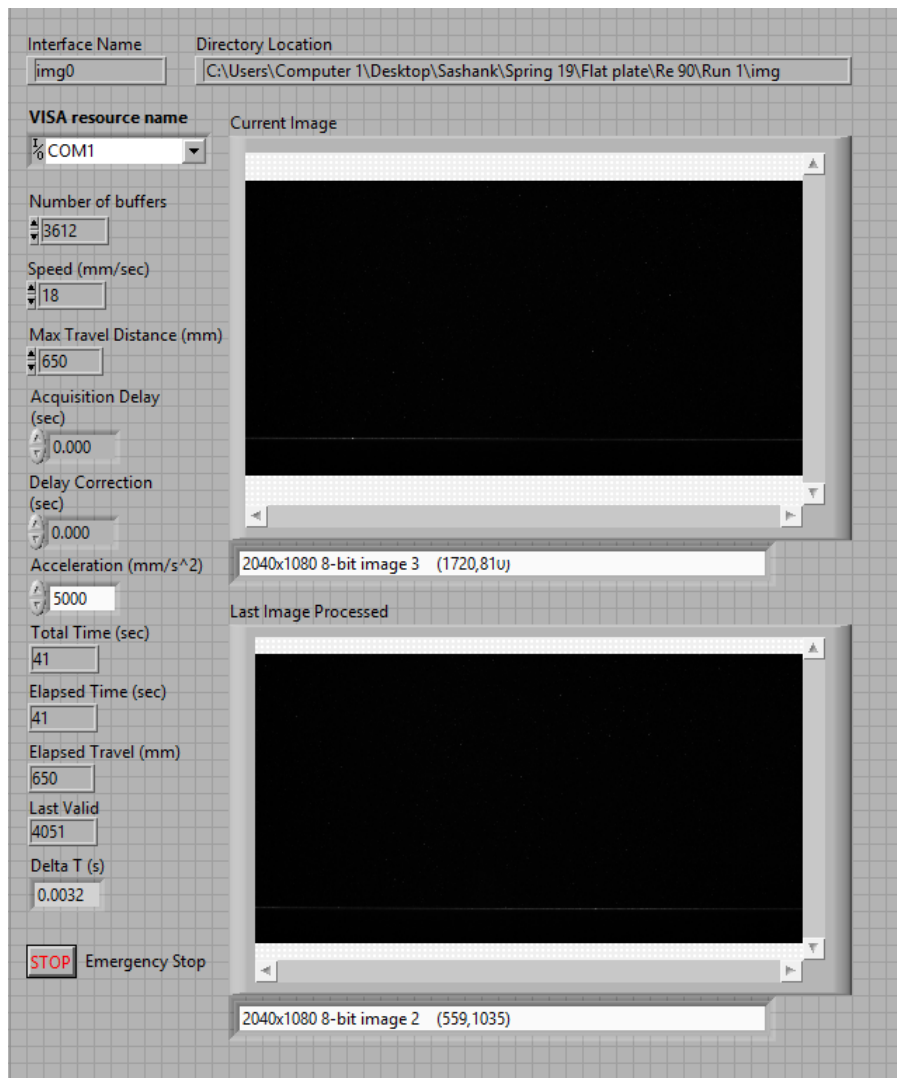


Figure F1: The User interface of the VI file

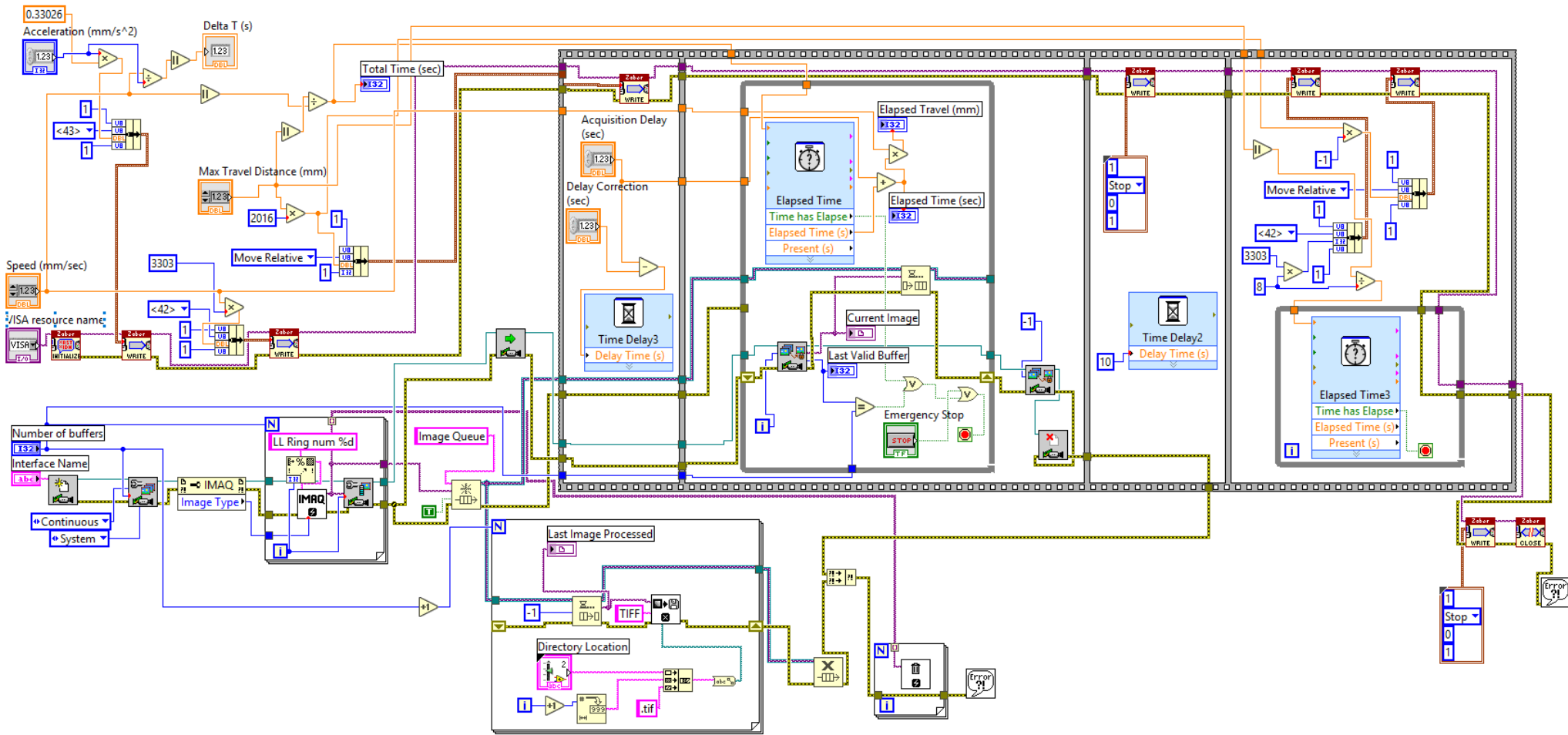


Figure F2: The block diagram of the VI